Micro- and nanostructured polymeric materials for art protection and restoration

Annalisa Cataldi

MICRO- AND NANOSTRUCTURED POLYMERIC MATERIALS FOR ART PROTECTION AND RESTORATION

Annalisa Cataldi

E-mail: annalisa.cataldi @ing.unitn.it

Approved by:

Prof. Alessandro Pegoretti, Advisor
Department of Industrial Engineering
University of Trento, *Italy.*

Prof. Flavio Deflorian, Advisor
Department of Industrial Engineering
University of Trento, *Italy.*

Ph.D. Commission:

Prof. José Manuel Torralba Castelló,
IMDEA Material Institute
Universidad Carlos III de Madrid, Spain.

Prof. Alberto Molinari,
Department of Industrial Engineering
University of Trento*, Italy.*

Prof. Yves Leterrier,
Laboratoire de Technologie des
Composites et Polymères
*Ecole Polytechnique Fédérale de
Lausanne, Switzerland.*

Dr. Antonietta Guagliardi,
Institute of Crystallography
*National Research Council IC-CNR and
To.Sca.Lab, Italy.*

University of Trento,

Department of Industrial Engineering

April 2015

Alla mia famiglia

"In scientia veritas, in arte honestas."
In science truth, in art honour.

Anonymous
In Jon R. Stone, The Routledge Dictionary of Latin Quotations (2005), 170

Cover image from De claris mulieribus, a medieval illuminated manuscript of 1403. National Library Paris, France - "The painter Thamar with an assistant grinding pigment

Abstract

In the restoration field the synthetic resins are commonly used and they are selected in order to replace natural products and possibly overcome their drawbacks. Nevertheless, these resins are not completely able to cover the specific mechanical properties required in each restoration work. The main aim of this research is the development of innovative micro/nanocomposite materials with enhanced features for artwork conservation operations. The introduction of appropriate amounts of micro- and nanofillers within commercially available art preserving polymers may allow the improvement of their mechanical deficiencies, without impairing their physical and chemical properties.

Cellulose microcrystals (CMC) and nanocrystals (CNC) were selected as natural reinforcing fillers for a commercial acrylic copolymer (Paraloid B72) widely applied as a consolidant of wooden objects and two molecular weights of a thermoplastic water soluble adhesive used in the restoration of oil paintings (Aquazol 200 and 500). In particular, melt-compounded Paraloid and Aquazol based microcomposites with various amounts (5÷30 wt%) of CMC and thin films of Aquazol 500 micro- and nanocomposites produced by the solution mixing method with a CMC and CNC content of 5-10-30 wt% were investigated. Several characterization techniques were used in order to assess the effect of micro- and nanocellulose on the physical and thermo-mechanical behavior of these three thermoplastic polymers.

In the first part of the work, the characterization of melt-compounded and compression molded microcomposites under dry and conditioned state (T= 23°C, RH= 55%) was performed. All dried and wet formulations showed a similar stabilizing effect of CMC flakes with an increase of elastic modulus and a decrease of thermal expansion coefficient and creep compliance,

regardless of the moisture content. Interestingly, conditioned composites exhibited the enhancement of the tensile properties at break, in contrast to dried microcomposites that reported a drop in these properties. On the other hand, the highest amount of CMC led to a chromatic change of the three matrices towards yellow-brown tones.

In the second part of the work, the characterization of solution mixed micro- and nanocomposites based on Aquazol 500 highlighted the systematic increment of the dimensional stability of the neat resin due to the presence of both CMC and CNC particles. Remarkably, CNC proved to be more effective than CMC in increasing of the stiffness and the elongation at break of Aquazol as the filler loading increased, without impairing the good optical properties of this material.

In the third part of the work, the application of melt-compounded Paraloid/CMC composites as consolidants for damaged wood was investigated. CMC introduction did not change the good viscosity of the neat matrix and especially its good water repellency. Wood samples treated with microfilled Paraloid exhibited an increment of the stiffness and the flexure strength under quasi-static and impact conditions and, additionally, a systematic enhancement of the radial and tangential surface hardness almost up to the intact wood values was observed.

In the last part of this thesis, the practical application of CMC and CNC Aquazol based adhesive films made by melt-compounding and solution mixing was investigated for the lining of oil paintings. Single-lap shear tests confirmed the stabilization action of both CMC and CNC particles on all experimental formulations with a progressive reduction of the compliance proportionally to the filler loading. Even in this case the increment of the Aquazol dimensional stability was mainly imparted by the presence of CNC. Only for solution mixed CMC composites a dramatic drop in the adhesive strength as the filler content increased was detected.

Table of contents

Chapter III

List of Figures

List of Tables

List of abbreviation and acronyms

[η] - Intrinsic viscosity

$CLTE_g$ - Coefficient of linear thermal expansion in the glassy state (i.e. below the glass transition temperature)

$CLTE_r$ - Coefficient of Linear Thermal Expansion in the rubbery state (i.e. above the glass transition temperature)

CMC - Cellulose Microcrystals

CNC - Cellulose Nanocrystals

D - Creep compliance

DI - Ductile Index

DMTA - Dynamic Mechanical Thermal Analysis

DP_W - Weight-average Degree of Polymerization

DSC - Differential Scanning Calorimetry

E - Elastic Modulus

E' - Storage Modulus

E" - Loss Modulus

E_f - Flexural modulus

ESEM - Environmental Scanning Electron Microscopy

FESEM - Field Environmental Scanning Electron Microscopy

FTIR - Fourier Transform Infrared

G_{IC} - Critical strain energy release rate

H_r - Radial Surface Hardness

H_t - Tangential Surface Hardness

K_{IC} - Critical stress intensity factor

M% - Moisture Content

M_{MAX} - Final Moisture Content

P_{TOT} - Percentage of Total Porosity

T% - Relative transmittance

tanδ - Loss Factor

TEB - Tensile Energy to Break

TEM - Transmission Electron Microscopy

T_g - Glass Transition Temperature

TGA - Thermogravimetric Analysis

T_{MAX} - Temperature associated to the maximum mass loss rate

T_{onset} - Temperature associated to the beginning of the thermal degradation

ts - Time required to reach the equilibrium water content

u - Adhesive Joint Displacement

U_i - Specific energy adsorbed at the crack initiation

U_P - Specific energy adsorbed during the crack propagation

U_{TOT} - Total specific absorbed energy

ε_B - Strain at break

$\varepsilon_{MAX,f}$ - Maximum flexural strain

η - Viscosity

σ_B - Stress at break

$\sigma_{MAX,f}$ - Maximum flexural stress

τ_B - shear stress at break

ω - Angular velocity

Chapter I

Introduction

Synthetic resins have been introduced in the artwork restoration field since the early nineteenth century in order to replace natural products which presented several problems of ageing resistance, especially against biological degradative attacks [1]. At the beginning conservators were reluctant to change over new products coming from the chemical industry, but now these materials are applied in every area of art conservation [2]. In restoration these polymers can be utilized as protective materials, in order to create a surface coating with barrier properties, especially able to limit the water uptake, as consolidants to recover the mechanical properties of damaged objects and as adhesives [3]. There are some kinds of polymers, such as some thermoplastic resins that, thanks to their good handling properties, in particular, their flexibility and transparency [2, 4], are indiscriminately applied in all restoration operations without considering that each of these operations require specific mechanical performance to the polymer to be applied. Despite this, the approach of conservators has always

been to choose resins based solely on their optical features and chemical resistance and rarely on their mechanical properties. For the most of these materials, in the literature, there is a lack of scientific studies on their mechanical properties, while, their physical and chemical behavior after natural and artificial ageing is well known. Additionally, all polymers used for art restoration come from the industrial field, therefore they are not specifically designed for conservation purposes and not completely able to cover the required mechanical performance of a specific restoration work.

Starting from these considerations, the present research investigates the possibilities offered by cellulose-based micro- and nanocomposites to improve the properties of polymers for artwork restoration. The introduction of appropriate amounts of micro- and nanofillers within commercial polymers for art protection may allow an improvement of their mechanical weak points, minimizing the increase in cost, without impairing their good physical and chemical properties.

Natural fillers present several advantages in comparison to the corresponding synthetic agents. They are non-toxic, biodegradable and recyclable. Natural plant derived particles have generally lower density and high specific strength and elevated stiffness [5, 6].

The aim of this research is the investigation of the possible effect of the addition of different amounts of cellulose micro- and nanocrystals (CMC, CNC) on the physical and thermo-mechanical properties of two commercial resins, widely used for the conservation of cultural heritages. In particular, the attention was focused on Paraloid B72® and two different molecular weights of Aquazol®, in the dry state and under recommended hydrothermal conditions for artworks conservation (T= 23°C, RH= 55%).

Different types of composites were considered:

- Microcomposites at different filler contents (from 5 wt% to 30 wt%) of cellulose microcrystals, CMC, made by melt-compounding and compression molding (see section 3.2). This microfiller presents a specific gravity of 1.56 g·cm^{-3} and an average aspect ratio of 2.4.

- Nanocomposites filled with 5÷30 wt% of cellulose nanocrystals, CNC, produced through solution mixing and casting process (see section 3.2). CNCs are rod-like particles with an average aspect ratio of 50.

- Microcomposites with the same amounts of CMC prepared through solution mixing and casting in order to perform a comparison between micro- and nanocomposites.

Optical and electron microscopy techniques were employed to evaluate the fillers dispersion into the matrices, while calorimetric analysis were conducted to evaluate the effect of the various fillers on the thermal stability and the glass transition temperature of the neat matrices. The possible change in the optical features of polymers due to the presence of micro- and nanocrystals was investigated by CIELAB color measurements, optical and UV-vis spectroscopy analysis. Viscoelastic properties were determined through quasi-static tensile tests, for the evaluation of the elastic modulus, and dynamic mechanical tensile tests under tensile and creep conditions. The fracture behavior was estimated through quasi-static tensile tests, in order to assess the effect of fillers on the tensile properties at break. A more detailed analysis on the fracture behavior of microcomposites was conducted by

determination of the fracture toughness under plane-strain conditions. Additionally, the investigation of the synergistic action of the water sorption and the fillers presence on the mechanical behavior of polymeric matrices was carried out.

In the present work a particular attention was dedicated to the application of the investigated materials as consolidants for degraded wood and as adhesives for the lining of oil paintings on canvas. For these conservation operations the increase of strength and elastic modulus and dimensional stability and elongation resistance of the polymer are respectively desirable.

For the evaluation of the possible increase of the consolidating properties of Paraloid B72 filled with microcellulose a physical and mechanical characterization was performed. Wood samples were treated with the investigated materials in acetone solution. Through gravimetric analysis and mercury intrusion porosimetry tests it was possible to assess the change in the water uptake tendency and the pore size of consolidated materials. Concurrently, Fourier transform infrared spectroscopy analysis and optical microscope observations allowed the determination of the penetration degree of consolidant solutions within wood samples. Three points bending tests, Charpy impact tests and ShoreD hardness tests were performed in order to investigate the action of the filler on the strength, the elastic modulus and the surface hardness of wood. Microstructural analysis of impact fractured cross-sections of wood samples with and without consolidants were carried out.

The assessment of the possible improvement of the creep resistance and the adhesive strength of micro- and nanocomposites based on Aquazol applied as adhesives of canvas were performed by single-lap shear tests under quasi-static and creep conditions. Microstructural analysis of the fracture surface of all adhesive joints were carried out.

Chapter II

Background

2.1   Use of synthetic polymers in the art restoration

The attention for the conservation of buildings, sculptures, painted works and all artworks evidence of human history and culture, is known from the Middle Age. There are very famous restoration operations performed in the sixteenth and in the seventeenth centuries, such as the restoration of the Sistine Chapel frescoes (1565), made 53 years after the ceilings painting by Michelangelo Buonarroti, and the conservation projects of Raphael's frescoes in Rome (1659 and 1702) [7, 8]. The first conservators were artists working especially to preserve the private collections from fire, insects, mold, water infiltration, excessive humidity and dust. They used the same materials already utilized in the production of artworks. The profession of restorer became official and legitimate in the eighteenth century with the diffusion in Europe of museums, galleries and libraries [9]. The first products utilized in conservation were natural, in particular, starch pastes, plant gums and resins, protein binders of glue and albumin, beeswax, polysaccharides and fats [3]. With the development of trade and technology a wide range of drying oils and resins became available. These materials and

the most recent colophony, mastic, sandarac, dammar and paraffin wax were the only materials suitable for repairing of cultural heritage until the late of the nineteenth century [10, 11]. In the early of 1920s the first synthetic resins, cellulose nitrate and other cellulose derivatives, were introduced in the conservation field. Then, in the 1930s, the first acrylic polymer, PVA was used as paintings varnish.

Nowadays, in the restoration field, the synthetic resins are widely used and they are selected ever more often in place of natural products. Among the various synthetic film-forming polymers, vinyl acetate derived polymers with the most diffused polyvinyl alcohol, acrylic resins and, in particular, acrylate and methacrylate polymers, polyurethanes, polyamides, silicones and epoxy resins are the most selected by conservators [3]. Conservators can apply these products as protective films, as consolidant materials and as adhesives.

2.1.1   Protective materials

A protective polymer can be defined as a surface film on the top of artworks acting as a barrier against water infiltrations and air pollutions. This film is applied on the surface of intact objects to prevent decay or on consolidated materials with a final thickness from few μm to some hundreds μm. It is a sacrifice coating and for this reason, over time it will be damaged and it should be replaced periodically [3]. Polymeric coatings can be applied as solutions and suspensions or as curable monomers and oligomers. In the first case, the formation of the hydrophobic film occurs after the evaporation of the solvent for the coalescence phenomenon [12] (Figure II-1). While for thermosetting polymers the film will be created after the in situ crosslink reaction.
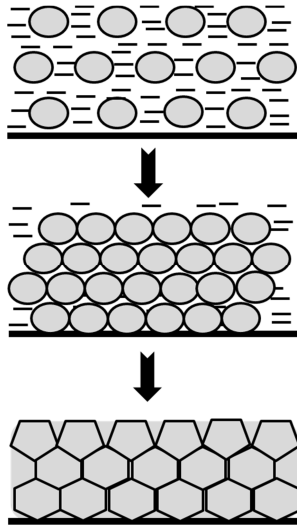
Figure II- 1. Formation of a protective coating with evaporation of solvent.

The coverage of substrates has to be complete and uniform, because any discontinuity or defect in the protective film is a preferential way for water and contaminants to penetrate inside and develop degradation processes. A high wettability and a low viscosity are desirable. The main aim of a protective layer is the water repellency action, but, at the same time, the surface coating has to allow the vapor permeability and the breathing of treated objects [13, 14]. A high transparency of the coating and a good match of its refractive index with the substrate are necessary for this kind of application in order not to impair the correct reading of artworks. A protective material needs a good chemical stability to acids, alkalines, pollution agents and all elements and compounds which could promote decay reactions. Coatings can be utilized as vehicles of corrosion inhibitors

and ultraviolet absorbers. Another important feature required to protective treatments is the reversibility, the possibility to remove the old coating and replace it with a new one. There are some cases where the removal of a polymer is practicable, e.g. coatings on compact substrates (metals), but in the cases of porous surfaces or where the cross-linking or the oxidation of polymeric chains make insoluble the coating, the reversibility is impossible [3]. For this reason, conservators prefer to apply thermoplastic resins instead of thermosetting polymers as protective films, and the lowest feasible molecular weight should be used.

2.1.2 Consolidant materials

A consolidant is a material that applied by impregnation in the inner of damaged objects has to recover their mechanical and cohesion properties. The consolidation being an irreversible treatment is carried out only when the conservation state of artworks is critical, with significant microstructural damages. Moreover, since the removal of consolidants is impracticable, a high stability and durability of these materials is really important. It would be desirable that old consolidation treatments let to treat again objects even with different products. Consolidant products are applied in solutions or suspensions, in the molten state due to the use of elevated temperatures or as monomers/oligomers for a resulting in situ polymerization. A low viscosity is needed for the polymer to reach the deep of the object and fill cavities, defects and cracks. A uniform distribution of the consolidant solution is desirable to reduce interface stresses and guarantee a good consolidating action of the product.

2.1.3   Adhesives

This kind of materials promotes the adhesion between broken apart surfaces
filling the microcavities of substrates. Protective and consolidant materials
can be consider more in general adhesives. Some adhesives can act   as
consolidants but it is recommended to use separate processes for
consolidation and adhesion [3]. Actually, an adhesion operation is performed
on the surface of the object, while a consolidation treatment acts in the inner
of the artwork (Figure II-2).
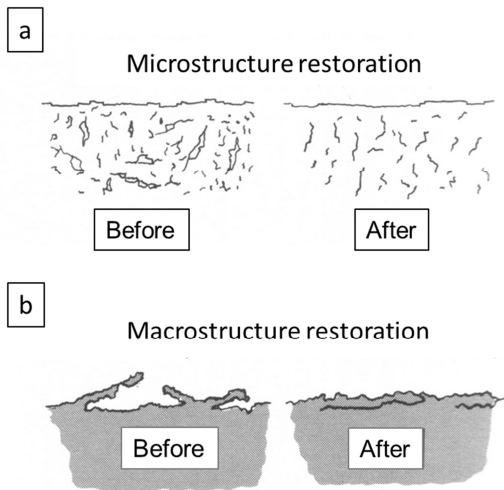
**Figure II- 2. (a) Consolidation of microstructure of artwork, (b) adhesion of broken apart
surfaces of artwork substrate [15].**

In restoration operations, conservators can choose among natural glues and
synthetic polymers. The natural adhesives can have a vegetable or animal

origin such as starch pastes and the rabbitskin glue. It is possible also to distinguish adhesives through their mechanism of adhesion. Thermoplastic resins and some natural polymers, such as beeswax and colophony, are applied at elevated temperatures in the molten state and they solify upon coolling. Other natural and synthetic polymers, become solid joints after the evaporation of a solvent. The properties of adhesives in the molten state are different from the properties of the solid adhesive joint. Good wettability, in order to uniformly cover the substrate, optimal viscosity for the specific surface to treat, not to penetrate in the deep of the object, a not so long time for the creation of the joint and high durability are the properties required to a liquid adhesive during application. When the joint is made, the solid adhesive system needs a good adhesive strength, in order to keep together two different surfaces, enough flexibility and elasticity to preserve the peculiar matter features of the artwork and it has to guarantee its reversibility and the possibility to be removed [16, 17]. The adhesive thickness is another important thing to consider. A thin adhesive film would be utilized in order to avoid any dimensional change (expansion and contraction) due to the environmental conditions.

2.2   *Consolidation of degraded wood*

2.2.1   **State of art**

One of the most used constituent material for art objects is wood. The historical wooden heritage is huge and varied. This material is very sensitive to decay and several kind of degradative processes can attack it [18]. The physical degradation involves especially outdoor exposed wood and can occur when wood is undergone to continuous sun-rain cycles and it swells

and shrinks for the cyclical sorption and evaporation of water, with the formation of irreversible deformations. Another cause of damage for wood is the temperatures fluctuation between day and night when big thermal excursions are involved. The water present into wood pore passes from solid to liquid state, increasing and decreasing its volume and the pressure on the pore walls. This can promote microstructural fractures and the increase of the open porosity of the object. Even the sun can play a role in the physical degradation of wood with the solubilization of lignin that depositing on the surface gives a typical grey color to wood. However, fluctuations of indoor microclimate conditions can produce similar effects on the structure of wooden artworks with microcracks and deformations. There is also a mechanical decay of wood due to vibrations, hits, erosion and abrasion phenomena. Biological degradation is very common for the most types of wood and their restoration is generally a critical issue. Certain wood species because of their microstructure and porosity type are less resistance than others to biological attacks. Moreover, the degradation operated by living organisms is not always the same. Xylophagous agents can generate chemical, physical and/or mechanical decay in wood and one of the main effect of these degradative actions is the reduction of its mechanical strength [19-22]. When the conservation state of wooden artworks is critical, conservators prefer to consolidate objects through the application of synthetic resins by brush, spray, injection or direct immersion in order to allow the capillarity impregnation of the consolidating solution. Low pressure and vacuum impregnation chambers can be suitable to consolidate small historical objects as well. Thanks to their physical and mechanical properties and especially their good reversibility, thermoplastic polymers are preferred over thermosetting resins [23-25].

2.2.2   Paraloid B72

Paraloid B72[®], a methyl-acrylate/ethylene methyl-acrylate (MA/EMA) copolymer, is one of the most used thermoplastic resin in restoration [26]. This MA/EMA copolymer, thanks to its capacity of forming soft high-transparency coherent films has always been used for metal aerosols, wood coatings, clear coatings for general product finishing and flexographic printing inks and then oriented to artwork restoration. Paraloid B72 is well known as "*the general-purposes resin*" in the restoration field because, especially in the past, it was utilized as a protective layer for metals and other compact surfaces; as a consolidant by impregnation of porous materials, such as wooden objects, plasterwork and tuff and as an adhesive for glasses and ceramics [27, 28]. Moreover, this product could be applied in solution for the restoration of oil paintings, making a transparent varnish layer and as adhesive in the lining of canvas. Paraloid B72 presents a lower tendency to water sorption and several years of usage of Paraloid B72 and repeated testing of artificial and natural ageing demonstrated its higher chemical stability, yellowing resistance and photo-thermal oxidation stability with respect other commonly used acrylics resins for art conservation [29-31]. On the other hand, the most severe limitations in the use of acrylics resins are related to their application mode, the resin concentration and the service conditions. However, these limitations have not impeded the use of Paraloid B-72 also in treated surfaces exposed to high humidity and temperature conditions, making mistakes and irreversible damages to artworks [32-35]. In the last years, conservators are focusing the usage of Paraloid just on certain restoration operations and under controlled environmental conditions. Paraloid B72 is certainly one of the most utilized consolidant material for degraded wood, in particular, for wood exposed to

biological attack that exhibits a critical structural decohesion state [3, 18, 23, 36]. Therefore, an increase of the strength and the elastic modulus of degraded wood after consolidation treatment is recommended.

2.3 Lining of oil paintings on canvas

2.3.1 State of art

The restoration of oil paintings on canvas involves all different material layers that constitute this kind of objects, such as the textile substrate, the preparation layer, the paint film and the varnish layer. For this reason, this restoration operation is one of the most concerning for conservators [37]. Often the critical source of oil paintings decay is the substrate. In fact, the flax canvas, that is the most used textile as substrate to paint, is sensitive to the environmental conditions and especially to the humidity level of the exposure environment [38]. Additionally, oil paintings are fixed to a stretcher and therefore subjected to long lasting constant shear stresses. Excessive dimensional variations of canvas and elevated stretching, can promote the deformation of the substrate and, consequently, the formation of cracks in the textile and in the paint film as well, until the separation of the paint from the preparation and the support [39]. The loss of tension and the relaxation of the canvas can occur [40]. A degraded canvas has to recover its initial mechanical properties and to do this conservators have two options, the consolidation of the original support and/or the lining of the canvas [41]. In both restoration operations an adhesive is applied to the damaged textile.

The lining of paintings was introduced in the 18th century [42]. The first adhesives utilized for this application were animal glue and flour, applied by hot steel iron. Wax-resins, generally called hot-seal adhesives, were

introduced in the 19th century in order to replace natural glue/paste adhesives which can suffer from degradative processes becoming hard and brittle [39, 42]. Lining processes were improved with the introduction of hot-tables and low-pressure consolidation processes that guaranteed a better control of temperature and pressure parameters during treatment [43]. This change in technology led to the use of heat-seal adhesives. In particular, thermoplastic adhesives are the most used for their good physical properties and high chemical and yellowing stability [38, 42].

The lining of oil paintings requires a combination of optical and chemical stability and specific mechanical properties. The adhesive joint needs an appropriate adhesive strength to keep connected surfaces with different properties (the old canvas and the new lining textile), good viscoelastic and creep strength and relaxation resistance [44]. Therefore, for this specific application an improvement of the adhesive joint dimensional stability under creep conditions is highly desirable.

2.3.2 Aquazol

Aquazol is a poly 2-ethyl-2-oxazoline, available in several molecular weights (i.e. 5, 50, 200, 500 daltons). It is a versatile water soluble adhesive that is soluble in a wide range of organic solvents, as well. Generally called PEOX, introduced in the field of conservation in the 1990s, even though scientific studies on this synthetic resin have been carried out since the 1980's [45, 46]. Aliphatic tertiary amides present a chemically stable form of nitrogen, therefore PEOXs tend to guarantee a good aging behavior [47, 48]. In fact, the results of accelerated aging studies demonstrated how Aquazol polymers are able to maintain both their neutral pH and their stability with aging [46, 49]. It has good thermal stability and ability to bond

a broad range of materials [47]. The most common use of this thermoplastic resin is in coating formulations [50], as pigment dispersants in inks [51] and as adhesive for various types of artworks [52]. Since its refractive index is close to that of sodalime glasses, Aquazol was originally applied as consolidant for glassy objects [46]. Thanks to its elevated transparency, high flexibility even at low humidity level [53, 54], ability to make protective film, good capability to penetrate into sharp cracks and easy removability, being a water soluble polymer, in the 1990s Aquazol was oriented in the restoration of oil paintings [55]. Nowadays, conservators utilize this polymer also as adhesive on friable paints and cracked gilding in order to fix the paint film onto the original canvas [49, 52]. On the other hand, Aquazol is a very sensitive hygroscopic material and conditioning levels over 50% of relative humidity significantly affect its mechanical behavior. The plasticizing action due to the moisture content emphasizes its rubber-like behavior leading to a decrease of its dimensional stability. This loss of tension can produce a distortion of the canvas thus impairing a coherent reading of the artwork [41].

2.4   *Micro- and nanocomposites*

Composites are combinations of at least two distinct phases, a matrix and a dispersed material, differing in composition, where each phase maintains its own identity. The matrix phase is the primary and continuous phase and usually it is the most ductile phase of a composite. The dispersed phase is arranged within the matrix in a discontinuous form. Since this secondary phase is usually stronger than the matrix, it is sometimes called reinforcing phase [56].

Engineering composite materials represent a special type of composites with three peculiar features:

- they contain two or more distinct constituents,
- they are synthesized controlling the form, distribution and amount of constituents,
- they have more specific and superior final performances that can be predicted from the properties, amounts and arrangements of constituents by mechanical criteria [57]. Compared to conventional engineering materials, composites can exhibit exceptional elevated strength and stiffness with respect to their density (Figure II-3).
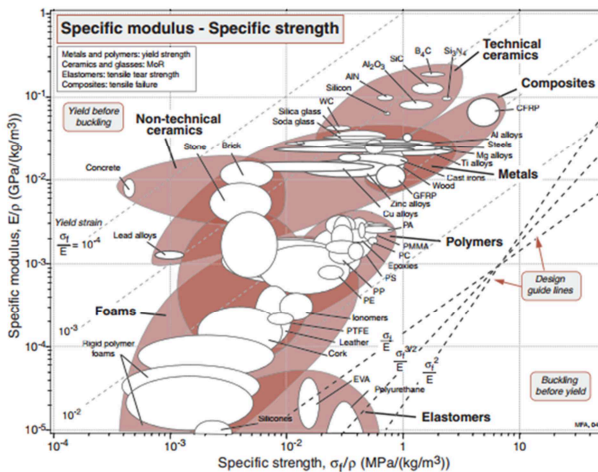
Figure II- 3. Specific elastic modulus E/ρ plotted against specific strength σ_f/ρ (on log scales) [57].

Composites can be distinguished by the type of the matrix composition into: metal matrix composites (MMCs), ceramic matrix composites (CMCs), and polymer matrix composites (PMCs). This last class of composites is certain the most industrially produced and the most scientifically investigated. Thanks to their low cost and simple fabication methods, polymer composites are so widely used in the engineering field [58].

Polymer composites can be distinguished by the characteristic size of the filler particles:

- microcomposites that contain micrometer-scale fillers;

- nanocomposites that contain nanometer-scale fillers, i.e. fillers that have at least a characteristic size less than 100 nm.

As compared to neat polymer, microcomposites and mainly nanocomposites exhibit markedly improved properties in terms of elastic modulus, strength, impact performance, and heat resistance.

2.4.1   Micro- and nanofillers

Particles can be spherical, cubic, platelet with regular or irregular geometry and, usually, they do not have a preferential orientation [59]. Reinforcing agents are often differentiated by their degree of anisotropy (aspect ratio). Fillers with plate-like geometry such as layered silicates, talc and mica are more stronger than spherical fillers and the effect of glass fibers is expected to be even stronger [58]. The particle size and distribution significantly affects the mechanical behavior of the composite material [60, 61]. For instance, large particles can easily debond from the matrix, leading to a premature failure. A high matrix/filler and particle/particle interact is

desirable for good functional properties of the composite. The surface free energy of fillers determines both interactions and it has a pronounced effect on the mechanical properties of the composite [58].   Thanks to surface treatments one can modify this property of fillers. In order to obtain a high dispersion degree of particles, fillers must be homogeneously distributed and dispersed in the polymeric matrix. Good distribution and good dispersion of fillers promotes all the advantages of the composite technology. Figure II-4 shows examples of dispersion and distribution conditions achievable in a composite material [62].
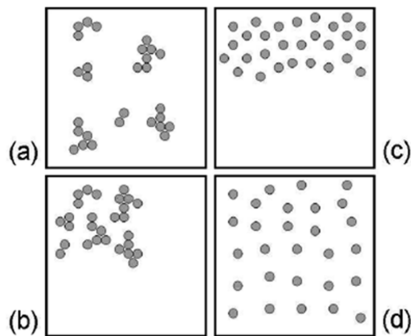
Figure II- 4. A schematic illustration of (a) good distribution but poor dispersion, (b) poor distribution and poor dispersion, (c) poor distribution but good dispersion and (d) good distribution and good dispersion [62].

Aggregation phenomena are strictly related to the particle size. Extensive filler agglomerations can lead to insufficient homogeneity, rigidity and low strength, acting as crack initiation sites [63, 64].   A broad variety of materials has been used as fillers in composites. Precipitated calcium carbonate, carbon black, carbon nanofibers and nanotubes, graphene and

graphite nanoplates, mica, short and long glass fibers, aramid and kevlar fibers, clay and layered silicates, fumed metal oxides (SiO_2, TiO_2, etc.), silicium carbide, phenolic microspheres and several flame retardants are just some of the most commonly utilized fillers or reinforcements [58].

Nowadays, there is a more and more large use of natural fillers from plants such as wood flour and fibers, and micro- and nanocellulose . This class of fillers has very high strength and, being abundantly available and biodegradable, present special advantages in comparison to synthetic fillers. [65, 66].

2.4.1.1 *Cellulose microcrystals*

Cellulose microcrystals, CMC, consist of cellulose fibers with a diameter of few micrometers. These fibers are made up elementary cellulose microfibrils having a width of about 5 nm and a length of about 20/30 nm [67] In Figure II-5 a schematic of microfibrils in cellulose fibers is shown [68].
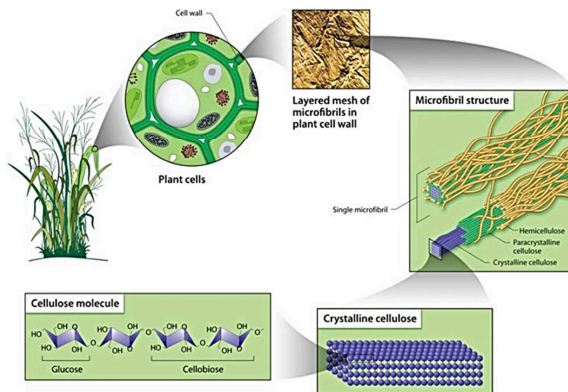
Figure II- 5. Schematic of the cellulose cell wall and microfibril organization [68].

Microcrystalline cellulose is obtained in industrial scale from native cellulose material or pulp through the acid hydrolysis process that it has been already known for over 50 years [69]. Production of CMC from materials such as water hyacinth, coconut shells [70], sugar cane bagasse [71]and jute has been investigated as well. The reaction of cellulose with water solution of strong mineral acid at boiling temperature removes the amorphous fraction and reduces the degree of polymerization (level-off degree of polymerization, LODP) of the cellulose chains [72] (Figure II-6).
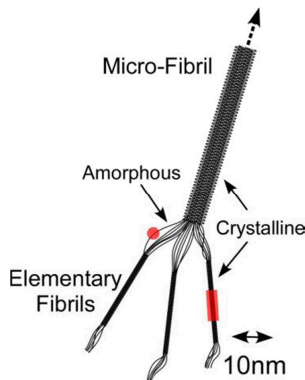
Figure II- 6. Schematic of crystalline and amorphous fractions in a cellulose microfibril [73].

Due to this hydrolysis reaction CMC presents a high degree of crystallinity. With the increasing of crystallinity, tensile strength, dimensional stability and density of microcrystalline cellulose increase. Moreover, this reinforcing agent has a good water swelling resistance and it is stable at elevated temperature and under different pH conditions [74, 75]. As all natural plant derived fibers, CMCs are non-toxic, biodegradable and recyclable and they

have generally lower density and high specific strength and elevated stiffness. For this reason, they are applied in the production of low-density composites at high filler concentration [76].

2.4.1.2   Cellulose nanocrystals

Nanocellulose exhibits excellent characteristics. In particular, a huge specific area, impressive mechanical properties, good optical properties, biocompatibility and biodegradability, rendering this material a potential candidate to be use as reinforcement in the polymer composite science [77]. The study of cellulosic nanofibers as a reinforcing phase in nanocomposites started 15 years ago [78]. Depending on the different production method, it is possible to obtain three main families of nanocellulose: microfibrillated cellulose (MFC), cellulose nanocrystals (CNC) and bacterial nanocellulose (BNC). In Table II-2 the different terminologies used to describe cellulose nanoparticles associated to their material source and production process are listed [79].

Table II- 1. The different terminologies used to describe cellulose nanoparticles [79].

Type of nanocellulose	Related terms	Typical sources	Formation and averaged dimensions
Microfibrillated cellulose (MFC)	Microfibrillated cellulose, cellulose nanofibrils, nanofibrillated cellulose, nanofibrillar cellulose, and microfibrils	Wood, sugar beets, potatoes, hemp, and flax	Delamination of wood pulp by mechanical pressure preceding and/or following chemical or enzymatic treatments Diameter: 5–60 nm Length: several µm
Nanocrystalline cellulose (CNC)	Cellulose nanocrystals, crystallites, whiskers, and rod-like cellulose microcrystals	Wood, cotton, hemp, flax, wheat straw, mulberry bark, ramie, tunicin, and cellulose from algae and bacteria	Acid hydrolysis of cellulose from many sources Diameter: 5–70 nm Length: 100–250 nm (from plant celluloses); 100 nm–several µm (from celluloses of tunicates, algae, and bacteria)
Bacterial nanocellulose (BNC)	Bacterial cellulose, microbial cellulose, and bio-cellulose	Low-molecular sugars and alcohols	Bacterial synthesis Diameter: 20–100 nm (various nanofibre networks)

In Figure II-7 one can observe the morphology of the three different classes of nanocellulose [79].
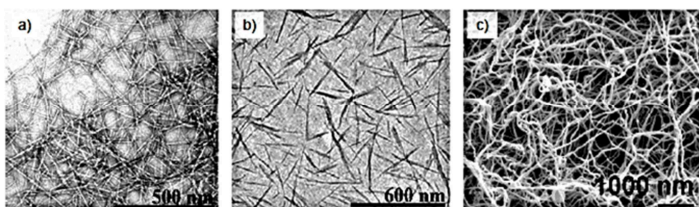
Figure II- 7. a) Transmission electron micrographs of a) MFC, b) CNC, and c) BNC [79].

Bacterial nanocellulose (known also as bacterial cellulose, microbial cellulose, or bio-cellulose) is made by aerobic acetic acid bacteria of Gluconacetobacter (e.g., Acetobacter xylinum). This genus of bacteria produce a fine fibrous network of fibers with an average diameter between 20-100 nm [80]. Bacterial cellulose differs from the other two types of nanocellulose for its biotechnological build-up process. MFC and CNC are instead formed by the delamination of natural fibers to separate and isolate the microfibrillar materials [81] (Figure II-8).
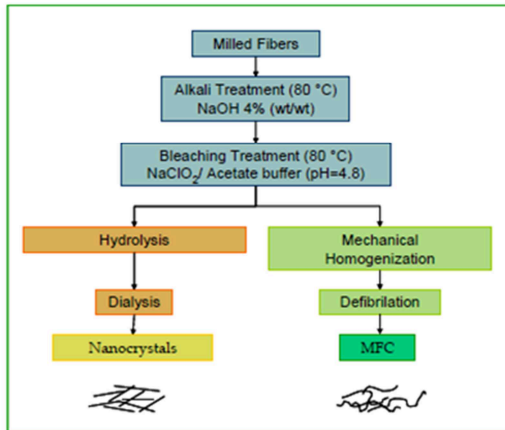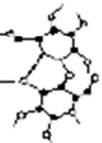
Figure II- 8. The main steps involved in the preparation of cellulose nanoparticles [82].

Microfibrilleted cellulose, or its synonymous nanofibrils, is used to designate long flexible nanoparticles consisting of alternating crystalline and amorphous strings. MFC can be considered as a cellulosic material, composed of expanded high-volume cellulose, moderately degraded and greatly expanded in surface area [82, 83]. MFC presents a web-like structure [84, 85], obtained by a homogenization process. In fact, MFCs are extracted

from the wood cell by a mechanical disintegration process that was first obtained by Herrick et al [86]. Cellulose nanocrystals are elongated crystalline rod-like nanoparticles [80]. In literature it is possible to find also the term nanowhiskers (or just simply whiskers), instead of CNC. Generally, CNCs are described as nanofibers grown under controlled conditions that lead to the formation of high-purity single crystals [87]. The extraction of crystalline cellulosic regions, in the form of nanowhiskers, is a simple process based on the acid hydrolysis [83]. Rod-like CNC particles have interesting properties, in terms of biocompatibility, anisotropy, good optical transparency, low thermal expansion coefficient and, especially, high elastic modulus, comparable to that of steel [6] (Table II-2). These features guarantee to nanocellulose a wild range of applications and promising results in the composite technology.

Table II- 2. Young's Modulus values of cellulose derivatives [73].

Structure	Process	Component	Young's Modulus
		Wood	10 GPa
	Pulping		
		Single pulp fiber	40 GPa
	Hydrolysis followed by mechanical disintegration		
		Microfibrils	70 GPa
		Crystallites	250 GPa

CNC can be prepared from a variety of vegetable and animal sources, e.g., bacterial cellulose [88], algal cellulose (valonia) [89], hemp [90], tunicin [91], cotton [92] and wood [93]. It is possible to obtain CNC through the sulfuric hydrolysis of microcrystalline cellulose [94] and this was the type of CNC utilized in this research.

2.4.2   Melt-compounding process

Polymer composites and, in particular, thermoplastic composites can be obtained through the mechanical mixing of the filler with the solid polymeric matrix (in the absence of any solvent) above the softening point of the polymer. Traditional techniques, such as melt mixing using a twin-screw extruder or injection molding, can be utilized in this case. This method includes the further employment of the compression molding by the application of a high pressure and a temperature equal or higher than that of the melt-compounding to melt again the polymer composite and give it a sheet form. In Figure II-9 a schematic of the melt-compounding and compression molding cycle for polymer composites is represented.
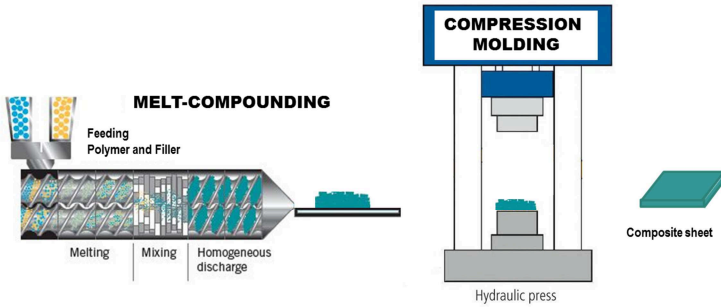
Figure II- 9. Schematic of the melt-compounding and compression molding cycle.

2.4.3 Solution mixing process

This method provides the direct mixing of the polymeric matrix and the filler, as the melt-compounding process but through the use of a solvent, in a solution system. This type of mixing is particularly suitable for preparation of polymer composites containing nano- or micron-sized fillers [95]. The fillers are predispersed in the polymer solution and casted in a mold. The further evaporation of the solvent from the filler/polymer solution leads to the formation of the composite film and allows a higher dispersion degree of the filler within the polymer matrix [96, 97] (Figure II-10).
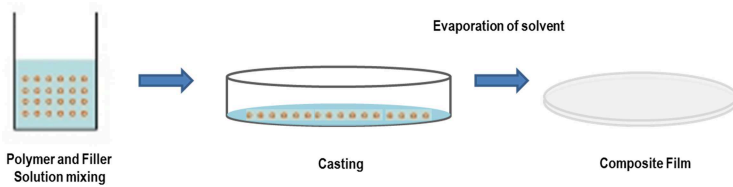
Figure II- 10. Schematic of the solution mixing process.

The shear force induced in the filler/polymer solution during the mixing process is much lower than that induced in the kneaded polymer melt in the absence of solvents [95]. For this reason, the solution-mixing method has an advantage over the melt-compounding method. On the other hand, polymer matrices that are not soluble in conventional low boiling point solvents cannot be used with this method.

Chapter III

Experimental

3.1   Materials

3.1.1   Paraloid B72

One of the selected polymeric matrices was a methyl-acrylate/ethylene methyl-acrylate (MA/EMA) copolymer (Figure III-1) (specific gravity= 1.15 g·cm^{-3}, mean molecular weight= 70000 g/mol) with the trade name of Paraloid B72$^®$, produced by Rohm and Hass (Germany) and provided by C.T.S. s.r.l. (Italy).
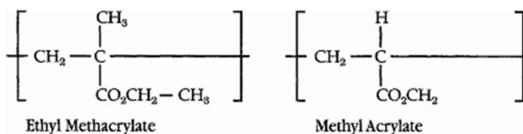
Figure III- 1. Chemical representation of Paraloid B72 macromolecule.

Paraloid B72 (PB72) is supplied in granular form (pellets) easily soluble in ketones, esters and aromatic hydrocarbons. This thermoplastic resin is one of the most used synthetic polymers in restoration. It is a general-uses resin usable as a protective coating for metals and other compact surfaces, as a consolidant of porous materials and as an adhesive. Paraloid presents a high photo-oxidation resistance and chemical stability. The principal properties of PB72 used in this research, according to the producer datasheet, are listed in Table III-1.

Table III- 1. Technical datasheet of Paraloid B72.

Physical form	Pellets
Bulk density, 25°C, lb/gal	9.6
Solubility parameter	9.3
Glass transition temperature, Tg, °C	40
Melting point, °C	70-75
Flowing point, °C	145-150
Ultimate hardness of clear films, KHN	10 to 11

3.1.2 Aquazol

Two different molecular weights of a poly 2-ethyl-2-oxazoline homopolymer (specific density= 1.07 g·cm^{-3}, mean molecular weight= 200000/500000 g/mol) with trade names of Aquazol 200$^®$ (AQ200) and Aquazol 500$^®$ (AQ500), respectively, were also selected as polymeric matrices. Additionally, AQ500 was used also for the production of nanocomposites. These products were produced by Polymer Chemistry Innovation (USA) and provided by C.T.S. s.r.l. (Italy). Figure III-2 shows the structure of the repeat unit of poly 2-ethyl-2-oxazoline.
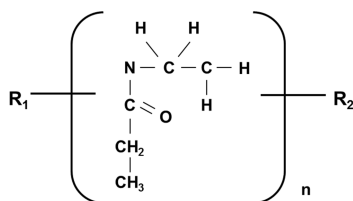
Figure III- 2. Structure of the repeat unit of poly 2-ethyl-2-oxazoline.

Aquazol 200 and 500 are water soluble adhesives, stable in weak acids and bases. They can be diluted in a broad range of organic solvents, thermally processed and extruded. These polymers present high flexibility and transparency, good thermal and aging resistance. The main properties of AQ200 and 500 are summarized in Table III-2.

Table III- 2. Technical datasheet of Aquazol 200 and 500.

Physical form	Pellets
Appearance	Light-yellow solid
Solubility	Freely soluble in water
pH in aqueous solution	6.8-7.4
Refractive index	1.52
Glass transition temperature, Tg, °C	69-71
Melting point, °C	212-392
Degradation onset, °C (TGA in air)	380

3.1.3   Cellulose microcrystals

Cellulose microcrystals, CMC, (specific gravity=1.56 g·cm^{-3}, mean molecular weight= 90000 g/mol) prepared through the reaction of cellulose with a water solution of strong mineral acid at boiling temperature, supplied by Sigma Aldrich (USA), were selected as microscale reinforcing filler. CMC particles consist of elongated flakes with an average length of about 24 µm and a diameter of about 10 µm (average L/D ratio of 2.4) (Figure III-3).

Figure III- 3. ESEM image of cellulose microcrystals.

3.1.4   Cellulose nanocrystals

Aqueous suspensions at 5.5 - 8.7 wt% of cellulose nanocrystals CNC, obtained through the sulfuric hydrolysis of microcrystalline cellulose powder (CMC) in the Wallenberg Wood Science Center (Sweden), were used as nanofiller. CNCs are rod-like particles 100-400 nm long, 5- 10 nm wide, with an average aspect ratio of 50 (Figure III-4).
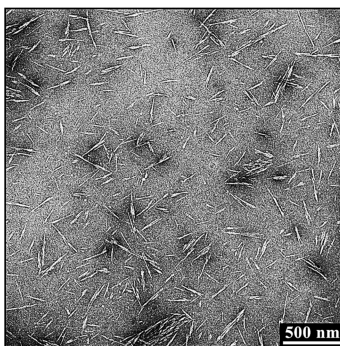
Figure III- 4. AFM image of cellulose nanocrystals.

3.2   Composites preparation

3.2.1   Microcomposites

Polymeric matrices pellets of PB72 and AQ200/500 and microcrystalline cellulose powder were dried under vacuum at 105 °C for 24 hours, before being processed. Microcomposite plates were prepared by melt mixing and compression molding. Paraloid B72 or Aquazol 200/500 (depends on microcomposites) and several amounts of CMC (from 5 wt% to 30 wt%) were physically mixed at room temperature and then melt-compounded in a Thermo Haake® internal mixer (T=160 °C, n=60 rpm, t=10 min) and following compression molded using a Carver® hot press (T=170 °C, p=4 MPa, t=5 min). In this way plane sheets of microcomposites with a thickness of around 1.3 mm were obtained. The internal mixer and the hot press used in this preparation are depicted in Figure III-5.
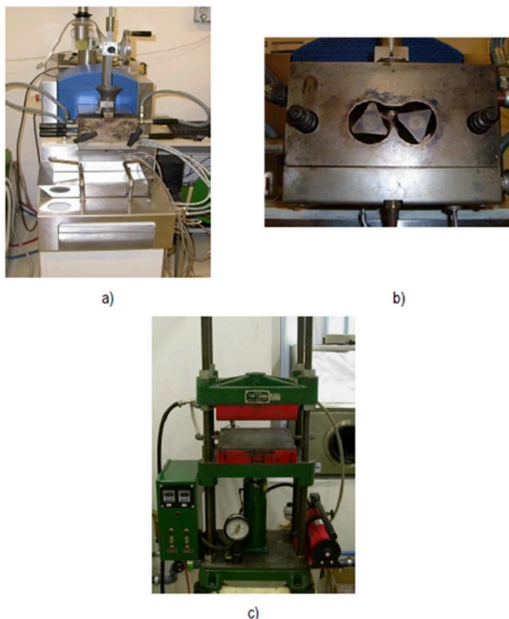
Figure III- 5. Pictures of (a) Haake® internal mixer (b) mixing chamber of the Haake® internal mixer and (c) Carver® hot press.

After processing, microcomposites samples were stored in vacuum sealed bags in order to avoid water uptake.

3.2.2 Nanocomposites

Thin films of Aquazol 500 based composites filled with cellulose nanocrystals with an average thickness of 250 μm and a filler content of 5 wt%, 10 wt% and 30 wt%, were prepared by solution mixing and casting method. Aqueous suspensions at 5.5 - 8.7 wt% of cellulose nanocrystals were mixed to the water solution of AQ500 under magnetic stirring at room

temperature. Nanocomposites solutions were mechanically mixed for 3 min at room temperature. All solutions were undergone to vacuum degassing using a vacuum pump until the complete removal of the excess air. Then it was possible to cast solutions in plastic circular plates and dry them in a vacuum oven at 40°C until the complete solvent evaporation. Nanocomposites films were stored under vacuum in a desiccator.

Films of AQ500 based composites filled with 5 wt%,10 wt% and 30 wt% of CMC and having an average thickness of 250 μm were produced fallowing the same method in order to perform the comparison between micro- and nanocomposites performances.

3.2.3   Samples designation

All micro- and nanocomposites were designated indicating the type of matrix, the type of filler and its amount. For instance, a sample of Paraloid B72 filled with 5 wt% of cellulose microcrystals is indicated as PB72-CMC-5, while AQ500-CNC-5 represents a sample of Aquazol 500 filled with 5 wt% of cellulose nanocrystals. Samples subjected to conditioning were denoted indicating also their conditioning level: W=conditioned (wet) state and D=dry state. For instance, AQ200-CMC-30$_D$ identifies a composite sample with a CMC amount of 30 wt% in the dry state.

3.3   Characterization of micro- and nanocomposites

3.3.1   **Microstructural charactectization**

3.3.1.1   SEM observations

Environmental scanning electron microscopy (ESEM) technique was used to evaluate the dimension and distribution of microcellulose particles within polymer matrices. ESEM observations on neat CMC powder and on cryofractured surfaces of composites samples were carried out by a Philips XL30 environmental scanning electron microscope under an accelerating voltage of 10 kV.

Microstructural analysis of micro- and nanocomposites made by the solution mixing method, were carried out through a Zeiss Supra 40 high resolution FESEM microscope with an accelerating voltage of 1 kV and a beam aperture of 20 μm.

Before observation, all samples were immersed in liquid nitrogen and fractured.

3.3.1.2   Evaluation of filler size

The dimensional distribution of CMCs before and after the melt compounding process was evaluated by a Wild Heerbrugg Leica optical microscope. For the determination of CMC size after mechanical mixing, samples of Paraloid B72 and Aquazol 500 based formulations at the highest amount of CMC were dissolved in acetone at 30 °C for 1 h, and the resulting flakes were then dried under vacuum at 105 °C for 2 hours. At least 200 measurements were performed on the resulting micrographs by an image analysis software (ImageJ®). For the sake of brevity, only one type of Aquazol matrices with the highest molecular weight was select for this test.

3.3.1.3   Differential scanning calorimetry

Differential scanning calorimetry (DSC) tests were performed by a Mettler DSC30 calorimeter. Samples of about 12 mg were analyzed under a nitrogen flow of 150 ml·min^{-1}, applying a first heating stage from 0 to 250°C linked to a cooling stage from 250 °C to 0 °C and to a second heating stage until 250 °C at 10°C·min^{-1}. For CMC and CNC solution mixed samples the same experimental parameters were used, but heating stages from 0°C to 120°C and a cooling step from 120°C to 0°C were selected. The glass transition temperature (T_g) was evaluated as the inflection point in the DSC curves.

3.3.1.4   Thermogravimetric analysis

The thermal stability of all micro- and nanocomposites was investigated through thermogravimetric analysis (TGA), by using a Mettler TG50 thermobalance in a temperature interval between 40 and 700 °C, at a heating rate of 10°C·min^{-1} and under a nitrogen flow of 150 ml·min-1. The onset temperature (i.e. the temperature associated to a mass loss of 5%) and the residual mass at 700 °C were determined. The maximum degradation temperature was evaluated from the main peak of mass loss rate curves.

3.3.2   Physical charactectization

The optical characterization of melt-compounded microcomposites through the visual assessment of transparency, CIELAB color measurements and UV-vis analysis was conducted on thin films of CMC composites with a reduced thickness of about 100 μm. In order to reach this reduced thickness, a further compression molding at 150 °C under a pressure of 4 MPa for 10 min, was required on the samples produced as described in par. 3.2.1.

3.3.2.1 Water sorption tests

Paraloid and Aquazol based melt-compounded microcomposites samples with an average thickness of 1.3 mm and bulk samples of CMC produced pressing the powder with a glass slide into a metal squared mold with a thickness of 1.2 mm were conditioned at 23°C and 55% of relative humidity in a chamber with a super-saturated solution of $Mg(NO_3)_2 \cdot 6H_2O$ for 30 days. This is the humidity level recommended in museums, churches and historical buildings for the optimal artwork conservation and fruition. It was selected to assess the effect of CMC on the water sorption tendency of neat matrices under a common service condition for cultural heritage. The moisture absorption was evaluated by monitoring the change of weight of five specimens for each formulation, by using a Gibertini E42 electronic balance with a resolution of 10^{-4} g, until a constant weight was reached. According to ASTM D570 standard, the moisture content (M%) was calculated comparing the initial weight of the samples (w_0) and the weight at a time t (w_t) according to Equation (1) :

$$M\% = 100 \frac{(W_t - W_0)}{W_0} \qquad (1)$$

Moreover, according to ASTM D5229 standard, the final moisture content (M_{MAX}) and the time required to reach the equilibrium water content (t_s) were evaluated.

3.3.2.2 Optical transparency assessment

Optical transparency of all micro- and nanocomposites films was evaluated through digital pictures taken by a professional Canon EOS 550D digital

camera equipped with a zoom lens EF-S 18-135 mm, at a distance of 20 cm from each specimen.

3.3.2.3   CIELAB color measurements

The color of CMC thin films samples obtained from melt-compounded composites plates was quantified by a portable spectrophotometer (Konica Minolta® model CM-2600d) with a diameter target area of 8 mm and CM-S100w (SpectraMagicTM NX) software. Three readings were performed in different zones of each specimen placed on a white sheet. Color measurements were analyzed in accordance to the CIELAB color system [98]. Each color is described through three Cartesian coordinates: L*, lightness or luminosity of color, from 0 (absolute black) to 100 (absolute white); a*, variation in redness–greenness (positive a* is red and negative a* is green); and b*, change in yellowness–blueness (positive b* is yellow and negative b* is blue). Another important value is dE·ab, the total color difference between a target and different samples, in this case each of the three neat matrices and the relative CMC composites, respectively. dE·ab values were provided by the CM-S100w software.

3.3.2.4   UV-vis spectroscopy analysis

Relative transmittance spectra of all micro- and nanocomposites films were recorded with a Jasco570 UV-Vis-NIR spectrophotometer, at a spectral wavelength range of 250-800 nm.

3.3.3　Mechanical charactectization

3.3.3.1　Hydrothermal conditioning

Before mechanical tests, all samples of micro- and nanocomposites were dried at 50 °C for 24 h in a vacuum oven. Microcomposites prepared by melt-compounding were also tested after being conditioned at T= 23°C and RH= 55% in order to assess the mechanical response of these materials under recommended hydro-thermal conditions for artworks conservation.

3.3.3.2　Dynamic mechanical thermal analysis (DMTA)

In order to assess the viscoelastic properties of all micro- and nanocomposites dynamic mechanical thermal analysis (DMTA) were performed by using DMA Q800 device by TA Instruments under tensile configuration. For CMC melt-compounded samples, at least three rectangular specimens 15 mm long, 5 mm wide and 1.3 mm thick were tested, while for CMC and CNC solution mixed samples the thickness of the examined rectangular specimens was 0.25 mm. A temperature range between -10 °C and 150 °C, a heating rate of 3 °C·min-1 and a frequency of 1 Hz were utilized. To assure a linear viscoelastic behavior, the strain amplitude was fixed at 0.05%. The trends of the storage modulus (E'), loss modulus (E") and loss tangent (tanδ) as a function of the temperature were registered. Moreover, coefficients of linear thermal expansion (CLTE) were determined from the evaluation of the slope of thermal strain curves below T_g in the glassy state ($CLTE_g$) and above T_g in the rubbery state ($CLTE_r$). For melt-compounded composites in the dry state the following temperature ranges were used:

- for Paraloid/CMC composites, $CLTE_g$ and $CLTE_r$ were determined in temperature intervals between 0 °C and 40 °C and between 50 °C and 55 °C, respectively.
- for Aquazol/CMC composites, $CLTE_g$ and $CLTE_r$ were calculated in temperature intervals between 0 °C and 55 °C and between 70 °C and 75 °C, respectively.

For conditioned melt-compounded composites the following temperature ranges were utilized:

- for Paraloid/CMC composites, $CLTE_g$ and $CLTE_r$ were evaluated in temperature intervals between 0 °C and 35 °C and between 50 °C and 55 °C, respectively.
- for Aquazol/CMC composites, $CLTE_g$ and $CLTE_r$ were determined in temperature intervals between 0 °C and 25 °C and between 30 °C and 35 °C, respectively.

For micro- and nanocomposites obtained by solution mixing method the following temperature ranges were used:

- for CMC composites, $CLTE_g$ and $CLTE_r$ were estimated in temperature intervals between 0 °C and 40 °C and between 65 °C and 75 °C, respectively.
- for CNC composites, $CLTE_g$ and $CLTE_r$ were investigated in temperature intervals between 0 °C and 40 °C and between 70 °C and 80 °C, respectively.

3.3.3.3   *Quasi-static tensile tests*

Quasi-static tensile tests were carried out on ISO 527 type 1BA samples of melt-compounded CMC composites (gage length 30 mm, width 5 mm, distance between the grips 55 mm, thickness 1.3 mm) by means of an Instron® 4502 universal testing machine, equipped with a 1kN load cell. Tensile tests for the evaluation of the elastic modulus were performed at a crosshead speed of 0.25 mm·min^{-1} (strain rate equal to 0.02 min^{-1}) setting a maximum axial deformation level of 1%. The strain was recorded by using a resistance extensometer Instron® model 2620-601 (gage length of 12.5 mm). According to ISO 527 standard, the elastic modulus was evaluated at room temperature as a secant value between deformation levels of 0.05% and 0.25%. Ultimate tensile properties (stress at break σ_B, and strain at break ε_B) were determined by tensile tests at break, executed at room temperature at a crosshead speed of 10 mm/min, without using the extensometer. At least five specimens were tested for each sample. For wet samples of Aquazol composites having a rubber-like behavior, a secant elastic modulus at 10% of strain was determined since it was not possible to use the extensometer. Additionally, the tensile energy to break (TEB) was calculated by integration of the area under the stress-strain curves corresponding to the total energy absorbed per unit volume of each specimen up to fracture.

3.3.3.4   *Plane-strain fracture toughness and strain energy release tests*

A deeper investigation of the fracture behavior of melt-compounded composites was carried out through the linear elastic fracture mechanics methods based on the determination of the plane-strain fracture toughness parameters K_{IC} and G_{IC}. An Instron universal testing machine, equipped with a 1kN load cell was used. According to ASTMD 5045 standard, single edge

notched bending samples (SENB), 35 mm long, 8 mm wide and 4 mm thick were tested at a crosshead speed of 10 mm·min^{-1}. Samples were pre-notched with a sharp notch of 4 mm in depth, with a notch tip radius of less than 10 microns. Both critical stress intensity factor (K_{IC}) and critical strain energy release rate (G_{IC}) values were determined as samples of at least five specimens.

3.3.3.5 Creep tests

In order to assess the effect of CMC and CNC on the elongation resistance of neat matrices, creep tests were performed at 30 °C by a TA Instrument DMA Q800 machine under tensile configuration, applying a constant stress value (σ_0) fixed at about 10% of the stress at break of neat matrices. Rectangular specimens 15 mm long, 5 mm wide and with a thickness of 1.3 mm for melt-compounded CMC composites and 0.25 mm for micro and nano solution mixed composites were tested for a total time of 3600 s. Creep compliance D(t), values were determined as the ratio between the time dependent deformation ε(t) and the applied stress (σ_0).

3.4 Consolidation of degraded wood

3.4.1 Preparation and application of consolidant solutions

Paraloid B72 neat matrix and corresponding microcomposites with 5 wt% and 30 wt% of CMC prepared by melt-compounding and compression molding were dissolved in acetone solutions at 10 wt% concentration. These consolidant solutions were applied on two species of historical degraded wood (18th century). The wood types selected for this work were a hardwood Persian walnut (Juglans regia) and a softwood European silver fir (Abies

alba). The two wood samples presented different conservation conditions. The Persian walnut exhibited a critical and advanced biological decay with evident holes and tunnels made by larval worms that interested also the inner part of the wood. Larvae holes and galleries were visible also in the silver fir but not as diffused as in the walnut wood. These two historical woods, representing different taxonomic families and degradation degrees, were selected to prove the consolidating properties of the neat Paraloid and the resulting microcomposites in various situations. Prismatic specimens of each wood species (5mm wide, 5mm tick and 80mm long) were impregnated with consolidant solutions by means of a brush. Two cycles of application on each face of specimens were performed and the amount of consolidant deposited was assessed by a Gibertini E42 electronic balance with a resolution of 10^{-4} g. Approximately, the same amount of consolidants, about 130 mg, was applied on each face. As a comparison, all tests were even carried out on untreated modern samples of the same types of wood in a well preserved state.

3.4.1.1   Samples designation

Wood samples were identified through their conservation state (UW represents the undamaged modern wood; DW is the degraded historical wood), and the type of formulation used for the consolidation treatment (T0 refers to neat Paraloid, T5 and T30 refer to Paraloid based composites with 5wt% and 30 wt% of CMC, respectively).

3.4.2   Brookfield tests

In order to evaluate the possible viscosity change of the matrix after the introduction of CMCs, rheological measurements were performed on

unfilled and filled Paraloid acetone solutions in a Brookfield RVT coaxial viscometer, with an inner diameter of 17 mm and an outer diameter of 19 mm, at a temperature of 25°C controlled by a thermostatic chamber. A shear rate interval between 0.1 and 15 rad·s^{-1} and a sample volume of 8 mL were used.

3.4.3   Physical characterization

After the air-drying of the solvent, wood samples for physical characterization were dried under vacuum at 105 °C until the achievement of a constant weight and then conditioned in a climatic chamber (ATS FAAR mod. CU/220-35) at a temperature of 23°C and a relative humidity of 65% till a constant weight was reached. A relative humidity level of 65% is the most common wet condition for wood that, consequently, presents a moisture content at equilibrium of about 12-15% [99, 100].

3.4.3.1   Gravimetric analysis

Weight and volume changes of at least 5 specimens for each type of wood were monitored by using a Gibertini E42 electronic balance with a resolution of 10^{-4} g and a Mitutoyo digital caliper, respectively. The moisture content (M%), the oven-dry density (ρ_0), the density at 65% of relative humidity level (ρ_{12}) [101, 102], and the volumetric swelling (S) [103] were calculated at the equilibrium point according to the following equations:

$$M\% = 100\frac{(W_t - W_0)}{W_0} \qquad (1)$$

$$\rho_0 = \frac{W_0}{V_0} \qquad (2)$$

$$\rho_{12} = \frac{W_t}{V_t} \tag{3}$$

$$S = 100\frac{(V_t - V_0)}{V_0} \tag{4}$$

where: W_t and V_t are the weight and volume of conditioned specimens at the equilibrium point and W_0 and V_0 are the initial dry weight and the initial dry volume of specimens, respectively.

3.4.3.2   Mercury intrusion porosimetry

The percentage of total porosity (P_{TOT}) and the radius of macro- and micropore of all examined woods were detected by a Mercury Intrusion Porosimeter 2000 (FISONS Instruments). Samples of about 0.2 g were immersed in the non-wetting mercury. The increase of the pressure in the capillary allowed the intrusion of mercury in the cavities of samples. The pore radius (r) was estimated through the Washburn equation (Equation 5), that gives the relationship between the analysis pressure and this parameter. The total porosity of each sample was determined as the ratio between the volume of mercury intruded into the sample at the highest analytical pressure and the initial external volume of the sample [104].

$$r = -\frac{2\gamma \cdot \cos\theta}{P} \tag{5}$$

where r is the pore radius, γ is the surface tension of mercury (0.48 N/m), θ is the wetting angle of mercury (141.3 °C) and P is the applied pressure.

3.4.3.3 Assessment of the penetration degree of consolidant solutions

Before and after all consolidating treatments, surfaces and long cross-sections of decayed wood samples were analyzed through optical microscope observations and Fourier transform infrared spectroscopy analysis FTIR in order to evaluate the penetration degree of all consolidant solutions.

3.4.3.3.1 Optical microscope observations

For optical microscope observations of surfaces and long cross-sections of decayed wood samples an optical microscope NIKON SMZ25 was utilized.

3.4.3.3.2 Fourier transform infrared spectroscopy (FTIR)

FTIR analysis of surfaces and long cross-sections of decayed wood samples were carried out by a FTIR spectrometer Varian 4100 (Excalibur Series) equipped with a Golden Gate diamond (Graseby Specac) for ATR analysis. A scanning range from 4000 to 400 cm^{-1} was utilized.

3.4.4 Mechanical characterization

Before testing, samples were conditioned at 23°C and 55% of relative humidity in a chamber with a super-saturated solution of $Mg(NO_3)_2 \cdot 6H_2O$ until a constant weight was reached.

3.4.4.1 Three points flexure tests

Three points flexure tests (ASTM D143) on at least 20 rectangular wood specimens (width= 5 mm, thickness= 5 mm, span length= 70 mm) for each set of samples were performed in order to investigate the effect of CMC on

the flexure behavior of Paraloid. These tests were conducted by means of an Instron 4502 universal testing machine, equipped with a 1 kN load cell. A crosshead speed of 1.3 mm/min was adopted. The flexural modulus (E_f), the maximum flexural stress ($\sigma_{MAX,f}$) and the maximum flexural strain ($\varepsilon_{MAX,f}$) were evaluated according to the following equations:

$$\sigma_{MAX,f} = \frac{3}{2}\frac{F_{MAX}L}{bh^2} \qquad (6)$$

$$\varepsilon_{MAX,f} = \frac{6hu}{(L/2)^2} \qquad (7)$$

$$E_f = \frac{FL^3}{4bh^3u} \qquad (8)$$

where F_{MAX} (N) is the load at break, L (mm) the span length, F (N) and u (mm) are any load and its displacement below the proportional limit, respectively and b and h (mm) are the width and the height of specimens, respectively.

3.4.4.2   Charpy impact tests

Charpy impact tests were conducted by a Ceast instrumented impact pendulum on at least 20 rectangular specimens (width= 5 mm, thickness= 5 mm, span length= 40 mm) for each set of wood. A striker mass of 1.187 kg, an initial impact angle of 84° and a data acquisition rate of 2000 points per second were utilized. Samples were impacted at a speed of 2 m·s^{-1} with a maximum impact energy of 2.37 J. Through the integration of force-displacement curves it was possible to estimate the specific energy adsorbed at the crack initiation (U_i), corresponding to the energy adsorbed up to the maximum load, the specific energy adsorbed during the crack propagation

(U_p) and the total specific absorbed energy (U_{TOT}), that is the sum of Ui and Up. Additionally, a ductility index (DI), was calculated as the ratio between U_i and U_p to determine the energy absorption capability of wood samples before and after treatments, during fracture propagation [105].

3.4.4.3   ShoreD hardness tests

The surface hardness of wood samples was determined by an ATS FAAR ShoreD hardness tester. According to ASTM D2240, three penetrations on each face of all wood specimens already tested by flexural tests were performed. Radial and tangential surfaces were analyzed.

3.4.4.4   Microstructural analysis

Microstructural analysis of fracture surfaces of impacted wood samples were carried out by a NIKON SMZ25 optical microscope Thanks to the instrument software, 3D profiles of failure surfaces were investigated in order to assess the effect of CMC introduction on the fracture mode of each group of wood.

3.5   Lining of oil paintings on canvas

3.5.1   Rheological tests

Before application, dynamic rheological tests were performed on Aquazol based composites filled with CMC by using an Anton Paar MCR 301 rheometer in plate-cone configuration. A maximum shear strain (γ_0) of 1% and an angular frequency range between 0.05 and 300 s^{-1} were used. Conditioned samples (T= 23°C, RH= 55%) with an average diameter of 25

mm and an average thickness of 0.8 mm were examined at 60°C, the temperature generally used to apply the lining adhesive on canvases [106-108].

3.5.2 Preparation of adhesive joints

In order to simulate the consolidation of an ancient oil paintings substrate through the canvas lining, thin films of melt-compounded Aquazol/CMC composites with an average thickness of 100 μm and CMC and CNC solution mixed composites 250 μm thick were applied as lining adhesives. Single-lap adhesive joints (12.7 mm long and 25 mm wide) connecting two kinds of canvas were obtained by applying a pressure of 1MPa for 5 min at 60 °C. The two canvases used for this application were a pure linen fabric, English canvas, made of boiled and wet spun flax yarn, with a weight of 170 g/m^2, a yarn count of 22X20 and a railroaded pattern, representing the original oil painting canvas, and a uncoated woven polyester, Sintel, with a weight of 260 g/ m^2, a yarn count of 22X22 and a railroaded pattern, utilized as lining textile. The English canvas has an average thickness of 0.35 mm, while, the average thickness of the woven polyester is of 0.45 mm. In this way rectangular specimens 200 mm long and 25 mm wide were produced to be tested under single-lap shear configuration (Figure III-6).
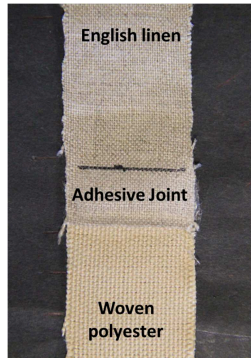
Figure III- 6. Example of a single-lap adhesive joint with textile adherends

3.5.3   Single-lap shear tests

In order to investigate the possible stabilizing effect due to the dispersion of micro- and nanoreinforcements into very hygroscopic polymers, and the consequent increment of their dimensional stability, single-lap shear tests were conducted. Before testing, all samples were conditioned for 48h at 23°C of temperature and 55% of relative humidity in a chamber with a super-saturated solution of $Mg(NO_3)_2 \cdot 6H_2O$. Single-lap shear tests in quasi-static and creep conditions (Figure III-7) were carried out by an Instron® 4502 universal testing machine, equipped with a 10kN load cell, using a crosshead speed of 10 mm/min to determine the adhesive shear strength (τ_B), calculated as the ratio between the maximum force and the overlapping area. The joint displacement (u), investigated in the gauge length of each sample, were determined applying a constant stress (τ_0), corresponding to about 50% of the shear stress at break (τ_B) of the neat matrix adhesive samples, at a

temperature of 30 °C, for 3600 s. At least five specimens were tested for each sample and each condition.
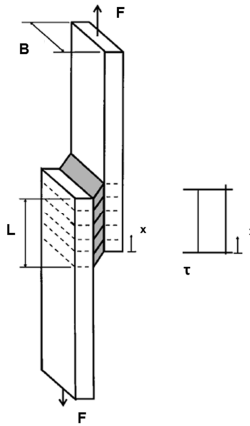
Figure III- 7. Schematic of testing parameters

3.5.4   Microstructural analysis

Observations of the fracture surface of adhesive joints were carried out through a Wild Heerbrugg Leica optical microscope at a magnification of 40X.

Chapter IV

Results and Discussion

Part of this chapter has been published in:

4.1 Characterization of microcomposites

4.1.1 Microstructural characterization

Microstructural characterization was carried out on microfiller, neat matrices and resulting microcomposites in order to assess the dispersion degree of CMCs within the selected polymer matrices and the possible correlation between microstructure and final properties of experimental composites.

4.1.1.1 ESEM observations

Analyzing ESEM images of CMC powder reported in Figure IV-1(a-b), it is possible to observe the irregular shape of CMC particles similar to elongated flakes with an average length of about 24 μm, a diameter of about 10 μm and an average aspect ratio of 2.4.

(a) (b)
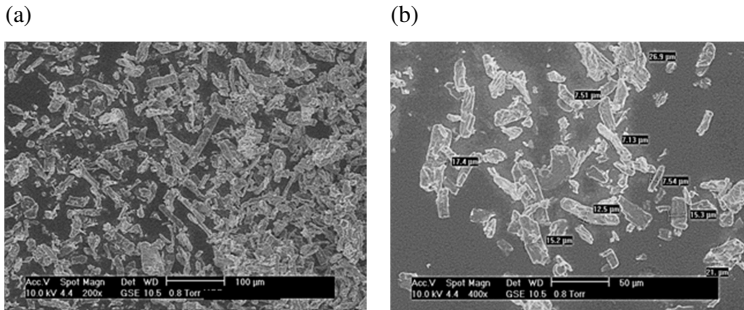
Figure IV- 1. ESEM images of microcrystalline cellulose particles.

Figures IV-2(a-e), IV-3(a-e) and IV-4(a-e) show ESEM micrographs of cryofractured surfaces of neat Paraloid and Aquazol matrices and resulting microcomposites samples.

(a)

(b)

(c)

(d)

(e)
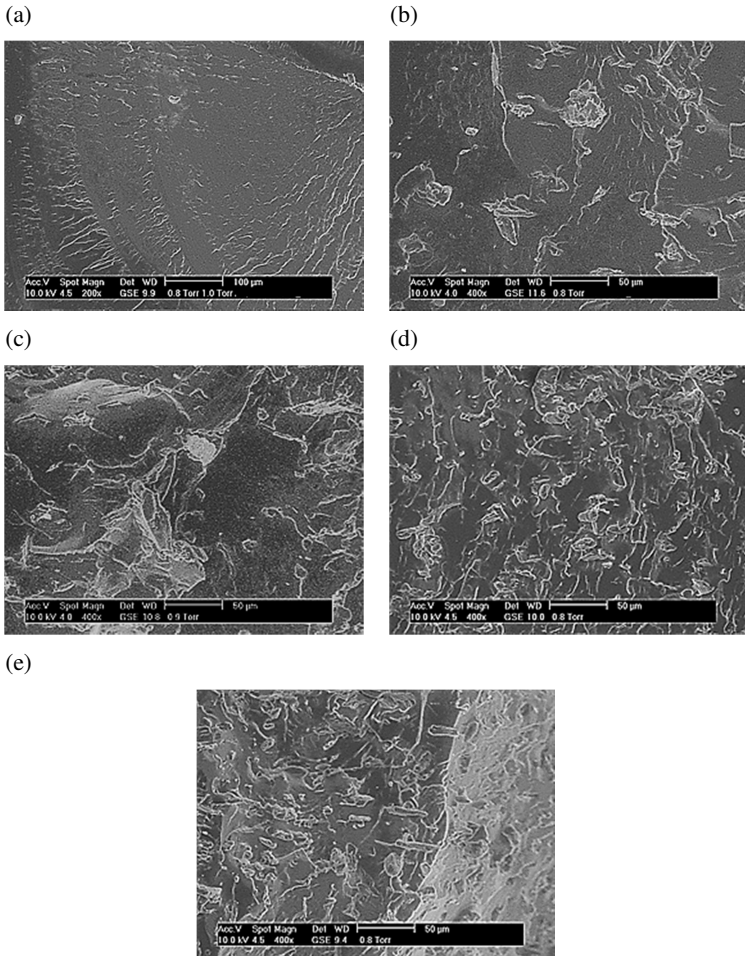
Figure IV- 2. ESEM images of cryofractured surfaces of (a) neat Paraloid B72 matrix and (b-e) resulting composites with 5wt%, 10wt%, 20wt% and 30wt% of CMC, respectively.

(a)

(b)

(c)

(d)

(e)
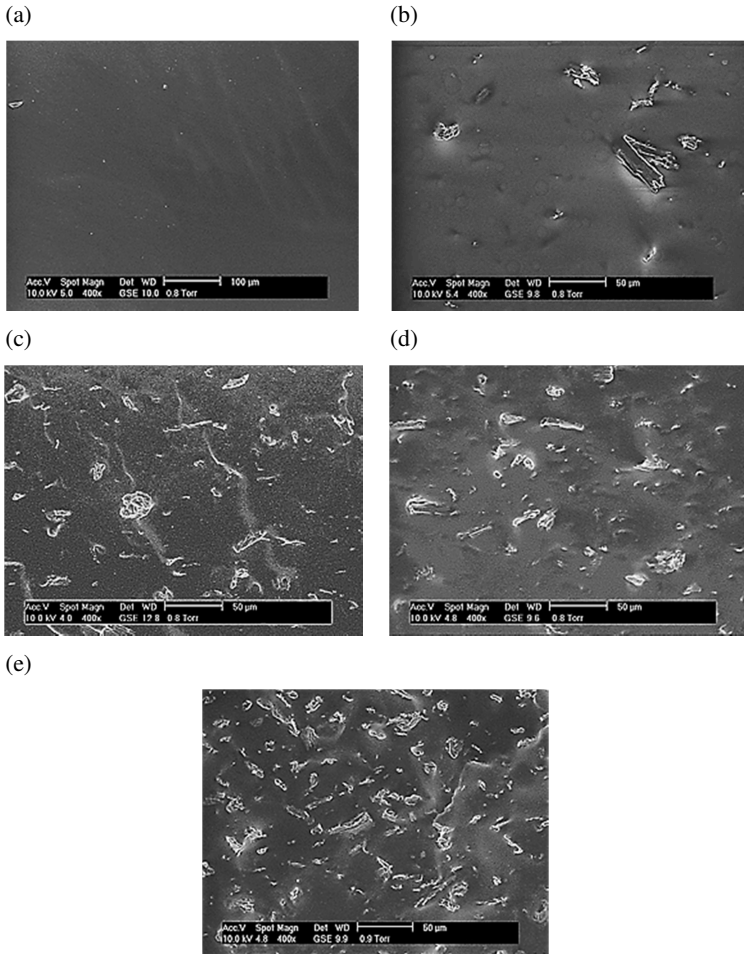
Figure IV- 3. ESEM images of cryofractured surfaces of (a) neat Aquazol 200 matrix and (b-e) resulting composites with 5wt%, 10wt%, 20wt% and 30wt% of CMC, respectively.

(a)

(b)

(c)

(d)

(e)
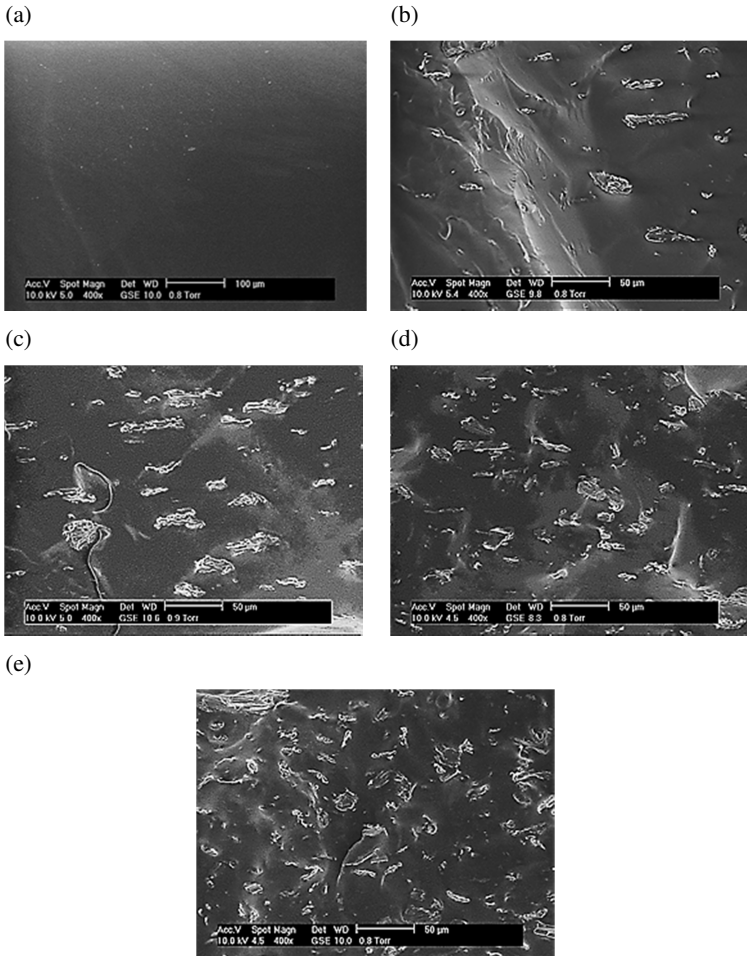
Figure IV- 4. ESEM images of cryofractured surfaces of (a) neat Aquazol 500 matrix and (b-e) resulting composites with 5wt%, 10wt%, 20wt% and 30wt% of CMC, respectively.

Paraloid and Aquazol 200-500 exhibit a relatively flat cryofractured section, typical of brittle materials. From micrographs of composites, it is evident that CMC flakes appear to be uniformly dispersed within the three matrices even at high filler loading without any preferential orientation. Individual flakes can be detected without a substantial filler aggregation. No evident debonding phenomena can be observed. For PB72 samples an increase of the roughness of fracture surfaces with increasing of the CMC content is visible, making harder a clear detection of filler flakes. Comparing the fracture surfaces of Paraloid and Aquazol composites, it can be easily noticed that PB72 filled samples exhibit the highest surface corrugation degree, evidence of a possible better polymer/CMC interaction.

4.1.1.2   *Evaluation of filler size*

The reinforcing capability of filler into composites is strictly related to its size and its aspect ratio. The evaluation of possible dimensional variations of the filler size induced by the melt compounding process was conducted. Optical microscope images of CMC flakes extracted from solubilized composites (an example of these images is reported in Figure IV-5(a-b)) were analyzed in order to determine the dimensional distributions of the length, the width and the aspect ratio of CMC extracted from Paraloid and Aquazol 500 composites (Figure IV-6(a-c), IV-7(a-c) and IV-8(a-c), respectively).

(a)

(b)
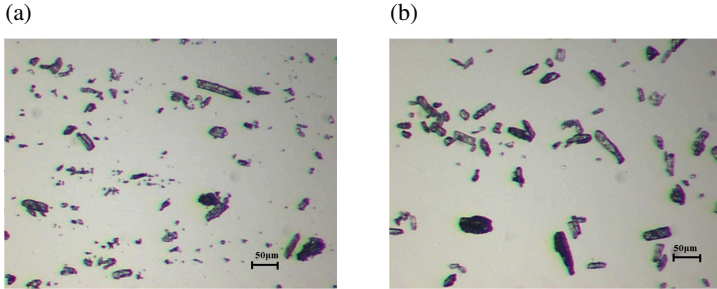
Figure IV- 5. Optical microscope images of CMC flakes. (a) Before and (b) after melt-compounding and compression molding process.

(a)

(b)

(c)
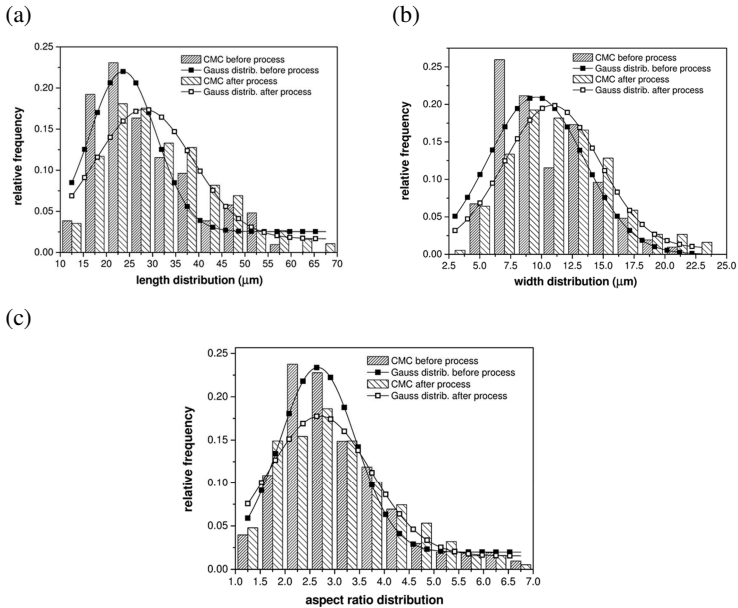
Figure IV- 6. CMC size distribution before and after processing cycle from Paraloid composites samples. (a) Length distribution, (b) width distribution, (c) aspect ratio distribution.

(a)

(b)

(c)
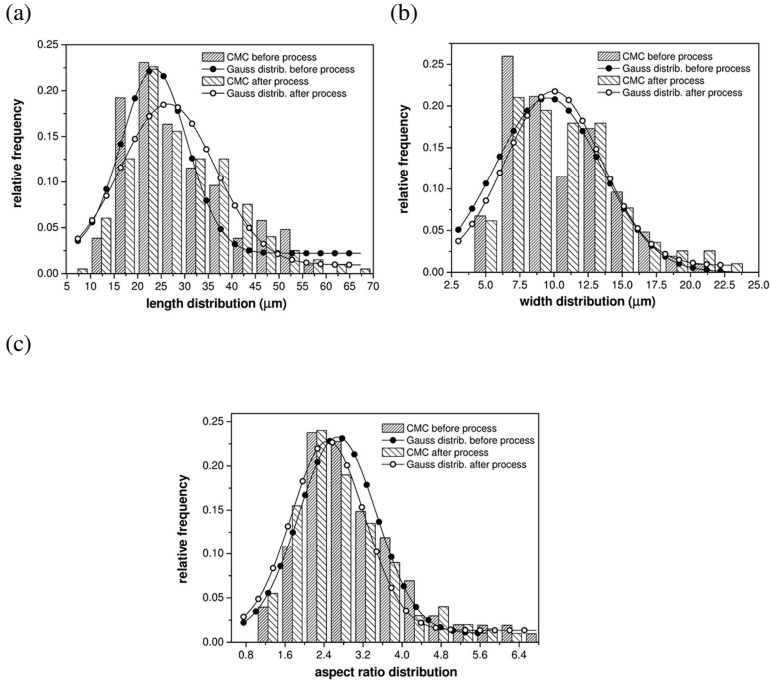
Figure IV- 7. CMC size distribution before and after processing cycle from Aquazol 500 composites samples. (a) Length distribution, (b) width distribution, (c) aspect ratio distribution.

After melt compounding the size distribution of CMCs within all polymers is slightly broader, with a fraction of particles having length and width slightly higher than un-compounded flakes, but their aspect ratio is practically the same. This point could be explained considering the mechanical deformation induced at elevated temperature by the rotors of the melt compounder and/or the hot pressing on the CMC particles. Considering the resulting aspect ratio of CMCs before and after process and the

experimental error associated to this kind of measurements, it can be concluded that the processing step does not markedly reduced the average dimensions of CMC particles in the composites. As reported in the literature, natural fibers can maintain their specific aspect ratio during melt processing thanks to their high flexibility in comparison to more brittle fillers such as glass or carbon fibres [109, 110].

4.1.1.3 Differential scanning calorimetry (DSC)

In Figures IV-8(a-b), IV-9(a-b) and IV-10(a-b) DSC thermograms of neat matrices and corresponding composites collected during the first and the second heating stage are reported. In Table IV-1 glass transition temperatures of each set of microcomposites collected during heating and cooling stages are summarized.

(a)   (b)
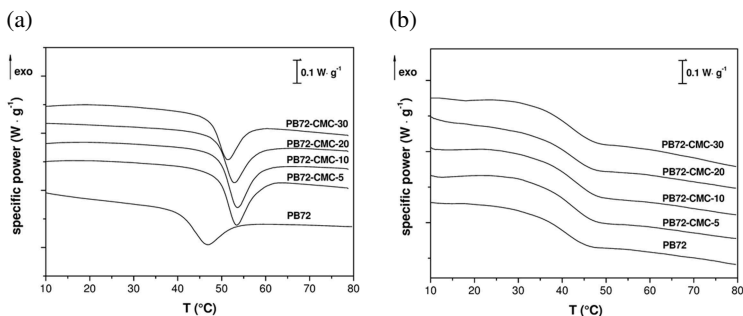
Figure IV- 8. DSC thermograms of neat PB72 and corresponding composites. (a) First heating stage, (b) second heating stage.

(a)

(b)
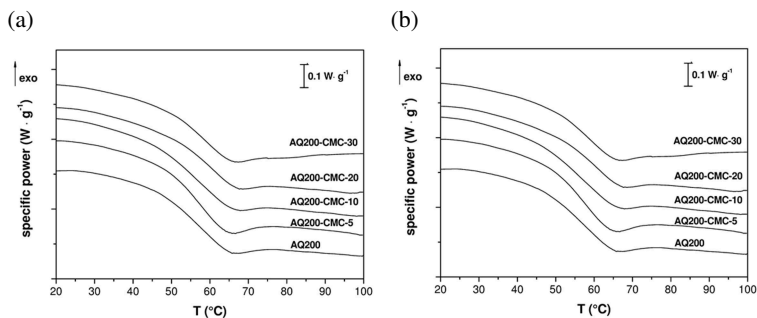
Figure IV- 9. DSC thermograms of neat AQ200 and corresponding composites. (a) First heating stage, (b) second heating stage.

(a)

(b)
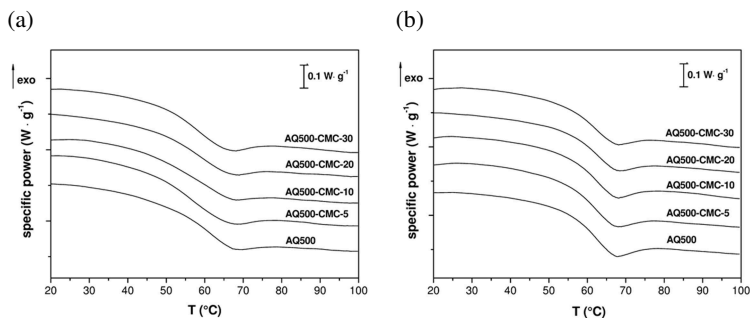
Figure IV- 10. DSC thermograms of neat AQ500 and corresponding composites. (a) First heating stage, (b) second heating stage.

Table IV- 1. Glass transition temperatures (T$_g$) of neat matrices and resulting composites from DSC tests.

Sample	T$_g$ °C		
	First heating	**Cooling**	**Second heating**
PB72	40.5	31.4	39.8
PB72-CMC-5	48.4	34.0	42.6
PB72-CMC-10	46.7	35.6	41.9
PB72-CMC-20	47.9	34.7	40.9
PB72-CMC-30	46.5	32.9	41.0
AQ200	55.9	48.0	58.9
AQ200-CMC-5	55.5	46.7	58.4
AQ200-CMC-10	55.4	47.2	58.6
AQ200-CMC-20	56.8	47.6	58.6
AQ200-CMC-30	56.4	46.4	58.7
AQ500	56.8	48.5	59.9
AQ500-CMC-5	56.6	47.7	59.7
AQ500-CMC-10	57.6	49.2	59.7
AQ500-CMC-20	57.1	47.3	60.1
AQ500-CMC-30	56.8	48.5	60.0

All specimens show the typical trend of amorphous polymers, with the presence of an inflection point due to the glass transition. In the first heating it is possible to note that CMC introduction in PB72 leads to an increase of the glass transition temperature. For instance, PB72-MCC-5 presents a T$_g$ enhancement of about 8 °C in comparison to the neat resin. On the other hand, for both Aquazol based composites no significative changes in the mobility of polymeric chains due to CMC presence is detected and only a

slight increase of the glass transition temperature can be observed. In cooling and second heating scans, all composites report similar values of T_g as their corresponding neat matrices regardless of the increase of CMC content.

Relative T_g trends as function of filler content were evaluated by dividing temperature values of each composite by those of their corresponding neat matrix in order to compare the effect of CMC on examined polymers. In Figure IV-11(a-b) relative T_g trends of PB72, AQ200 and AQ500 in the first and second heating stage that reported the most significant results, are shown. It is evident how CMC is able to increase the glass transition temperature of Paraloid independently on the CMC loading, while there are practically no effects on Aquazol polymers. This could be explained through the level of polymer-filler interaction, that for PB72-CMC is higher than AQ200/500-CMC, leading to a more pronounced action of CMCs on PB72 polymeric chains and consequently on its T_g [111].

(a)   (b)
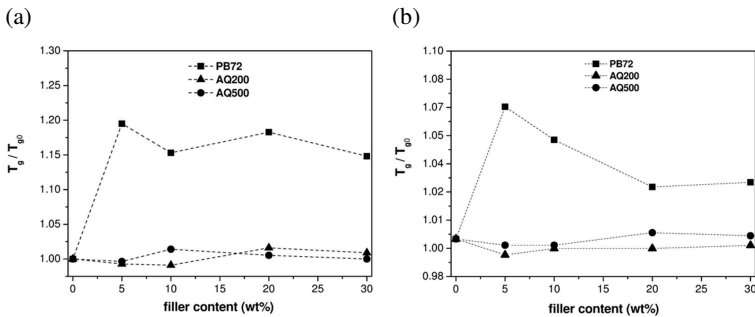
Figure IV- 11. Relative glass transition temperature (T_g) trends of Paraloid, Aquazol 200 and 500 based composites. (a-b) First and second heating stage.

4.1.1.4   Thermogravimetric analysis (TGA)

TGA thermograms and derivative of the mass loss curves of constituents and corresponding composites are reported in Figure IV-12(a-b) for PB72, IV-13(a-b) for AQ200 and IV-14(a-b) for AQ500. The most important parameters regarding the thermal stability of the investigated materials are summarized in Table IV-2.

(a)

(b)
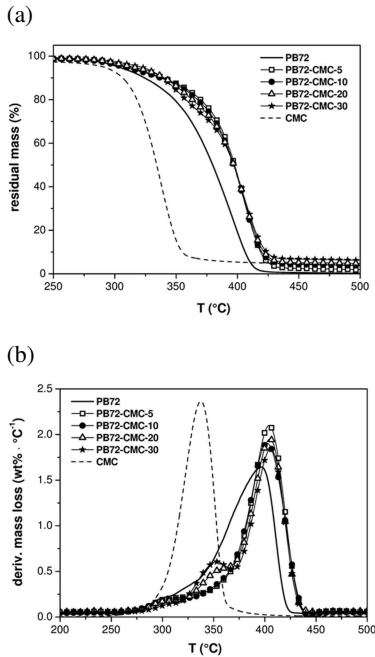
Figure IV- 12. TGA thermograms of neat PB72, neat CMC and resulting composites. (a)Residual mass as a function of temperature, (b) derivative of the mass loss.

(a)

(b)
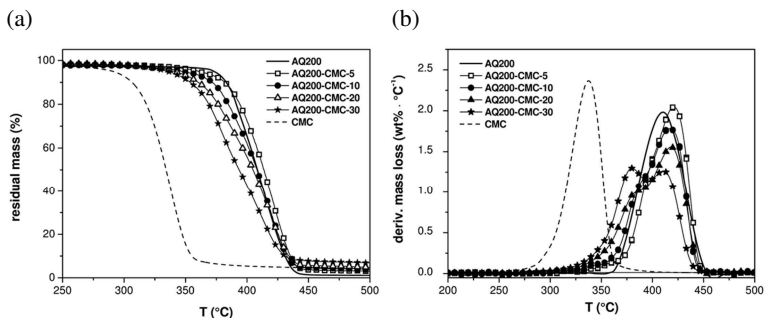
Figure IV- 13. TGA thermograms of neat AQ200, neat CMC and resulting composites. (a)Residual mass as a function of temperature, (b) derivative of the mass loss.

(a)

(b)
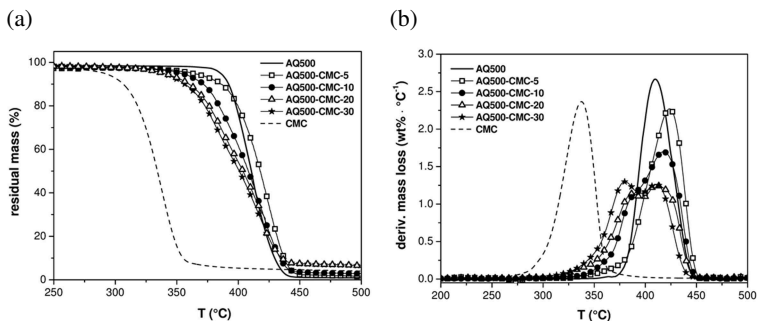
Figure IV- 14. TGA thermograms of neat AQ500, neat CMC and resulting composites. (a)Residual mass as a function of temperature, (b) derivative of the mass loss.

Table IV- 2. Results of TGA tests on neat matrices, CMC and resulting composites

Sample	T_{onset} (°C)	T_{max} (°C)	Residual mass at 700 °C (%)
PB72	298	396	--
PB72-CMC-5	310	406	0.2
PB72-CMC-10	308	406	1.0
PB72-CMC-20	314	406	2.2
PB72-CMC-30	321	406	3.4
AQ200	370	414	--
AQ200-CMC-5	360	422	0.2
AQ200-CMC-10	346	420	1.1
AQ200-CMC-20	341	420	2.6
AQ200-CMC-30	335	380	3.8
AQ500	380	411	--
AQ500-CMC-5	362	425	0.2
AQ500-CMC-10	353	418	1.0
AQ500-CMC-20	338	399	2.5
AQ500-CMC-30	339	380	3.7
CMC	291	337	0.8

Unfilled and filled composites with the lowest amount of CMC show a similar decomposition pattern with a one-step degradation peak due to the polymer matrix oxidative degradation. The increase of CMC loading over 10 wt% leads to the presence of another peak centered at lower temperatures closer to the CMC degradation temperature. Although this earlier degradation peak has been detected in other studies on CMC polymer composites [112], it is difficult to assess its nature. It could be attributed to a fraction of CMC particles that starts to degrade immediately after the typical decomposition stage of pure CMC because of the presence of the matrix or if it is due to an earlier degradation of a fraction of the matrix promoted by the high amount of the microfiller. The temperature associated to the beginning of the thermal degradation (T_{onset}), corresponding to a mass loss of 5 wt%,

for PB72 samples increases proportional to the filler loading. In case of Aquazol formulations the opposite phenomenon occurs, with the decrease of T_{onset} with increasing of CMC content. All composite samples exhibit an interesting improvement of the temperature associated to the maximum mass loss rate (T_{max}) since the lowest amount of microfiller, confirming the capability of this microfiller to increase the thermal stability of polymeric matrix [5, 113]. For Paraloid formulations there is no variation as the CMC content increases. For Aquazol polymers and especially for AQ500 the highest amounts of CMC promote the shift of the T_{max} peak towards lower temperatures closer to the T_{max} value of microcellulose. This different behavior is summarized in Figure IV-15(a-b) reporting the relative T_{onset} and T_{max} trends of the three matrices as a function of the CMC loading, calculated dividing temperature values of each composite by those of their corresponding neat matrix.

(a)   (b)
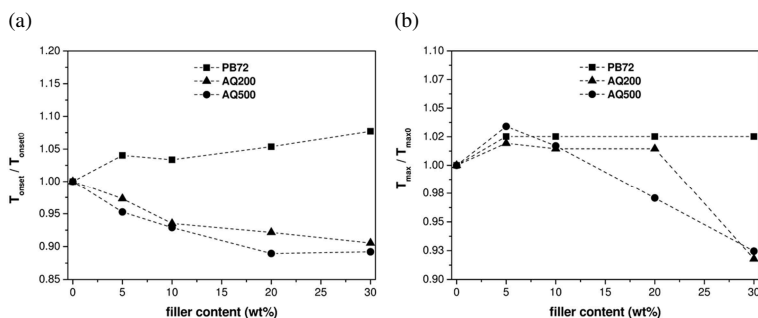
Figure IV- 15. Relative TGA properties trends of Paraloid, Aquazol 200 and 500 based composites (a) Temperature associated to the beginning of the degradation (T_{onset}), (b) temperature associated to the maximum mass loss rate (T_{max}).

A different polymer–filler interfacial adhesion degree between PB72 and AQ200/500 could be the main cause of this different behavior. According to

a widely accepted explanation [114, 115], the introduction of a filler in polymeric materials can promote the formation of a char enriched surface layer acting as a barrier to the diffusion of oxidant species through the samples and thus inhibiting the degradation process. This effect leading to an increase of the thermal stability of the matrix is particularly evident in nanofilled composites, but it could be also found in some microcomposites. The formation of this ceramized surface layer on samples is confirmed by the fact that the residual mass at 700 °C increases proportionally to the filler content for all composites because this surface layer does not allow the complete combustion and vaporization of matrices (Table IV-2). But, in case of Aquazol samples the lower polymer-filler interaction limits the positive effect of this ceramized surface on the thermal stability.

4.1.2   Physical characterization

4.1.2.1   *Water sorption tests*

The water uptake tests allowed the determination of the moisture sorption kinetics (M%) of unfilled and filled matrices (Figure IV-16(a-c)). Composites with the lowest and the highest amounts of CMC were tested. The maximum moisture content (M_{MAX}) and the time required to reach equilibrium conditions (t_s) are summarized in Table IV-3. Gravimetric curves of all formulations (Figure IV-16(a-c)) show a typical Fickian behavior, with an initial step reporting a linear relationship between the humidity sorption and the square root of the time, typical of a Fickian diffusion. After this step, the water sorption rate decreases until an equilibrium point. Similar behavior is widely documented in the scientific literature on the hydro-thermal aging of polymer composites [116-118].

(a)

(b)

(c)
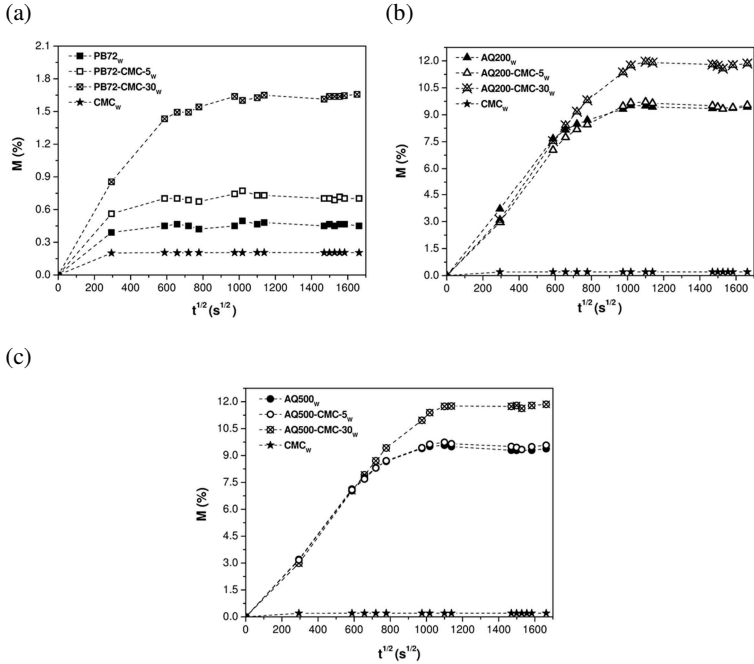
Figure IV- 16. Water kinetics of CMC powder, neat matrices and resulting composites conditioned at RH = 55% and T = 23°C. (a) PB72 based composites, (b) AQ200 based composites, (c) AQ500 based composites.

Table IV- 3. Results of water absorption kinetics of neat matrices and resulting composites in conditioned state.

Sample	M_{MAX} (wt%)	t_s (s)
PB72	0.45	24
PB72-CMC-5	0.70	96
PB72-CMC-30	1.63	240
AQ200	9.37	264
AQ200-CMC-5	9.51	264
AQ200-CMC-30	11.91	336
AQ500	9.35	264
AQ500-CMC-5	9.56	264
AQ500-CMC-30	11.77	336
CMC	0.20	24

It is worthwhile to note the different sorption behavior of Paraloid and Aquazol polymers. The two polyamides show a much higher tendency to water uptake with respect to the acrylic resin, underlining the substantial hygroscopic nature of these products.

Analyzing composites results, although CMC powder sorbs less water than neat resins, the introduction of this filler leads to an increase of the moisture content in all filled samples, more evident as its content increases. For instance, if M% of AQ500 is 9.35 wt%, AQ500-CMC-30 samples present an equilibrium moisture value of 11.77 wt%. Moreover, the time needed to reach the equilibrium level (ts) increases with the filler amount, passing, for example, from 4 days for PB72 and PB72-CMC-5 samples up to 10 days for PB72-CMC-30 ones and from 11 days for AQ200 and AQ500 samples up to 14 days for AQ200-CMC-30 and AQ200-CMC-30 composites. Moisture

absorption in polymeric materials is generally ruled by the Fick's diffusion law. It is known that water molecules may rapidly diffuse within the matrix, while moisture diffusion through filler particles is considerably slower. Another important diffusion mechanism in composite materials is the capillarity and the flow of water through microcraks, voids and other defects, including the filler-matrix interface [119-121]. Therefore, the higher tendency of CMC filled composites to absorb water in comparison to neat polymer matrices could be explained considering this capillary water diffusion.

4.1.2.2 *Optical transparency assessment*

Good optical properties and, particularly, high transparency levels are among the most important features of a polymer to be applied in the cultural heritage restoration. The addition of a filler in a polymeric matrix can impair its optical features because of the size of the reinforcing agent, the tendency of the filler to aggregate and/or the filler content [122, 123]. In Figure IV-17 optical pictures of thin films of each neat matrix and its relative composites with 5 wt% and 30 wt% of CMC are shown. It is evident how formulations with the highest CMC amount exhibit a chromatic variation, ranging from colorless materials to light yellow/brown ones.

Figure IV- 17. Optical images of thin adhesive composite films showing the effect of the addition of 5 wt% and 30 wt% of CMC on the optical properties of Paraloid and Aquazol matrices.

4.1.2.3   CIELAB color measurements

The chromatic variation optically detected was quantified by CIELAB color measurements and the main color parameters are listed in Table IV-4. In the CIELAB 1976 system, the Cartesian coordinates, L*, a* and b*, describe a 3-dimensional space useful to identify colors. L*, a* and b* values correspond to CIE XYZ tristimulus values X, Y, Z, by following equations:

$$L^* = 116 \left(\frac{Y}{Y_n} \right)^{1/3} - 16 \qquad (9)$$

$$a^* = 500 \left[\left(\frac{X}{X_n} \right)^{1/3} - \left(\frac{Y}{Y_n} \right)^{1/3} \right] \qquad (10)$$

$$b^* = 200 \left[\left(\frac{Y}{Y_n} \right)^{1/3} - \left(\frac{Z}{Z_n} \right)^{1/3} \right] \qquad (11)$$

where X_n, Y_n and Z_n are the tristimulus values of the white stimulus, which is typically the brightest stimulus in the view field [124].

Table IV- 4. Measured CIELAB Color coordinate values.

Sample	L*	a*	b*	dE*·ab
PB72	93.76 ± 0.07	2.70 ± 0.05	-10.51 ± 0.24	0
PB72-CMC-5	93.57 ± 0.71	2.65 ± 0.05	-10.06 ± 0.23	0.56 ± 0.07
PB72-CMC-30	92.57 ± 0.42	2.09 ± 0.04	-6.24 ± 0.27	4.36 ± 0.24
AQ200	93.47 ± 0.29	2.41 ± 0.08	-9.22 ± 0.25	0
AQ200-CMC-5	93.09 ± 0.79	2.13 ± 0.06	-8.22 ± 0.25	1.06 ± 0.17
AQ200-CMC-30	91.97 ± 0.47	1.74 ± 0.04	-4.44 ± 0.11	5.28 ± 0.48
AQ500	93.68 ± 0.44	2.53 ± 0.06	-9.89 ± 0.02	0
AQ500-CMC-5	93.06 ± 0.56	2.43 ± 0.09	-8.76 ± 0.24	1.16 ± 0.29
AQ500-CMC-30	92.17 ± 0.65	2.27 ± 0.11	-6.48 ± 0.16	3.50 ± 0.04

All tested films have similar lightness value (L*), except, composites with the highest amount of CMC that report a slight decrese of this property. All samples register a decrease of redness–greenness value (a*), and an enhancement of yellowness-blueness value (b*) as CMC loading increases. These variations are related to a chromatic shift of each neat matrix towards yellow tones with a slight decrease of brightness, especially for those formulations with 30 wt% of CMC as already seen in Figure IV-17. In order to quantify the color difference among examined samples, the Euclidean distances between the dE*·ab values of neat polymers (L_s, a_s, b_s) and the color values of CMC loaded matrices (L_2, a_2, b_2) were determined according to Eqn 12. [125]:

$$dE^* \cdot ab = [(L_2^* - L_s^*)^2 + (a_2^* - a_s^*)^2 + (b_2^* - b_s^*)^2]^{1/2} \qquad (12)$$

The just noticeable difference (JND) is the minimum dE*·ab value that can be perceived by the human eye. The accepted dE*·ab value for a barely perceivable difference is 2.3 and is given a unit of 1 JND. Color differences below 1 JND, or 2.3 dE*ab, are not easily detected by an observer [126]. Considering the dE*·ab values collected in Table IV-4, only formulations with the highest amount of CMC show a noticeable color difference and among these samples AQ200 presents the highest chromatic variation, while AQ500 has the lowest one.

4.1.2.4 UV-vis spectroscopy analysis

Relative transmittance, T%, as a function of the wavelength is reported in in Figure IV-18(a-c) for filled and unfilled polymers films.

(a)

(b)
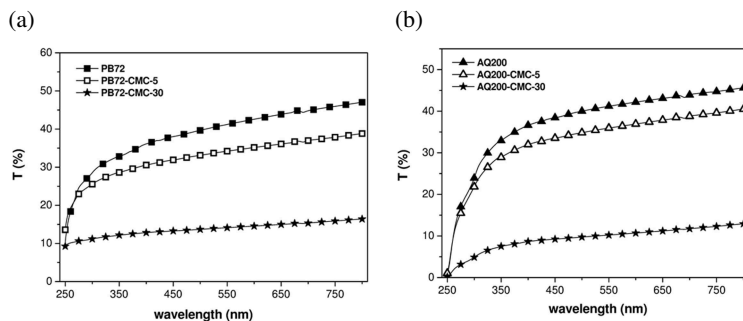
(c)
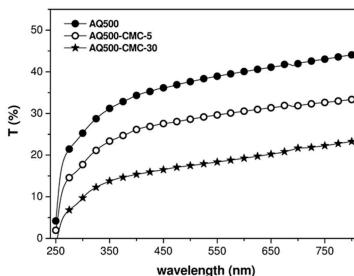
Figure IV- 18. Relative transparency (T) spectra of neat matrices and resulting composites. (a) Paraloid B72, (b-c) Aquazol 200 and 500.

The introduction of CMC leads to a drop in transmittance values with increasing filler content for all three polymers. In particular, PB72 and AQ200 lose about 15% and 70% of the transmittance after the addition of 5 wt% and 30 wt% of CMC, respectively. AQ500 registers a higher T% loss at 5 wt% of CMC of about 25% and the lowest decrease of transparency at 30 wt% of filler loading of about 45%.

4.1.3   Mechanical characterization

The mechanical characterization results discussed in the following sections were obtained on microcomposites in dry and conditioned state (T= 23°C, RH= 55%).

4.1.3.1   *Dynamic mechanical thermal analysis (DMTA)*

The storage modulus (E'), loss modulus (E'') and tanδ curves of the three neat matrices and corresponding CMC composites in the dry state, obtained from DMTA analysis, are reported in Figure IV-19(a-c), IV-20(a-c) and IV-

21(a-c). In Table IV-5 the most relevant data emerging from DMTA analysis are shown.

(a)

(b)

(c)
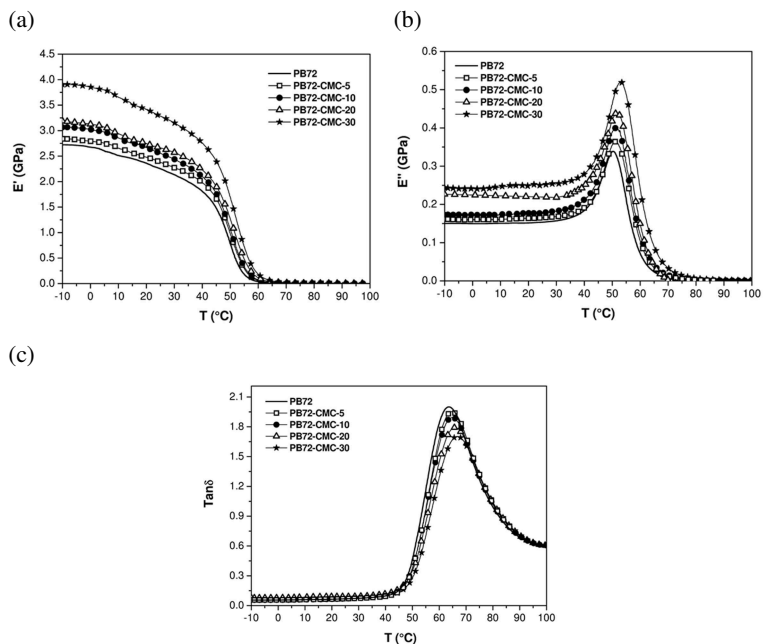
Figure IV- 19. DMTA thermograms of neat PB72 and resulting composites in the dry state (f = 1 Hz). (a) Storage modulus E', (b) loss modulus E", (c) loss factor tanδ.

(a)

(b)

(c)
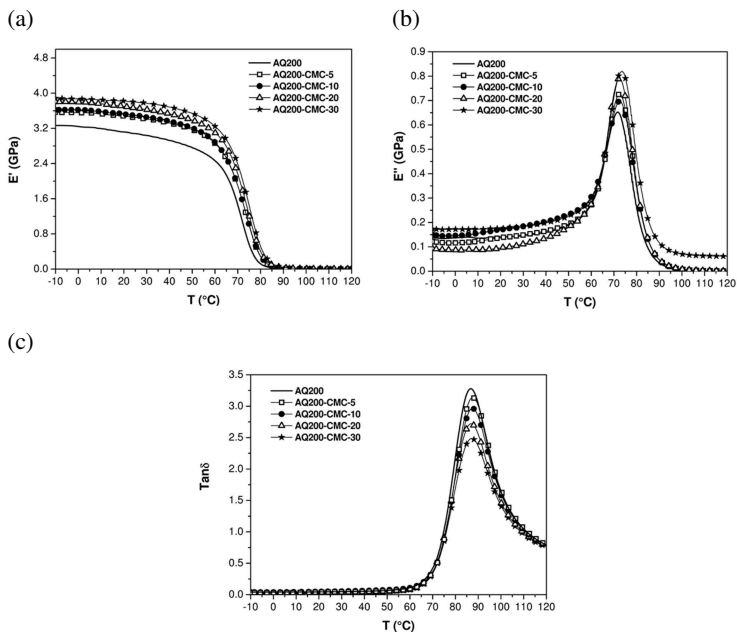
Figure IV- 20. DMTA thermograms of neat AQ200 and resulting composites in the dry state (f = 1 Hz). (a) Storage modulus E', (b) loss modulus E'', (c) loss factor tanδ.

(a)

(b)
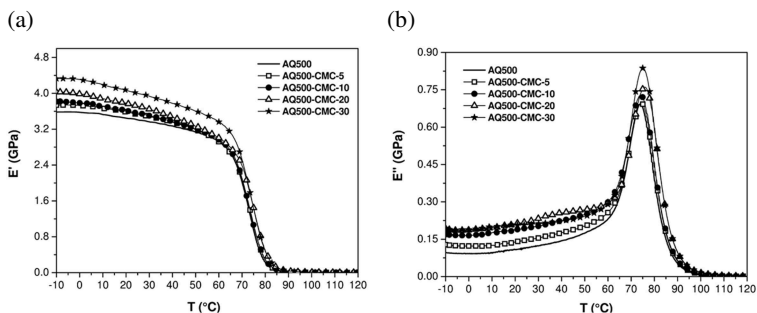
(c)
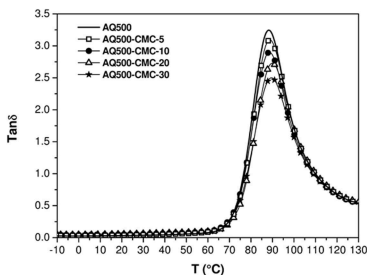
Figure IV- 21. DMTA thermograms of neat AQ500 and resulting composites in the dry state (f = 1 Hz). (a) Storage modulus E', (b) loss modulus E'', (c) loss factor tanδ.

Table IV- 5. Results of DMTA tests on neat matrices and resulting composites in the dry state.

Sample	E' at 25°C (GPa)	E'' peak value (GPa)	tanδ peak value	T_g from E'' (°C)
PB72	2.25	0.34	2.00	50.5
PB72-CMC-5	2.40	0.36	1.99	51.3
PB72-CMC-10	2.55	0.40	1.93	51.4
PB72-CMC-20	2.65	0.46	1.81	51.8
PB72-CMC-30	3.27	0.52	1.73	52.9
AQ200	3.08	0.62	3.25	71.6
AQ200-CMC-5	3.45	0.67	3.18	72.5
AQ200-CMC-10	3.51	0.68	2.99	72.6
AQ200-CMC-20	3.66	0.73	2.75	72.4
AQ200-CMC-30	3.80	0.80	2.52	73.5
AQ500	3.41	0.69	3.23	73.9
AQ500-CMC-5	3.53	0.70	3.17	74.4
AQ500-CMC-10	3.58	0.73	2.97	74.2
AQ500-CMC-20	3.71	0.76	2.79	75.5
AQ500-CMC-30	4.00	0.84	2.54	75.0

All dried microcomposites report a similar viscoelastic response after the introduction of CMC flakes with a progressive enhancement of both the storage (E') and the loss (E'') moduli as the filler loading increases. Correspondingly, tanδ values decrease with the CMC amount. Considering that the loss factor is calculated as the ratio between E'' and E', the detected tanδ trends can be explained by the fact that the positive contribution of the CMC addition on the E' is higher than the E'' enhancement. Therefore, CMC has a more relevant action on the elastic components than the viscoelastic behavior of neat matrices. Formulations of Paraloid with 30 wt% of CMC reach values of E' higher than about 45% in comparison to the neat matrix, Aquazol 200 and 500 filled composites with the highest amount of CMC register an increase of E' of about 25% and 20% respectively in comparison to their corresponding matrix. This stabilizing effect due to the CMC introduction has been already reported in other literature studies [5, 112, 127]. According to DMTA tests, the temperatures associated to E'' peaks (representing the glass transition temperatures of composites) slightly shift towards higher values with an enhancement of about 3 degrees for PB72-CMC-30 and about 2 degrees for AQ200-CMC-30 and AQ500-CMC-30. In addition the coefficient of linear thermal expansion (CLTE) was calculated, as the slope of the secant line of thermal strain curves in the glassy (CLTEg) and rubbery (CLTEr) states for each set of composites, according to Equation (13):

$$CLTE = \frac{\Delta L}{L_0 \cdot \Delta T} \qquad (13)$$

where L_0 is the original length of the samples (i.e the length of the samples at interval temperatures), ΔL is the thermal displacement in the considered

temperature interval (ΔT). CLTE values below and above T_g of all composites are listed in Table IV-6, while in Figure IV-22(a-b), IV-23(a-b), IV-24(a-b) thermal strain curves of PB72, AQ200 and AQ500 composites, used for the determination of CLTE values, are shown.

(a)   (b)
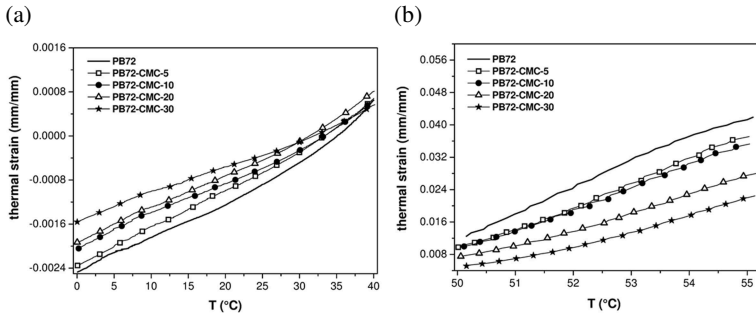
Figure IV- 22. Thermal strain curves of PB72/CMC composites in the dry state. (a) Below T_g, between 0 °C and 40 °C, (b) above T_g, between 50 °C and 55 °C.

(a)   (b)
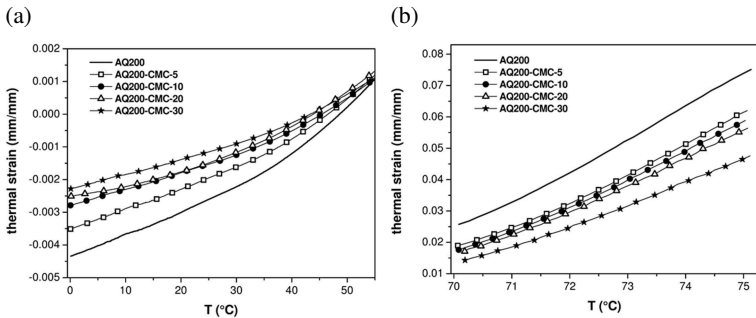
Figure IV- 23. Thermal strain curves of AQ200/CMC composites in the dry state. (a) Below T_g, between 0 °C and 55 °C, (b) above T_g, between 70 °C and 75 °C.

(a) (b)
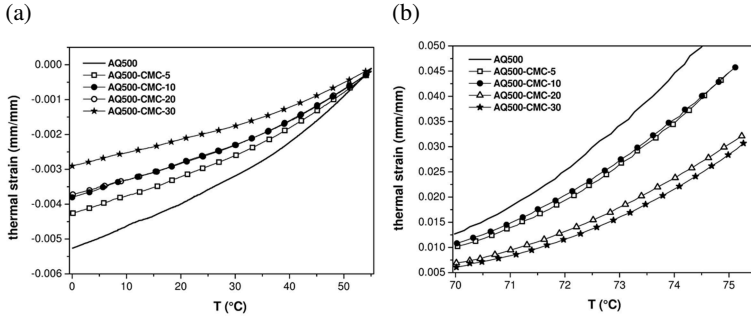
Figure IV- 24. Thermal strain curves of AQ500/CMC composites in the dry state. (a) Below T$_g$, between 0 °C and 55 °C, (b) above T$_g$, between 70 °C and 75 °C.

The addition of CMC flakes induces a general reduction of the coefficient of linear thermal expansion (CLTE) both under and above the glass transition temperature in all resins. CLTE$_g$ and CLTE$_r$ values of neat matrices decreases of about 30% for PB72 and AQ200 based composites and about 40% for AQ500 samples (Table IV-6). This improvement highlights the stabilizing effect of CMC on these polymers.

Table IV- 6. Coefficient of linear thermal expansion values calculated in the glassy (CLTE$_g$) and in the rubbery (CLTE$_r$) states under dry conditions.

Sample	CLTE$_g$ (K^{-1})	CLTE$_r$ (K^{-1})
PB72	6.3E-05	6.2E-03
PB72-CMC-5	6.7E-05	5.7E-03
PB72-CMC-10	5.7E-05	5.4E-03
PB72-CMC-20	5.8E-05	4.2E-03
PB72-CMC-30	4.8E-05	3.6E-03
AQ200	9.3E-05	10.1E-03
AQ200-CMC-5	8.0E-05	8.8E-03
AQ200-CMC-10	6.6E-05	8.4E-03
AQ200-CMC-20	6.7E-05	8.1E-03
AQ200-CMC-30	5.8E-05	6.9E-03
AQ500	8.9E-05	8.4E-03
AQ500-CMC-5	7.1E-05	7.0E-03
AQ500-CMC-10	6.2E-05	6.9E-03
AQ500-CMC-20	6.2E-05	5.0E-03
AQ500-CMC-30	4.8E-05	4.8E-03

DMTA analysis were carried out on PB72, AQ200 and AQ500 microcomposites after a hydrothermal conditioning at T= 23°C and RH= 55%, simulating the standard environmental conditions recommended for the artwork conservation. Formulations with the lowest and the highest amount of CMC were selected for these tests. In Figure IV-25(a-c), IV-26(a-c) and IV-27(a-c) the storage modulus (E'), loss modulus (E'') and tanδ

curves of conditioned microcomposites are presented. In Table IV-7 DMTA results of each group of CMC composites are listed.

(a)

(b)

(c)
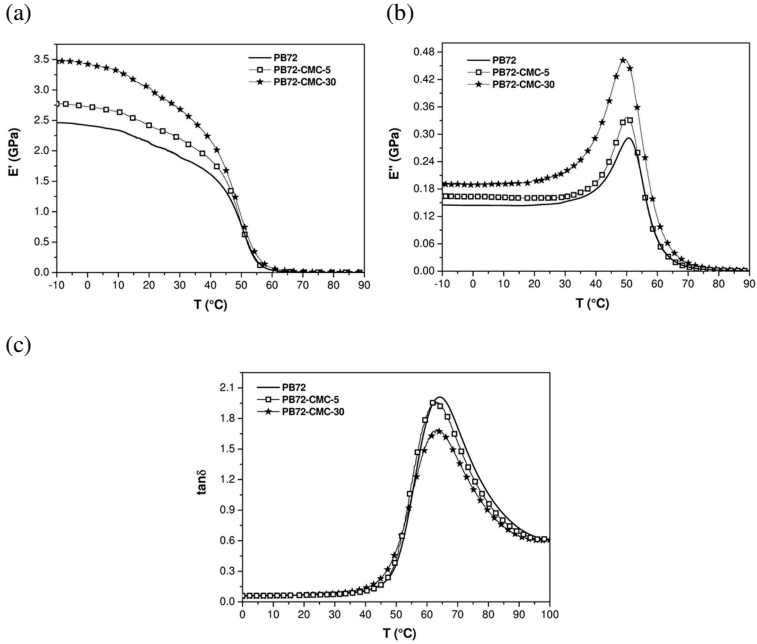
Figure IV- 25. DMTA thermograms of neat PB72 and resulting composites in conditioned state (f = 1 Hz). (a) Storage modulus E', (b) loss modulus E'', (c) loss factor tanδ.

(a)

(b)
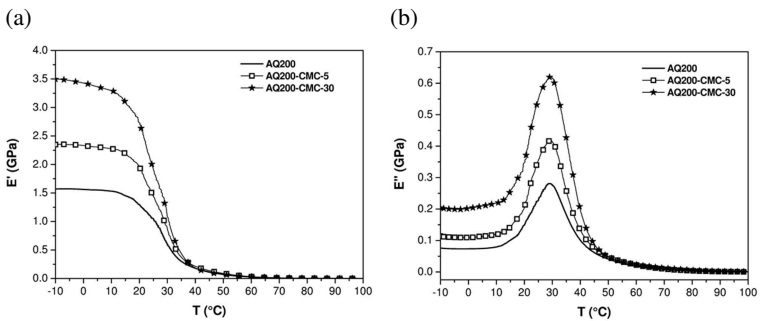
(c)
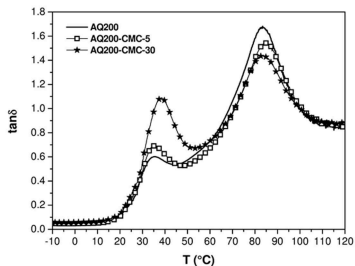
Figure IV- 26. DMTA thermograms of neat AQ200 and resulting composites in conditioned state (f = 1 Hz). (a) Storage modulus E', (b) loss modulus E", (c) loss factor tanδ.

(a)
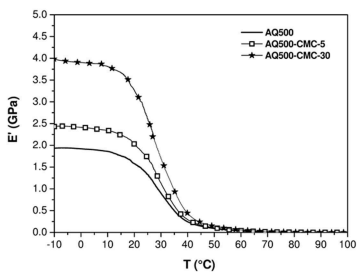
(b)
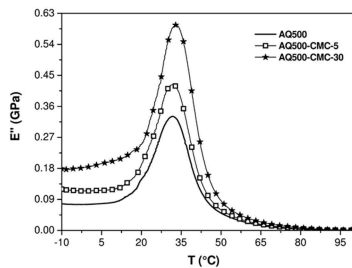
(c)
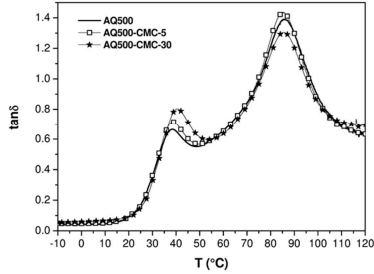
Figure IV- 27. DMTA thermograms of neat AQ500 and resulting composites in conditioned state (f = 1 Hz). (a) Storage modulus E', (b) loss modulus E", (c) loss factor tanδ.

Table IV- 7. Results of DMTA tests on neat matrices and resulting composites in the conditioned state.

Sample	E' at 25°C (GPa)	E" peak value (GPa)	tanδ peak value	T_g from E" (°C)
PB72	2.04	0.29	2.01	50.5
PB72-CMC-5	2.32	0.34	1.95	50.1
PB72-CMC-30	2.85	0.46	1.70	49.3
AQ200	1.56	0.28	0.60	28.9
AQ200-CMC-5	2.33	0.42	0.69	29.1
AQ200-CMC-30	3.43	0.62	1.09	29.9
AQ500	1.92	0.33	0.67	31.6
AQ500-CMC-5	2.70	0.48	0.72	31.6
AQ500-CMC-30	3.90	0.64	0.80	32.9

Interestingly, although the presence of water, it is possible to notice that even for conditioned composites the introduction of CMC is still able to promote the stabilization of each matrix with a proportional enhancement of both the storage and loss moduli as CMC loading increases. The viscoelastic behavior of wet Paraloid based composites is practically similar to that of corresponding dried samples. The tanδ of PB72/CMC dry and wet samples decreases with increasing of filler content. For Aquazol 200 and 500 in Figure IV-26c and IV-27c two peaks of tanδ are visible. The first peak centered at about 30 °C is related to wet samples while the second one centered at about 90 °C corresponds to dried polymers. In fact, being at a temperature close to that of the water evaporation, the two Aquazol composites lose their moisture content. Considering the first one, the loss factor of Aquazol wet formulations increases proportionally to the CMC amount, underling the dependency of tanδ on the humidity content of samples. In particular, AQ200/CMC wet composites show the highest increase of tanδ in comparison to AQ500/CMC ones. The glass transition temperature of wet PB72 composites at elevated filler amounts, evaluated in correspondence to the E" peak, shows a slight decrease due to the presence of moisture. A slight increase of T_g is observed for Aquazol samples. As reported in Table IV-8 the linear thermal expansion coefficient of the three matrices decreases proportionally to the CMC content in the glassy and in the rubbery state, regardless of the presence of moisture in materials. It is interesting to observe how the plasticizing effect promoted by the sorbed water is largely overcompensated by the stiffening action due to the microfiller addition.

Table IV- 8. Coefficient of linear thermal expansion values calculated in the glassy (CLTE$_g$) and in the rubbery (CLTE$_r$) states under wet conditions.

Sample	CLTE$_g$ (K^{-1})	CLTE$_r$ (K^{-1})
PB72	8.0E-05	4.9E-03
PB72-CMC-5	7.3E-05	5.1E-03
PB72-CMC-30	5.8E-05	3.4E-03
AQ200	10.2E-05	3.8E-04
AQ200-CMC-5	9.4E-05	3.7E-04
AQ200-CMC-30	7.7E-05	3.4E-04
AQ500	10.1E-05	4.5E-04
AQ500-CMC-5	9.2E-05	4.3E-04
AQ500-CMC-30	6.5E-05	4.1E-04

In order to better appreciate the viscoelastic response of CMC composites under different environmental conditions, the comparison between dried and conditioned samples of Paraloid and the two Aquazol is described in Figure IV-28(a-f) and IV-29(a-f), showing the relative DMTA properties trends (i.e. normalized over the value corresponding to neat polymer matrices) as a function of the CMC loading.

(a)   (b)

(c)

(d)

(e)

(f)
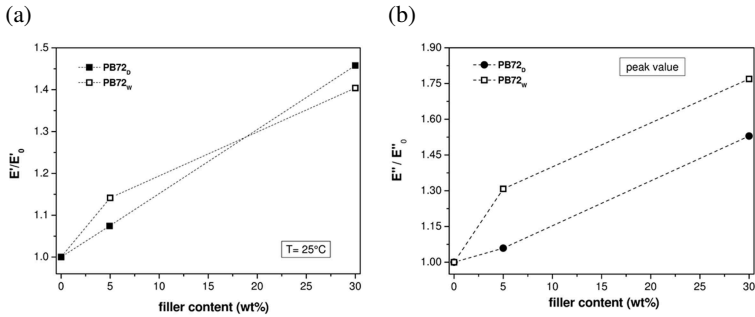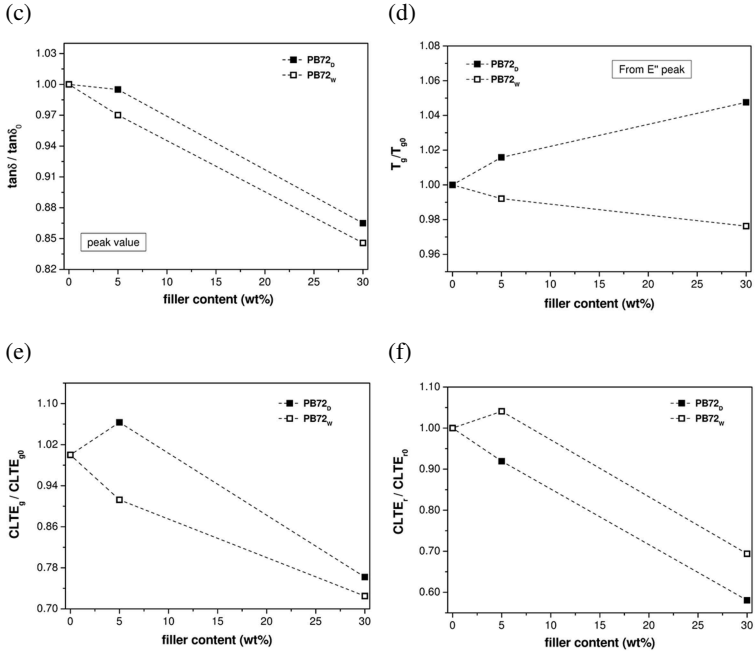
Figure IV- 28. Relative DMTA properties. Comparison between dried and conditioned PB72 composites:(a) Storage modulus, (b) loss modulus, (c) loss factor (d) glass transition temperature and (e-f) coefficient of linear thermal expansion below and above T_g.

(a)

(b)

(c)

(d)

(e)

(f)
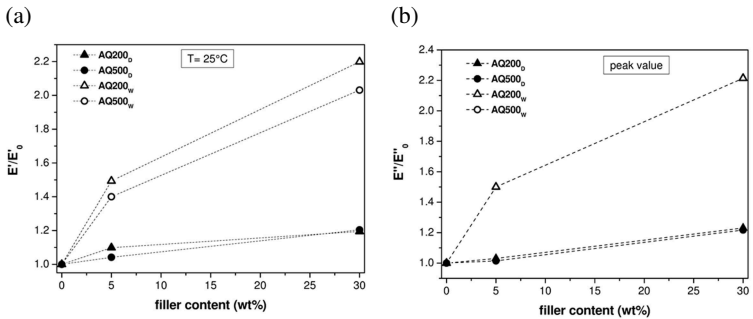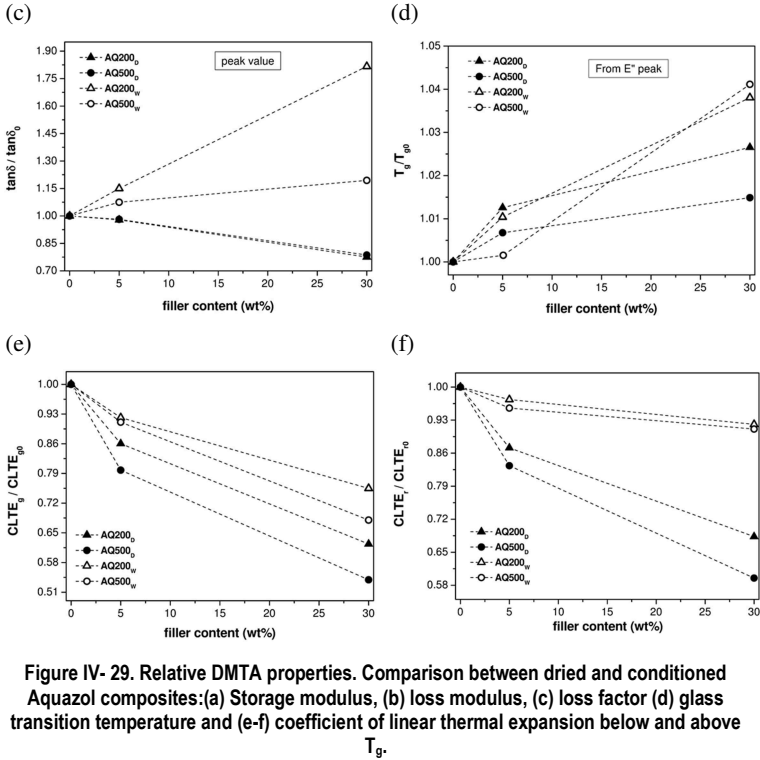
Figure IV- 29. Relative DMTA properties. Comparison between dried and conditioned Aquazol composites:(a) Storage modulus, (b) loss modulus, (c) loss factor (d) glass transition temperature and (e-f) coefficient of linear thermal expansion below and above T_g.

Paraloid B72 filled samples are not significantly affected by the presence of moisture. In fact dried and wet Paraloid show a similar viscoelastic behavior after the CMC introduction, except for the Tg trend that under conditioning slightly decreases with increasing of the CMC content. While dried PB72 composites report an increase of this property.   Remarkable, the increase of the elastic and the viscous part of the viscoelastic response (storage and loss moduli) of wet Aquazol formulations is more pronounced than that registered by dried samples. The loss tangent of AQ200/500 conditioned

samples shows an opposite trend in comparison to dried formulations, with tanδ that increases proportionally to the filler content instead to decrease as seen for dried compositions. There is no relevant effect due to the synergistic presence of water and CMC on the glass transition temperatures of neat polyamides. As reported in Figure IV-29(e-f), the linear thermal expansion coefficient of all matrices decreases proportionally to the CMC content in the glassy and in the rubbery state. Moreover, dried composites report a more significant reduction of this property. It is possible to conclude that the stabilizing effect provided by CMC does not markedly depend on the moisture content. Actually in the case of Aquazol the water molecules probably improve the low polymer-filler interfacial adhesion, filling the interface voids between matrix and CMC flakes and thus allow a better reinforcing action of microcellulose.

4.1.3.2   *Quasi-statc tensile tests*

Representative stress/strain (σ/ε) curves obtained from quasi-static tensile tests of unfilled and filled Paraloid and Aquazol composites in the dry state are reported in Figure IV-30(a-c), while in Table IV-9 the most important parameters obtainable from these curves are summarized (i.e. elastic modulus E, stress at break σ_B, strain at break ε_B and tensile energy at break TEB).

(a)

(b)

(c)
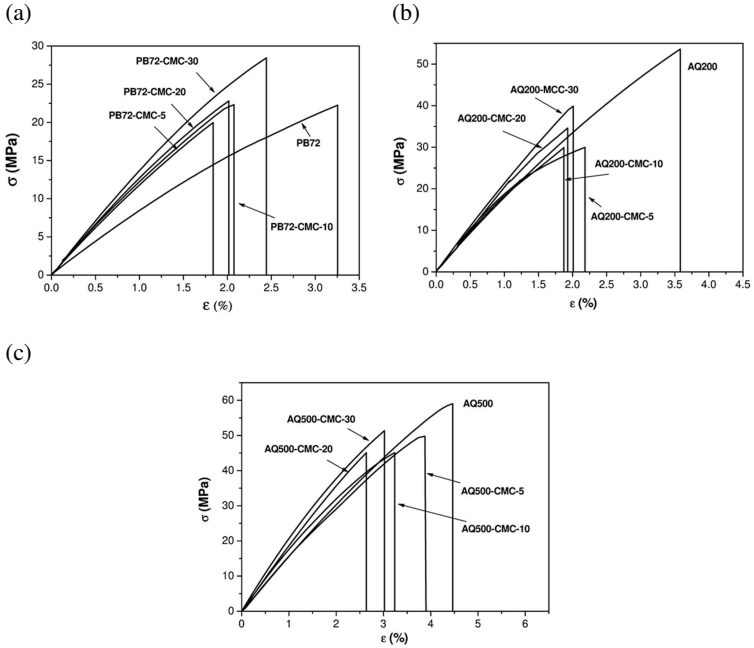
Figure IV- 30. Representative stress-strain curves of neat matrices and corresponding composites in the dry state. (a) Paraloid B72, (b) Aquazol 200 and (c) Aquazol 500.

Table IV- 9. Tensile properties of neat matrices and resulting composites in the dry state.

Sample	E (GPa)	σ_B (MPa)	ε_B (%)	TEB (MJ·m^{-3})
PB72	1.54 ± 0.08	23.01 ± 1.51	3.46 ± 0.19	0.44 ± 0.08
PB72-CMC-5	1.49 ± 0.22	21.22 ± 2.37	2.28 ± 0.43	0.34 ± 0.11
PB72-CMC-10	1.75 ± 0.21	23.14 ± 2.09	2.98 ± 0.31	0.48 ± 0.06
PB72-CMC-20	2.57 ± 0.30	23.80 ± 2.27	2.14 ± 0.28	0.28 ± 0.07
PB72-CMC-30	3.32 ± 0.40	26.02 ± 2.44	2.09 ± 0.33	0.35 ± 0.09
AQ200	3.05 ± 0.15	52.26 ± 5.34	3.26 ± 0.27	1.13 ± 0.38
AQ200-CMC-5	3.23 ± 0.33	29.07 ± 3.11	2.21 ± 0.22	0.43 ± 0.04
AQ200-CMC-10	3.61 ± 0.26	29.23 ± 1.21	1.84 ± 0.06	0.32 ± 0.06
AQ200-CMC-20	3.99 ± 0.44	34.77 ± 1.33	1.93 ± 0.06	0.35 ± 0.03
AQ200-CMC-30	4.22 ± 0.30	40.16 ± 1.56	2.07 ± 0.09	0.43 ± 0.04
AQ500	3.33 ± 0.44	59.80 ± 1.45	4.55 ± 0.11	1.44 ± 0.15
AQ500-CMC-5	3.47 ± 0.10	47.88 ± 2.99	3.84 ± 0.32	0.99 ± 0.18
AQ500-CMC-10	3.96 ± 0.24	45.23 ± 0.92	3.29 ± 0.46	0.86 ± 0.19
AQ500-CMC-20	4.1 ± 0.18	42.95 ± 2.94	2.51 ± 0.26	0.52 ± 0.09
AQ500-CMC-30	4.50 ± 0.63	52.05 ± 2.57	2.77 ± 0.28	0.84 ± 0.02

All formulations under dry conditions exhibit a fracture behavior typical of brittle materials with a limited plastic deformation fraction before failure.

The reinforcing action of CMC is clearly visible in the systematic increase of the elastic modulus (E) with increasing of the filler loading reported by all microcomposites. In order to better understand the elastic properties of examined samples, a modeling of the experimental elastic modulus data was attempted. Elastic modulus data were fitted by using an empirical model traditionally used for composites with short fibers randomly oriented in a plane [128]. According to Equation (11), the tensile modulus of 2D

randomly oriented fibers composites (E_C) can be related to the elastic moduli of ideal composites having the same volume fraction of fibers perfectly aligned (E_L) or transversally oriented (E_T) to the loading axis:

$$E_C = \frac{3}{8} E_L + \frac{5}{8} E_T \qquad (14)$$

The moduli (E_L, E_T) can be calculated by using Halpin-Tsai model [129] according to the following equations:

$$E_L = \frac{1 + 2(L/D)(\eta_L \phi)}{1 - \eta_L \phi} \ E_M \qquad (15)$$

$$E_T = \frac{1 + 2\eta_T \phi}{1 - \eta_T \phi} \ E_M \qquad (16)$$

and:

$$\eta_L = \frac{(E_F/E_M) - 1}{(E_F/E_M) + 2(L/D)} \qquad (17a)$$

$$\eta_T = \frac{(E_F/E_M) - 1}{(E_F/E_M) + 2} \qquad (17b)$$

where L/D is the aspect ratio of the fibers, Φ is the volume fraction of the fibers, and E_F and E_M are the fibers and matrix moduli, respectively. The comparison between the experimental values of elastic moduli of Paraloid, Aquazol 200 and 500 based composites under investigation and the values predicted according to eqn 14 is represented in Figure IV-31(a-c). Two theoretical predictions were considered, by using two different CMC elastic

modulus values. The first one (i.e. 9.2 GPa) was determined by Hancock et al. through micromechanical tests [130], while the second one (i.e. 25 GPa) was estimated by Eichorn et al. through Raman spectroscopy [131].

(a)   (b)

(c)
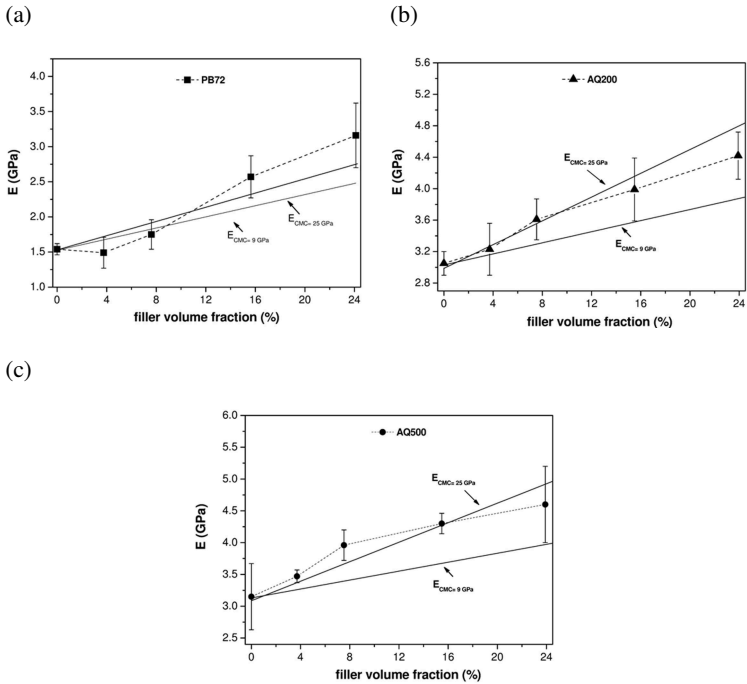
Figure IV- 31. Elastic modulus trends, with theoretical predictions according to Equation (14) (full lines). (a) Paraloid B72, (b) Aquazol 200 and (c) Aquazol 500.

Considering standard deviation values, between the two proposed models, that one calculated with an elastic modulus of CMC flakes equal to about 25 GPa is able to satisfactorily fit experimental data of all three matrices.

Other important evidences from tensile tests are presented in Table IV-9. For PB72 samples, the stress at break (σ_B) is not substantially affected by CMC flakes, while strain at break (ε_B) is slightly reduced. This ε_B reduction induces the light decrease of the specific tensile energy to break (TEB) values as the filler increases. For both Aquazol matrices, a significant embrittling effect due to the CMC introduction can be detected under dry state with a decrease of σ_B, ε_B and consequently of the specific tensile energy to break. This phenomenon is more evident at lowest amounts of CMC.

Tensile test were even conducted on conditioned samples of Paraloid and Aquazol composites (T= 23°C and RH= 55%). Formulations with 5 wt% and 30 wt% of CMC that showed the best mechanical results under dry conditions were examined. Figure IV-32(a-c) shows representative stress/strain curves of conditioned microcomposites samples.

(a)

(b)
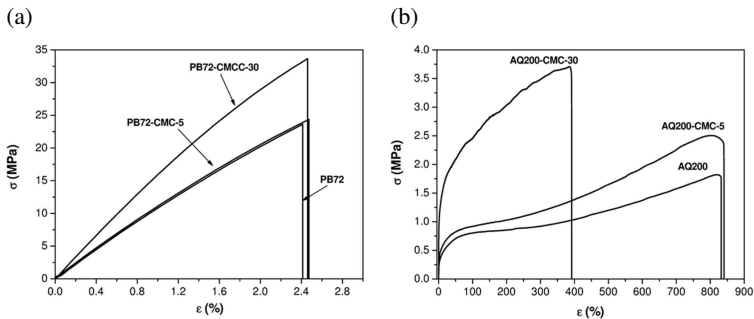
(c)
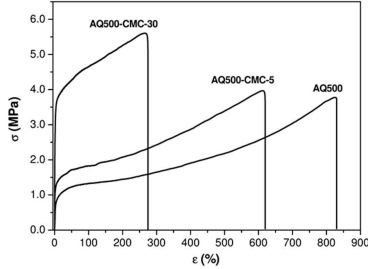
Figure IV- 32. Representative stress-strain curves of neat matrices and corresponding composites in the conditioned state. (a) Paraloid B72, (b) Aquazol 200 and (c) Aquazol 500.

If Paraloid, as already seen in DMTA analysis, does not show a relevant difference in its mechanical response in presence of moisture, Aquazol 200 and 500 modify their mechanical response from brittle to ductile after conditioning. As one can see in Figure IV-31 (b-c) the plastic deformation fraction is much higher than that observed for dried samples. In Table IV-10 the main tensile results obtained from Paraloid based microcomposites are reported.

Table IV- 10. Tensile properties of neat Paraloid and its resulting composites in the conditioned state.

Sample	E (GPa)	σ_B (MPa)	ε_B (%)	TEB (MJ·m^{-3})
PB72	1.65 ± 0.06	23.53 ± 0.39	2.49 ± 0.11	0.35 ± 0.02
PB72-CMC-5	1.71 ± 0.06	24.60 ± 0.38	2.78 ± 0.01	0.37 ± 0.02
PB72-CMC-30	3.13 ± 0.09	35.82 ± 1.88	2.50 ± 0.13	0.52 ± 0.07

For conditioned PB72 samples a noticeable increase of σ_B can be observed. Moreover, ε_B is not affected by CMC and an increase of TEB as the filler loading increases is detected. For instance, a TEB enhancement of 20% in comparison to the neat PB72 matrix was registered for PB72-CMC-30 samples. In Table IV-11 the ultimate tensile properties of wet Aquazol based microcomposites are summarized. Since AQ200 and AQ500 samples after conditioning show a rubber-like behavior, a secant elastic modulus at 10% strain was determined.

Table IV- 11. Tensile properties of neat Aquazol and resulting composites in the conditioned state.

Sample	$E_{10\%\varepsilon}$ (GPa)	σ_B (MPa)	ε_B (%)	TEB (MJ·m^{-3})
AQ200	4.56 ± 0.06	1.86 ± 0.13	861.22 ± 27.75	9.46 ± 0.21
AQ200-CMC-5	5.79 ± 0.14	2.44 ± 0.06	846.31 ± 25.54	12.75 ± 0.54
AQ200-CMC-30	14.59 ± 0.79	3.77 ± 0.18	426.04 ± 20.70	12.18 ± 0.38
AQ500	11.56 ± 0.20	3.90 ± 0.21	724.14 ± 29.48	17.80 ± 0.68
AQ500-CMC-5	14.31 ± 0.70	4.13 ± 0.09	646.00 ± 14.42	17.01 ± 0.18
AQ500-CMC-30	38.68 ± 1.44	5.90± 0.10	276.47 ± 8.57	13.65 ± 0.20

A progressive increment of the stiffness and the strength at break values of all Aquazol formulations can be detected with the increase of both E and σ_B as the filler loading increases. Although the systematic reduction of ε_B due to the increase of CMC amount, no negative effect on the toughness of these composites is observed for AQ200 filled samples, while AQ500-CMC-30 composites report a decrease of TEB of about 20% in comparison to their neat matrix. A direct comparison between the relative parameters (i.e. normalized over the value corresponding to neat polymer matrices) detected

from tensile test of dried and conditioned microcomposites is illustrated in Figure IV-33(a-d) for Paraloid and IV-34(a-d) for the two Aquazol.

(a)

(b)

(c)

(d)
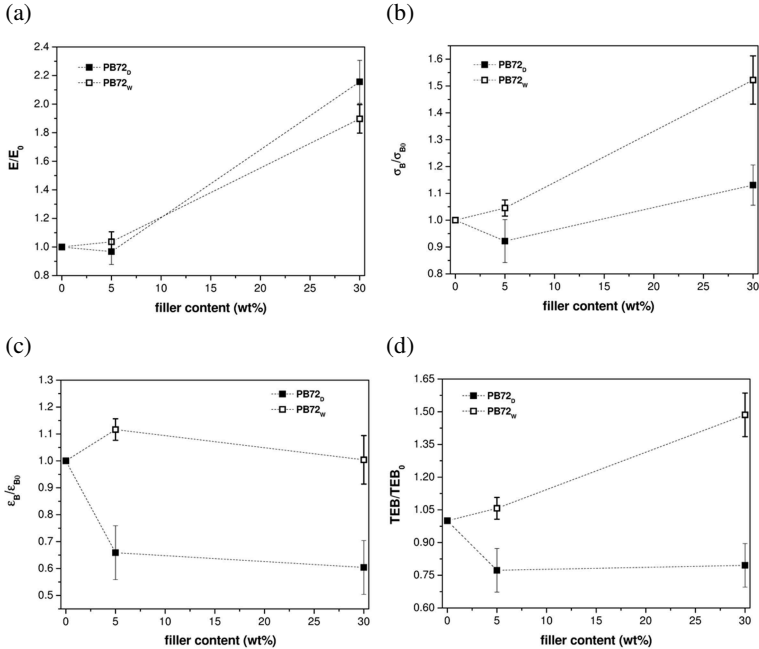
Figure IV- 33. Comparison between relative tensile properties of dried and wet Paraloid composites: (a) elastic modulus, (b) stress at break, (c) strain at break and (d) tensile energy to break.

Considering standard deviation values associated to these measurements, it is possible to affirm that elastic modulus trends of Paraloid formulations in dry and wet states are similar. While, in presence of moisture, CMC mainly acts as a reinforcement producing the enhancement of σ_B and a slight increase of ε_B and consequently the increase of TEB values.

(a)

(b)

(c)

(d)
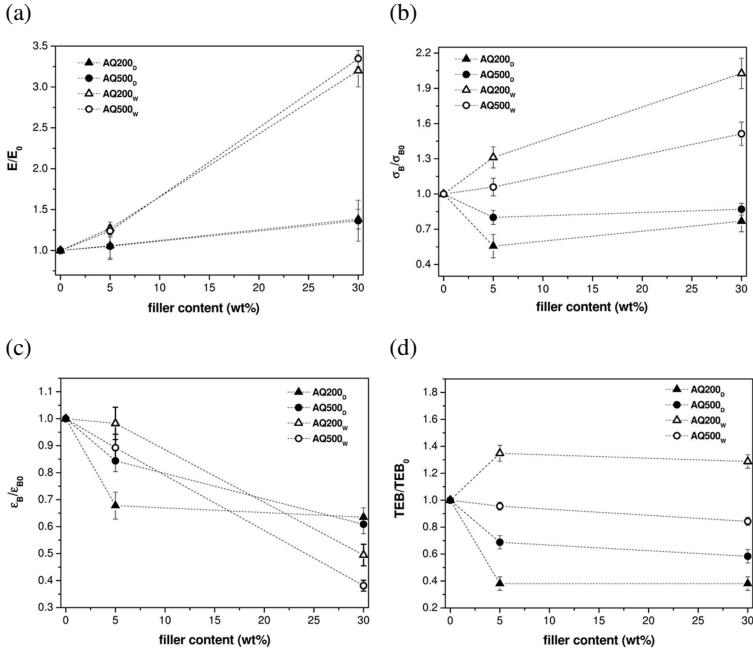
Figure IV- 34. Comparison between relative tensile properties of dried and wet Aquazol composites: (a) elastic modulus, (b) stress at break, (c) strain at break and (d) tensile energy to break.

For Aquazol, as clearly shown in Figure IV-34(a-d), the increase of the elastic modulus with the filler loading can be observed for all samples in both dry and conditioned state, but relative values of wet samples are much higher than dried ones. For the two polymeric matrices, dried samples exhibit an embrittling effect due to the CMC introduction with a decrease of tensile strength and ultimate strain and consequently of the tensile toughness (TEB). On the other hand, wet samples do not present this drawback. In fact, the increase of the σ_B proportional to the CMC content avoids the drop in TEB values. Conditioned AQ200 based composites present a remarkable

increase of TEB. For instance, AQ200-CMC-30$_w$ manifests an increment of σ_B and TEB values of about 100% and 35%, respectively, in comparison to the neat matrix. It is therefore confirmed the reinforcing and stabilizing effect of this natural microfiller on the investigated polymer matrices under a humidity level typical of artwork conservation.

On the basis of the collected results it can be concluded that the concurrent action of a natural reinforcing microfiller as CMC and a limited moisture content leads to a mechanical improvement of filled materials showing better mechanical performance than dried matrices. This demonstrates how CMC has a predominant role on the mechanical response of PB72 and AQ200-500 over the action of water absorbed by these materials under standard hydro-thermal service conditions.

4.1.3.3   *Plane-strain fracture toughness and strain energy release tests*

In the light of tensile results, formulations with the lowest and the highest amounts of CMC were selected for a deeper investigation of their fracture behavior, based on the determination of linear elastic fracture parameters: critical stress intensity factor K_{IC}, and critical strain energy release rate G_{IC}. Dried samples were tested. In Figure IV-35(a-c) representative load-displacement (P/u) curves obtained from flexural tests on SENB samples are reported, while in Table IV-12 K_{IC} and G_{IC} values are listed.

(a)

(b)

(c)
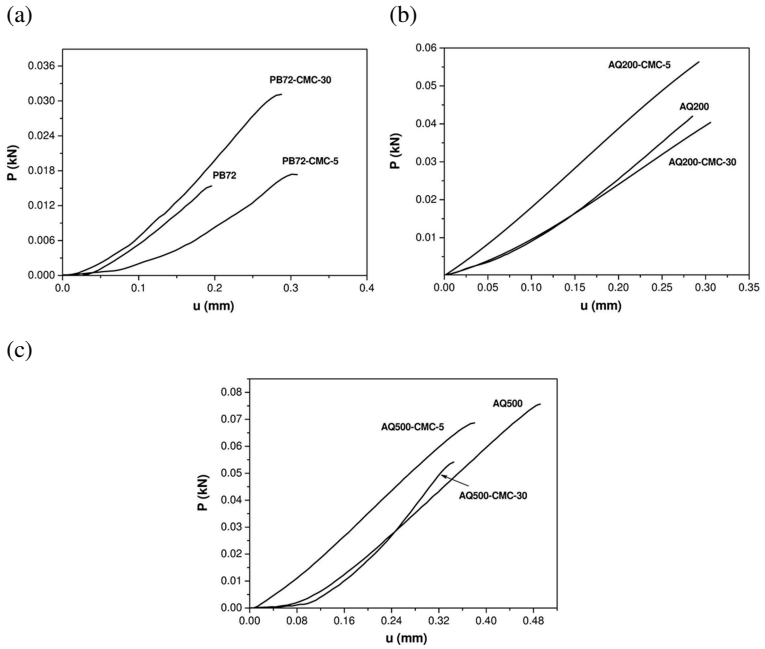
Figure IV- 35. Representative load-displacement curves of neat matrices and resulting composites from flexural test for the determination of K_{IC} and G_{IC} of (a) Paraloid B72, (b) Aquazol 200 and (c) Aquazol 500.

Table IV- 12. Critical stress intensity factor K_{IC}, and critical strain energy release rate G_{IC} values of neat matrices and resulting composites.

Sample	K_{IC} (MPa·m$^{1/2}$)	G_{IC} (kJ·m^{-2})
PB72	0.55 ± 0.03	0.12 ± 0.01
PB72-CMC-5	0.59 ± 0.02	0.16 ± 0.02
PB72-CMC-30	0.99 ± 0.03	0.31 ± 0.02
AQ200	1.16 ± 0.08	0.44 ± 0.04
AQ200-CMC-5	1.45 ± 0.24	0.84 ± 0.03
AQ200-CMC-30	1.31 ± 0.04	0.43 ± 0.04
AQ500	2.22 ± 0.22	1.40 ± 0.13
AQ500-CMC-5	1.82 ± 0.09	1.03 ± 0.19
AQ500-CMC-30	1.83 ± 0.14	0.55 ± 00.6

It is interesting to note that for Paraloid composites both fracture toughness parameters are noticeably increased upon CMC addition: K_{IC} rises from 0.55 MPa·m$^{1/2}$ for the neat matrix to 0.99 MPa·m$^{1/2}$ for PB72-CMC-30 samples, while, G_{IC} value passes from 0. 1 to 0. 3 kJ·m^{-2}. Therefore, even if quasi-static tensile tests evidence a slight reduction of TEB values, CMC introduction determines a substantial improvement of the fracture resistance of this material. In quasi-static tensile tests the presence of CMC microparticles could be responsible of the stress concentration and the crack nucleation, while, when a notch is already present on the sample the embrittling effect due to CMC is not effective and other mechanisms can be responsible of the toughening effect encountered for filled samples. It could be tentatively hypothesized that the presence of CMC flakes modify the crack propagation path, with positive effects on the fracture toughness of PB72. For Aquazol formulations no significant change in K_{IC} and G_{IC} are

determined except for AQ500 samples that register a decrease of G_{IC} as the filler loading increases. These results confirm the evidences already seen in ESEM micrographs of cryofractured surfaces of neat matrices and corresponding CMC composites (Figure IV-(2-4)) where only Paraloid filled samples exhibit an increase of the surface roughness.

4.1.3.4 Creep tests

In order to investigate the dimensional stability of all examined polymers after the addition of CMC flakes, creep tests were carried out on dried and conditioned samples. In Figure IV-36(a-c) representative creep compliance (D) curves of Paraloid and Aquazol microcomposites in the dry state are reported. In Figure IV-37(a-c) representative creep compliance curves of Paraloid and Aquazol conditioned microcomposites with the lowest and highest amounts of CMC are shown.

(a)   (b)
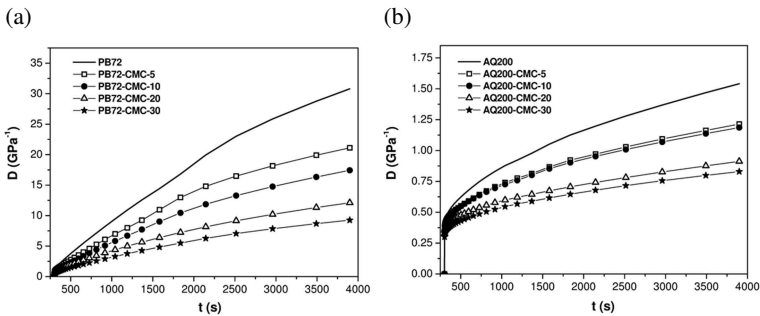
(c)
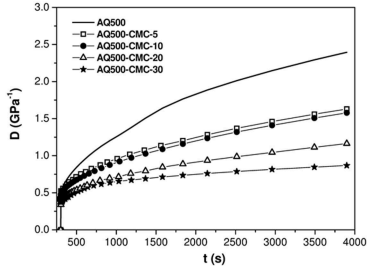
Figure IV- 36. Representative creep compliance curves of neat matrices and resulting composites in the dry state. (a) Paraloid B72, (b) Aquazol 200 and (c) Aquazol 500.

(a)
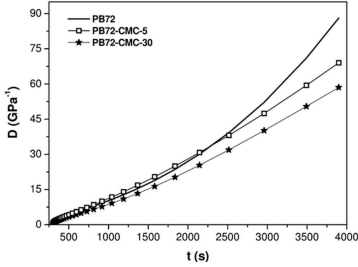
(b)
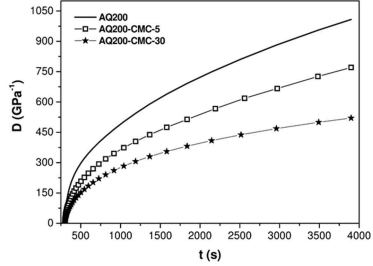
(c)
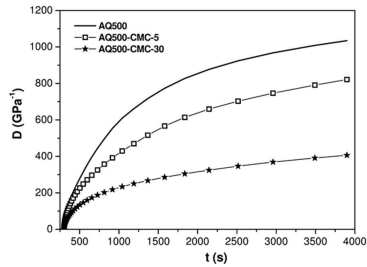
Figure IV- 37. Representative creep compliance curves of neat matrices and resulting composites in the conditioned state. (a) Paraloid B72, (b) Aquazol 200 and (c) Aquazol 500.

Creep tests verify the stabilization induced by CMC addition on polymers, with a remarkable and progressive reduction of creep compliance values regardless of matrices and the moisture content, especially for long creep times (3600 s). From the direct comparison between relative creep compliance values (normalized over the value corresponding to neat polymer matrices) at 3600 s of dried and wet samples (Figure IV-38(a-b)) it is interesting to note that PB72/CMC samples register a higher reduction of D in the dry state because of the light plasticizing action of moisture content. While, although the presence of water, it can be affirmed that dried and conditioned samples of both Aquazol have similar D values as a function of CMC amounts.

(a)   (b)
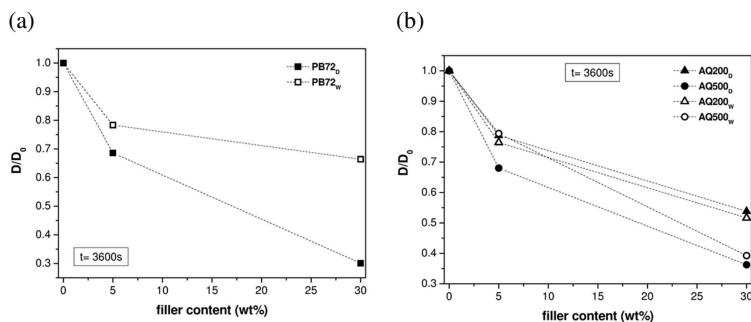
Figure IV- 38. Comparison of relative creep compliance values at 3600 s between dried and wet samples. (a) Paraloid B72, (b) Aquazol 200 and 500.

These results are particularly promising for Aquazol resins that being very hygroscopic materials even at low humidity levels (i.e. 55%) can turn into highly flexible films losing their dimensional stability and mechanical resistance. This aspect could play a positive role for those applications where a good dimensional stability of the adhesive resin is required (i.e. lining of oil painting canvas under constant long-lasting stress conditions).

4.2 Characterization of nanocomposites

All tests presented in this section were performed on nanocomposites films of Aquazol 500 filled with cellulose nanocrystals CNC, under dry conditions. CNC amounts of 5, 10 and 30 wt% were used. The same characterization was carried out on microcomposites films of the same polyamide filled with cellulose microcrystals CMC. In this way the comparison between micro- and nanocomposites obtained by solution mixing method was investigated.

4.2.1   Microstructural characterization

4.2.1.1   FESEM observations

The dispersion degree of cellulose nanocrystals within the matrix was evaluated trough FESEM observations of cryofractured surfaces of the neat matrix and the corresponding composites. FESEM images of AQ500 and resulting composites with 5-10 and 30 wt% of CNC are showed in Figure IV-39(a-d).

(a)
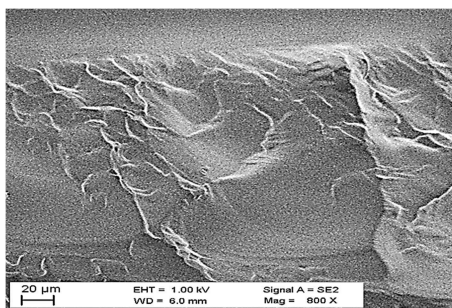
(b)
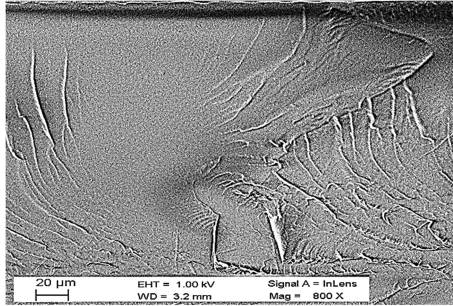
(c)
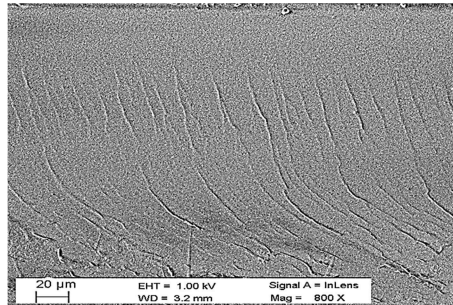
(d)
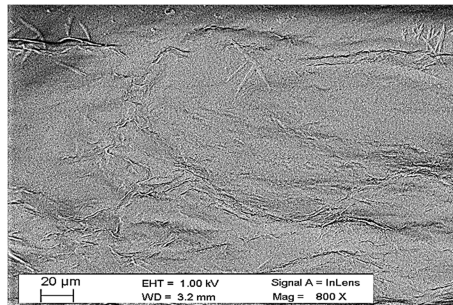
Figure IV- 39. FESEM images of cryofractured surfaces of (a) neat Aquazol 500 matrix and (b-d) resulting composites with 5wt%, 10wt% and 30wt% of CNC, respectively.

For all CNC composites it is not possible to detect any agglomeration of nanoparticles. Actually, Figure IV-40, reporting an enlargement of the cryofractured surface of AQ500-CNC-30 sample, verifies this evidence.
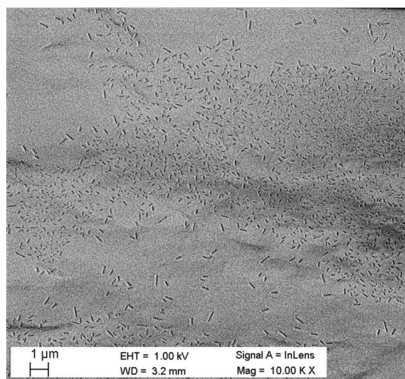
Figure IV- 40. FESEM image at higher magnification of the cryofractured surface of Aquazol 500 filled with 30 wt% of CNC

In fact, CNCs are homogeneously dispersed within the matrix even at highest amount of filler, without noticeable aggregates. Thanks to the image analysis software Jimage®, the size of these particles was determined. CNCs have a length between 100 - 500 nm and a width from 10 to 50 nm, similar to their initial size. The slight increase of their width could be related to the resolution limit of FESEM microscope that was not able to reach higher magnifications. This confirms the good stability of cellulose nanocrystals into aqueous polymeric solutions.

4.2.1.1.1   Comparison between micro- and nanocomposites

In Figure IV-41(a-d) FESEM images of neat AQ500 and microcomposites with 5-10 and 30 wt% of CMC are reported.

(a)

(b)

(c)

(d)
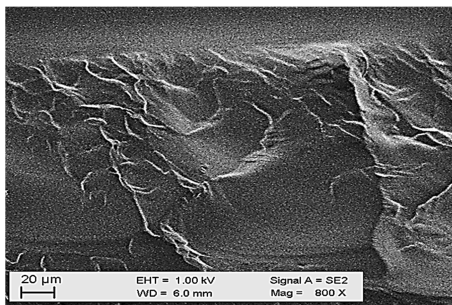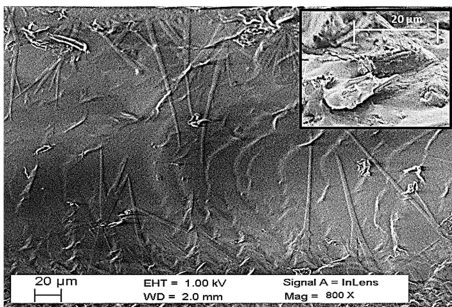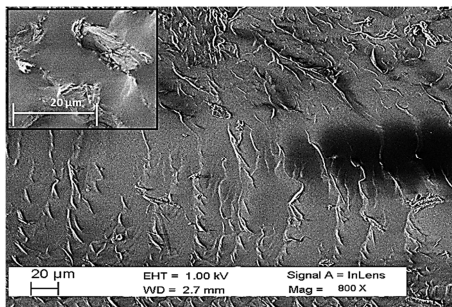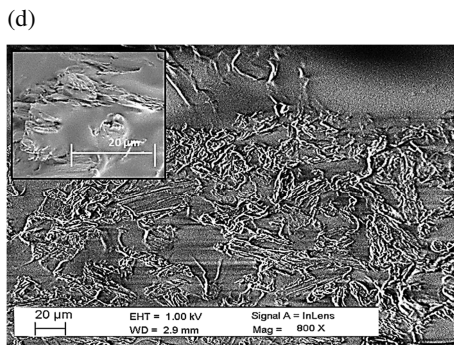
**Figure IV- 41. FESEM images of cryofractured surfaces of (a) neat Aquazol 500 matrix
and (b-d) resulting composites with 5wt%, 10wt% and 30wt% of CMC, respectively.**

CMC filled samples with lower filler amounts show how microcellulose particles are uniformly dispersed into the films without any preferential orientation and any significant agglomeration phenomena. In the enlarged pictures of each microcomposites section it is possible to recognize single flakes of CMC with an average size of 20 μm. For samples filled with 30 wt% of CMC a deposit phenomenon of the microfiller is noticed, probably occurred during the solvent clearing, evidencing that 30 wt% of CMC for this kind of composite processing is a critical amount and leads to the accumulation of CMCs at the bottom size of samples.

4.2.1.2   Differential scanning calorimetry (DSC)

In Figures IV-42(a-b) DSC thermograms of the neat matrix and relative CNC composites collected during the first and the second heating stage are reported. In Table IV-13 glass transition temperatures of nanocomposites collected during heating and cooling stages are summarized.

(a)   (b)
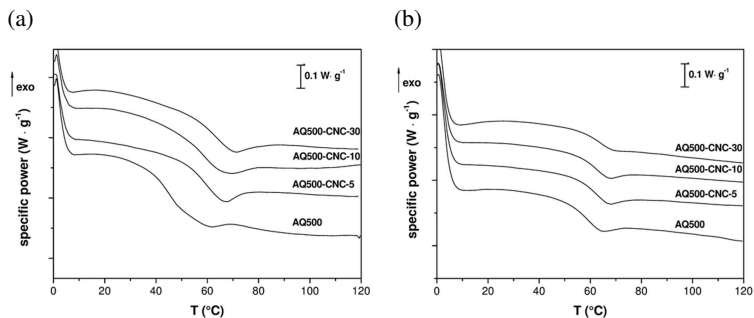
Figure IV- 42. DSC thermograms of neat AQ500 and corresponding nanocomposites. (a) First heating stage, (b) second heating stage.

All formulations report a systematic increase of the glass transition temperature T_g as the CNC amounts increases, in all stages.

Table IV- 13. Glass transition temperature (Tg) of neat AQ500 and relative nanocomposites from DSC tests.

	T_g °C		
Sample	**First heating**	**Cooling**	**Second heating**
AQ500	44.1	45.6	55.7
AQ500-CNC-5	55.4	50.5	59.4
AQ500-CNC-10	56.5	51.4	59.0
AQ500-CNC-30	57.1	51.9	61.3

4.2.1.2.1   Comparison between micro- and nanocomposites

In Figures IV-43(a-b) DSC thermograms of the neat matrix and relative CMC composites collected during the first and the second heating stages are

shown. In Table IV-14 glass transition temperatures of microcomposites collected during heating and cooling stages are listed.
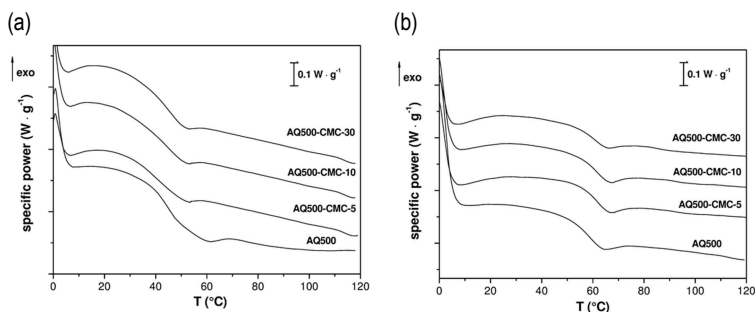
Figure IV- 43. DSC thermograms of neat AQ500 and corresponding microcomposites. (a) First heating stage, (b) second heating stage.

Table IV- 14. Glass transition temperature (Tg) of neat AQ500 and relative microcomposites from DSC tests.

Sample	T_g °C		
	First heating	Cooling	Second heating
AQ500	44.1	45.6	55.7
AQ500-CMC-5	44.4	50.5	62.2
AQ500-CMC-10	45.4	51.4	61.7
AQ500-CMC-30	44.8	51.9	62.0

All CMC formulations exhibit an increase of the glass transition temperature only in the second heating stage. The direct comparison between relative T_g trends of CMC and CNC composites (i.e. normalized over the value corresponding to the neat polymer matrix) as a function of the filler loading

is represented in Figure IV-44(a-b). One can notice how the nanosize of CNC makes it more able to interact with polymeric chains of AQ500 and modify their mobility with respect to CMCs. In fact AQ500/CNC samples in the first heating scan reach T_g values around 10 degrees higher than that of the neat matrix, while CMC does not practically affect the glass transition temperature of AQ500. On the other hand, the nanosize of CNC makes this filler more sensitive to the polymeric chains re-organization due to the second heating treatment that reduces the T_g increase seen in the first scan. In the second stage AQ500/CMC composites present the highest enhancement of T_g.

(a)   (b)
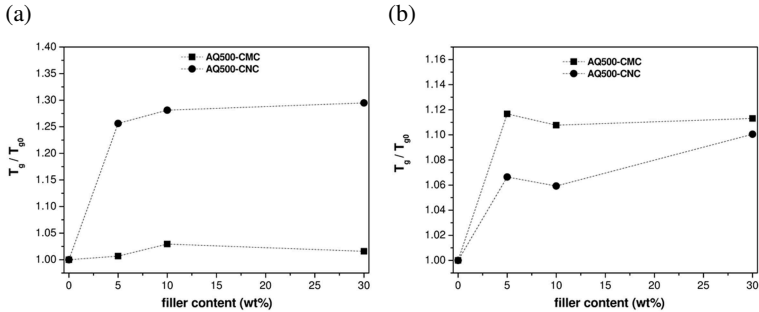
Figure IV- 44. Relative glass transition temperature (T_g) trends of Aquazol 500 based CMC and CNC composites. (a-b) First and second heating stage.

4.2.1.3   Thermogravimetric analysis (TGA)

TGA thermograms and derivative of the mass loss curves of AQ500 and corresponding nanocomposites are reported in Figure IV-45(a-b). The most important parameters regarding the thermal stability of the investigated materials are summarized in Table IV-15.

(a)   (b)
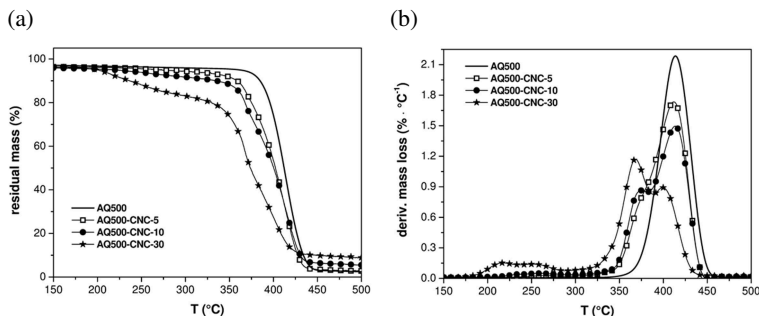
Figure IV- 45. TGA thermograms of neat AQ500 and resulting nanocomposites. (a)Residual mass as a function of temperature, (b) derivative of the mass loss.

Table IV- 15. Results of TGA tests on neat AQ500 and resulting nanocomposites.

Sample	T_{onset} (°C)	T_{max} (°C)	Residual mass at 700 °C (%)
AQ500	364	416	--
AQ500-CNC-5	271	410	--
AQ500-CNC-10	238	409	1.10
AQ500-CNC-30	198	367	4.45

It is evident a pronounced shift of the onset temperatures of nanocomposites towards lower values as the filler loading increases. This may be related to the hemicellulose and α-cellulose decomposition that anticipates the degradation step of nanocellulose typically centered at around 350 °C [132, 133]. Although the thermal stability of CNC is lower than the pure matrix, with a range of degradation temperatures between 250 and 400 °C [134], all compositions with 5 wt% and 10 wt% of nanofiller show only a slight decrease of the maximum degradation temperature T_{MAX}, while samples with the highest amount of CNC show a reduction of about 10% of this property. This underlines that a CNC amount of 30 wt% is quite critical for

the matrix in terms of degradation resistance. In particular, at the highest content of nanocellulose the T_{MAX} of AQ500 moves towards the CNC main degradation temperature because of the stronger influence of this filler on the neat matrix. Moreover, the residual mass at 700 °C increases proportionally to the filler content in all formulations. As well known in literature, sulfate groups, present on the surface of CNCs, allow the formation of a ceramized surface layer on the samples that may act as a flame retardant, impeding the complete combustion and vaporization of the matrix [135].

4.2.1.3.1   Comparison between micro- and nanocomposites

In Figures IV-46(a-b) TGA thermograms and derivative of the mass loss curves of the neat AQ500 and relative CMC composites are presented. In Table IV-16 the most important parameters regarding the thermal stability of microcomposites are collected.

(a)   (b)
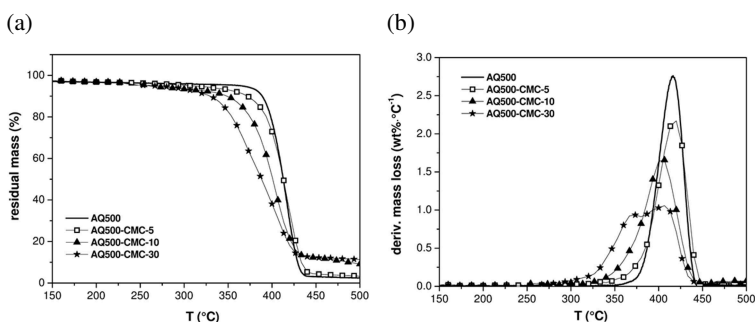
**Figure IV- 46. TGA thermograms of neat AQ500 and resulting microcomposites.
(a)Residual mass as a function of temperature, (b) derivative of the mass loss.**

Table IV- 16. Results of TGA tests on neat AQ500 and resulting microcomposites.

Sample	T_{onset} (°C)	T_{max} (°C)	Residual mass at 700 °C (%)
AQ500	364	416	--
AQ500-CMC-5	313	418	--
AQ500-CMC-10	276	405	0.30
AQ500-CMC-30	267	403	3.91

CMC filled formulations register a progressive decrease of the onset temperature as the filler content increases due to the lower thermal stability of the microcellulose with respect to AQ500 (Table IV-2). Also the decrease of the matrix thermal stability, evident in the reduction of the maximum degradation temperature, T_{MAX}, is observed since the 10 wt% of CMC. The presence of a char enriched surface layer on CMC samples produces a residual mass at 700 °C that increases proportionally to the filler content for all microcomposites. Figure IV-47(a-b) reports the relative T_{onset} and T_{max} trends of CMC and CNC composites (i.e. normalized over the value corresponding to the neat matrix) as a function of the filler loading.

(a)

(b)
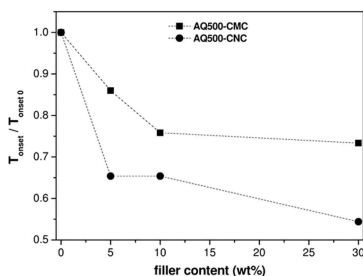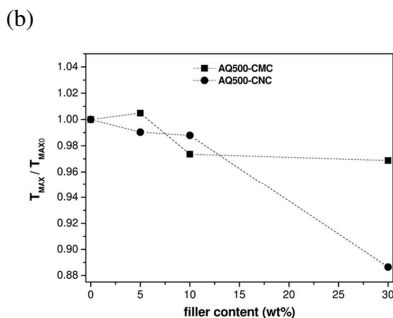
Figure IV- 47. Relative TGA properties trends of Aquazol 500 CMC and CNC composites (a) Temperature associated to the beginning of the degradation (T_{onset}), (b) temperature associated to the maximum mass loss rate (T_{max}).

A more relevant shift of the AQ500 onset temperature towards lower values (upon around 45% less) is shown by all CNC filled films as the filler loading increases. At the highest filler concentration, AQ500/CNC composites register the most relevant fall in thermal stability of about 10% in comparison to the unfilled samples.

4.2.2   Physical characterization

Aquazol 500 has been introduced as adhesive in the conservation of oil paintings, and other art objects, even for its elevated transparency. The addition of a filler in a polymeric matrix can impair its optical features. For this reason the assessment of the transparency degree of AQ500 based micro- and nanocomposites was conducted.

4.2.2.1   Optical transparency assessment

In Figure IV-48 optical pictures of thin films of neat matrix and its relative nanocomposites with 5, 10 and 30 wt% of CNC are presented.

(a)
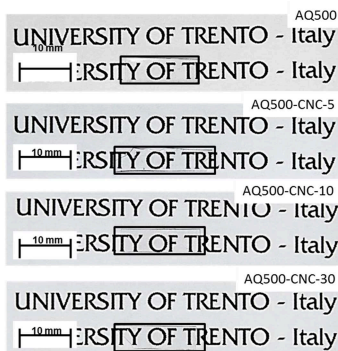
(b)

Figure IV- 48. Optical images of thin composite films showing the effect of the addition of 5, 10 and 30 wt% of (a) CNC, (b) CMC on the optical properties of Aquazol 500.

Remarkable, CNC has no effect on the optical aspect of the neat polymer even at high filler amounts. All observed CNC filled films are transparent and do not exhibit any chromatic variation as well. After the introduction of CMC, AQ500 shows a chromatic change, passing from a colorless material

to light yellow/brown one proportionally to the CMC loading, as already seen for melt-compounded microcomposites (Figure IV-17).

4.2.2.2   UV-vis spectroscopy analysis

In Figure IV-49 relative transmittance (T) spectra of pure AQ500 and corresponding CNC composites are reported. The introduction of CNCs even at highest filler amounts has no significant effect on the transmittance of the neat adhesive, especially, in the visible wavelengths interval (400-800 nm). Also after the addition of 30 wt% of nanocellulose, AQ500 maintains its initial T values.
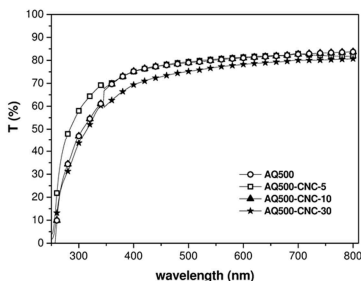
Figure IV- 49. Relative transparency (T) spectra of neat AQ500 and resulting nanocomposites.

4.2.2.2.1   Comparison between micro- and nanocomposites

In Figure IV-50 relative transmittance (T) spectra of AQ500 and corresponding CMC composites are shown.
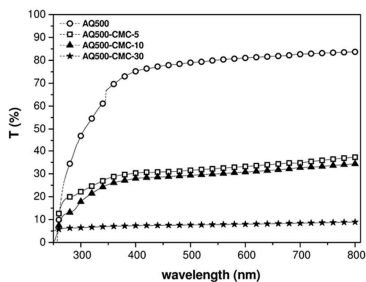
Figure IV- 50. Relative transparency (T) spectra of neat AQ500 and resulting microcomposites.

The presence of CMC produces a reduction of T since the lowest amount of filler. The direct comparison between relative T trends (i.e. normalized over the value corresponding to the neat polymer) of CMC and CNC composites as a function of filler content, evaluated in the visible wavelengths range is reported in Figure IV-51.
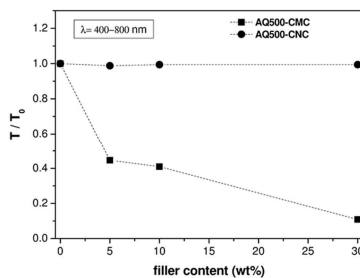
Figure IV- 51. Relative transparency values in the visible wavelengths range as function of the filler content of CMC and CNC composites.

Through Figure IV-51 one can appreciate better the advantage of the use of CNC instead of CMC as filler. In fact, if CMC introduction leads to a drop in T up to about 60% for AQ500 filled with 5-10 wt%, reaching the 90% less of transmittance with samples at 30 wt% of microcellulose in comparison to the unfilled polyamide, T values of CNC composites remains unvaried regardless of the filler content.

4.2.3   Mechanical characterization

4.2.3.1   Dynamic mechanical thermal analysis (DMTA)

The storage modulus (E'), loss modulus (E") and tanδ curves of the neat matrix and corresponding CNC composites in the dry state, obtained from DMTA analysis, are reported in Figure IV-52(a-c). In Table IV-17 the viscoelastic properties of AQ500/CNC formulations are shown.
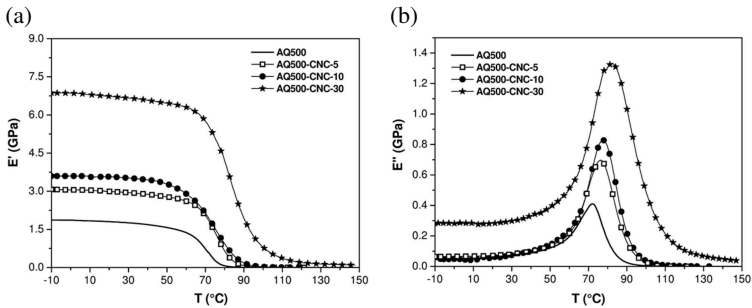
(c)
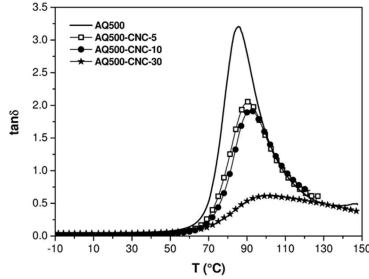
Figure IV- 52. DMTA thermograms of neat AQ500 and resulting nanocomposites (f = 1 Hz). (a) Storage modulus E', (b) loss modulus E'', (c) loss factor tanδ.

Table IV- 17. Results of DMTA tests on neat AQ500 and resulting nanocomposites.

Sample	E' at 25°C (GPa)	E'' peak value (GPa)	tanδ peak value	T_g from E'' (°C)
AQ500	1.86	0.41	3.21	72.0
AQ500-CNC-5	3.06	0.70	2.23	74.7
AQ500-CNC-10	3.72	0.82	1.88	77.1
AQ500-CNC-30	6.86	1.33	0.78	82.6

CNC promotes a remarkable increase of both the storage and the loss moduli (E' and E'') proportionally to the filler content. Formulations with 30 wt% of CNC register a value of E' around three times higher than that reported by the neat matrix. Correspondingly, loss factor (tanδ) values decrease as the filler amount increases. Another action of CNCs on AQ500 is the progressive enhancement of its glass transition temperature T_g, determined from the shift of the E'' peak towards higher temperatures. In particular, samples with the highest amount of CNC have a Tg increase of about 10

degrees. In Figure IV-53(a-b) thermal strain curves of AQ500 composites, used for the determination of the coefficient of liner thermal expansion (CLTE) are shown. CLTE values below and above T_g of all nanocomposites are listed in Table IV-18.

(a)   (b)
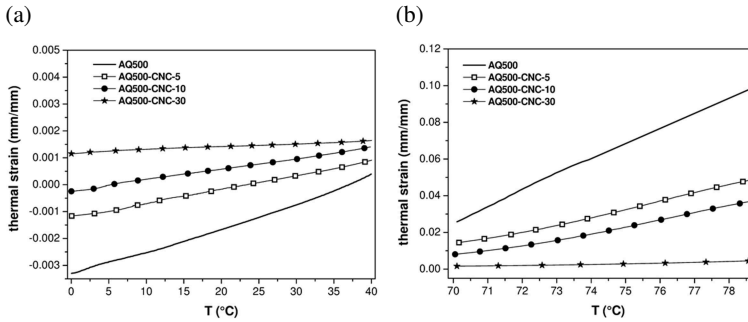
Figure IV- 53. Thermal strain curves of AQ500/CNC composites. (a) Below T$_g$, between 0 °C and 40 °C, (b) above T$_g$, between 70 °C and 80 °C.

Table IV- 18. Coefficient of linear thermal expansion values of nanocomposites calculated in the glassy (CLTE$_g$) and in the rubbery (CLTE$_r$) states.

Sample	CLTE$_g$ (K^{-1})	CLTE$_r$ (K^{-1})
AQ500	8.9E-05	8.7E-03
AQ500-CNC-5	5.9E-05	4.2E-03
AQ500-CNC-10	3.9E-05	3.5E-03
AQ500-CNC-30	1.0E-05	3.3E-04

CNC produces the enhancement of the dimensional stability of the neat matrix with the progressive reduction of both coefficients of linear thermal expansion (CLTE) below and above Tg as the filler content increases.

4.2.3.1.1   Comparison between micro- and nanocomposites

The storage modulus (E'), loss modulus (E'') and tanδ curves of neat AQ500 and corresponding CMC composites in the dry state are reported in Figure IV-54(a-c). In Table IV-19 the viscoelastic properties of AQ500/CMC formulations are listed.

(a)   (b)

(c)
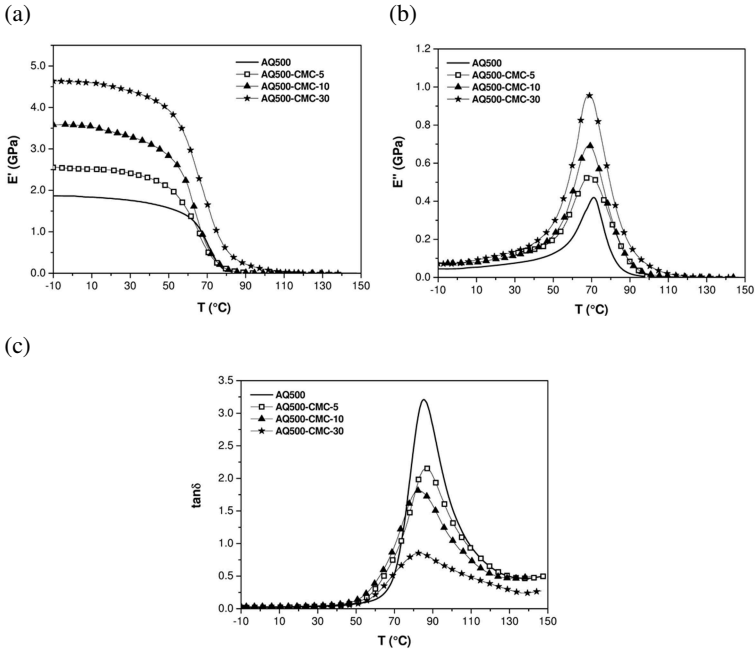
Figure IV- 54. DMTA thermograms of neat AQ500 and resulting microcomposites (f = 1 Hz). (a) Storage modulus E', (b) loss modulus E'', (c) loss factor tanδ.

Table IV- 19. Results of DMTA tests on neat AQ500 and resulting microcomposites.

Sample	E' at 25°C (GPa)	E'' peak value (GPa)	tanδ peak value	T_g from E'' (°C)
AQ500	1.86	0.41	3.21	72.0
AQ500-CMC-5	2.53	0.53	2.16	69.1
AQ500-CMC-10	3.55	0.69	1.81	68.9
AQ500-CMC-30	4.60	0.96	0.84	68.9

Both storage and loss moduli (E' and E'') are proportionally increased thanks to the presence of CMC. AQ500-CMC-30 samples register an E' value about two times higher than that of the neat matrix. Correspondingly, loss factor (tan δ), values decrease as the filler amount increases, confirming that the positive contribution of the CMC addition on the E' is higher than the E'' enhancement see (Table IV-5). For CMC compositions no significant effect on the AQ500 T_g is detected. In Figure IV-55(a-b) thermal strain curves of AQ500 microcomposites, used for the determination of the coefficient of liner thermal expansion (CLTE) are shown. CLTE values below and above T_g of all CMC composites are collected in Table IV-20.

(a)

(b)
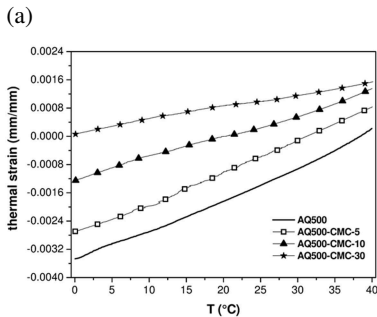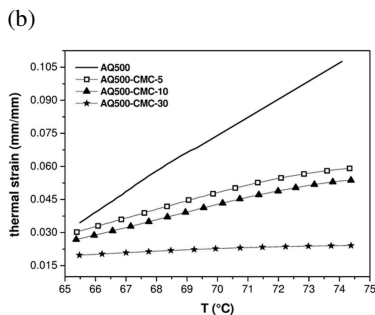
Figure IV- 55. Thermal strain curves of AQ500/CMC composites. (a) Below T$_g$, between 0 °C and 40 °C, (b) above T$_g$, between 65 °C and 75 °C.

Table IV- 20. Coefficient of linear thermal expansion values of microcomposites calculated in the glassy (CLTE$_g$) and in the rubbery (CLTE$_r$) states.

Sample	CLTE$_g$ (K^{-1})	CLTE$_r$ (K^{-1})
AQ500	8.9E-05	8.7E-03
AQ500-CMC-5	9.0E-05	3.9E-03
AQ500-CMC-10	6.0E-05	3.5E-03
AQ500-CMC-30	3.5E-05	6.7E-04

CMC is able to gradually reduce the thermal strain of AQ500 and thus leads to a proportional decrease of CLTE in both glassy and rubbery states as the filler loading increases. The comparison between CNC and CMC composites of Aquazol 500 described in Figure IV-56(a-f), show the relative DMTA properties trends (i.e. normalized over the value corresponding to the neat matrix) as a function of the filler loading.

(a)

(b)

(c)

(d)

(e)

(f)
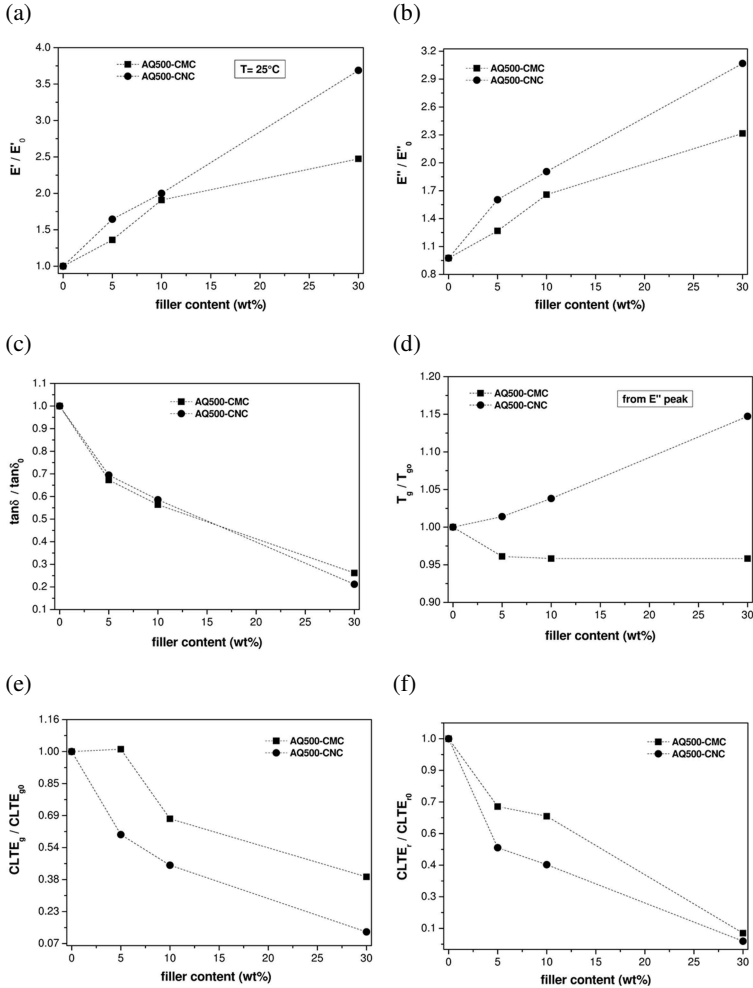
Figure IV- 56. Relative DMTA properties trends. Comparison between CMC and CNC composites:(a) Storage modulus, (b) loss modulus, (c) loss factor (d) glass transition temperature and (e-f) coefficient of linear thermal expansion below and above T_g.

Although both fillers produce similar effects on the stiffness and the dimensional stability of the neat AQ500, is evident that CNCs are much more powerful than CMC flakes. Formulations with 30 wt% of CNC suspensions reach E' values even three times higher than the neat AQ500 and register a thermal displacement reduction of about 90% with respect to CLTE values of microcomposites that are 40% lower than the neat polymer (Figure IV-56e). Only CNC is able to modify the T_g of the neat Aquazol (Figure IV-56d).

4.2.3.2   Creep tests

In Figure IV-57 representative creep compliance (D) curves of Aquazol 500 nanocomposites in the dry state are reported.
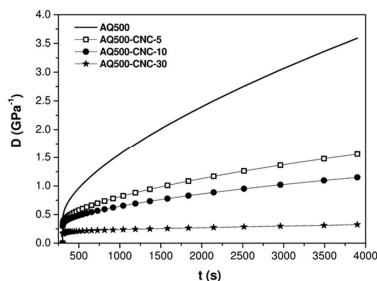
Figure IV- 57. Representative creep compliance curves of neat Aquazol 500 and resulting nanocomposites.

It is clear from Figure IV-57 that creep tests confirm the significant increase of the dimensional stability of AQ500 due to the CNC introduction. The creep compliance of this polymer decreases with increasing the filler content.

4.2.3.2.1   Comparison between micro- and nanocomposites

In Figure IV-58 representative creep compliance (D) curves of Aquazol 500 microcomposites in the dry state are reported.
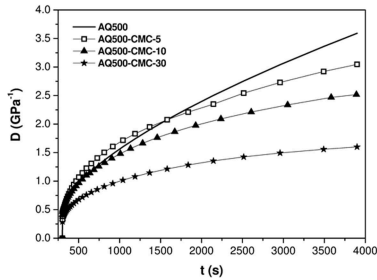
Figure IV- 58. Representative creep compliance curves of neat Aquazol 500 and resulting microcomposites.

Also the CMC addition promotes a stabilizing effect on the neat AQ500. In fact, all microcomposites exhibit a progressive reduction of the creep elongation as the CMC loading increases. In Figure IV-59 the comparison between relative D trends (i.e. normalized over the value corresponding to the neat polymer) of CMC and CNC composites as a function of the filler loading are shown.
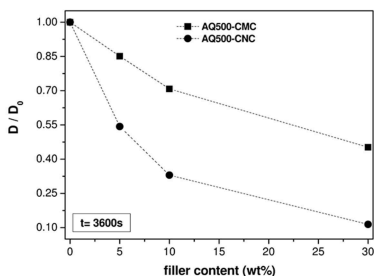
Figure IV- 59. Relative creep compliance (D) trends. Comparison between CMC and CNC composites.

Again the CNC action on the increment of the creep resistance is more pronounced than CMC one. If CMC filled films, after a testing time of 3600s, can reduce D up to 60% less than the neat matrix value, CNC films are able to reach the 90% less. This is a very important result, considering the end use of AQ500 in the field of cultural heritage conservation as a consolidant/adhesive for oil paintings, which being fixed to a stretcher, are subjected to long-lasting constant stresses.

4.3   *Consolidation of degraded wood*

A consolidation work has to recover the mechanical properties of damaged artworks which because of decay processes are subjected to a mechanical performance loss. On the basis of the mechanical improvements of Paraloid B72 after the CMC introduction, it was decided to orient the experimental formulations with the lowest and the highest amounts of CMC to the restoration of decayed wood. Neat and filled Paraloid melt-compounded composites with 5 wt% and 30 wt% of CMC were applied as consolidant solutions in acetone on two species of historical degraded wood (18th

century). The wood types selected for this work are a hardwood Persian walnut (Juglans regia) and a softwood European silver fir (Abies alba). The two wood samples exhibit different conservation conditions. The Persian walnut presents an advanced biological decay with evident holes and tunnels made by larval worms that interested also the inner part of the wood. The silver fir shows a better conservation degree with larvae holes and galleries not so diffused as in the walnut case.

4.3.1   Brookfield tests

One of the most important parameter for a successful wood consolidation is the level of penetration of the consolidating material into the artwork. In fact, these restoration operations involve the substrate of wooden paintings or sculptures, therefore, it is very important that the viscosity of consolidant polymers is low enough to penetrate into the wood, but not too low to reach also the paint film and thus destroying the artwork. Thanks to its optimal viscosity, Paraloid B72, in concentration range of 3-10 wt%, is one of the most used consolidant resin for wood [18]. In order to assess the possible effect of CMC introduction on this property, Brookfield rheological tests on neat Paraloid and its resulting CMC composites solutions in acetone were carried out. In Figure IV-60 reports the viscosity/angular velocity (η/ω) curves of PB72/CMC samples.
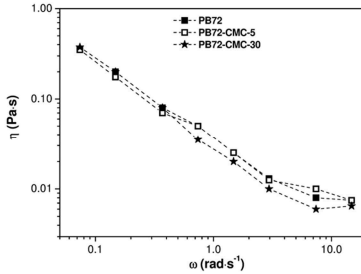
Figure IV- 60. Brookfield rheological curves of neat Paraloid and CMC composites.

It is worthwhile to observe that, even at the highest amount of CMC, the viscosity of the polymer matrix does not change to a significant extent.

4.3.2 Physical characterization

Wood samples for physical characterization were dried under vacuum at 105 °C until the achievement of a constant weight and then conditioned in a climatic chamber at a temperature of 23°C and a relative humidity of 65% upon a constant weight was reached.

4.3.2.1 Gravimetric analysis

Figure IV-61(a-b) shows moisture absorption kinetic curves of undamaged and damaged walnut and fir wood before and after treatments with pure PB72 and PB72/CMC composites. In Table IV-21 the moisture content (M%), the oven-dry density (ρ_0), the density at 65% of relative humidity level (ρ_{12}) and the volumetric swelling (S) are listed.

(a)

(b)
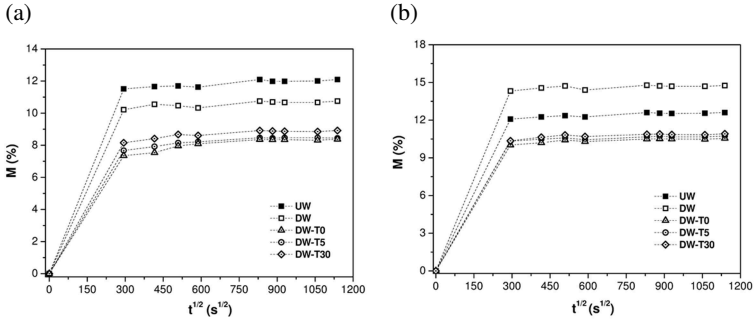
Figure IV- 61. Moisture absorption kinetic curves of undamaged and damaged wood samples untreated and treated with neat Paraloid and CMC-based composites. (a) Walnut, (b) Fir.

Table IV- 21. Gravimetric analysis results of undamaged and damaged walnut and fir wood samples before and after consolidation with neat PB72 and corresponding CMC composites.

Sample	M% (wt%)	ρ_0 (g·cm^{-3})	ρ_{12} (g·cm^{-3})	S (%)
walnut				
UW	12.23 ± 0.13	0.68 ± 0.01	0.69 ± 0.01	7.82 ± 0.18
DW	11.20 ± 0.09	0.60 ± 0.01	0.57 ± 0.01	7.29 ± 0.35
DW-T0	8.27 ± 0.30	0.63 ± 0.01	0.66 ± 0.02	3.43 ± 0.59
DW-T5	8.46 ± 0.45	0.63 ± 0.02	0.66 ± 0.02	3.69 ± 0.25
DW-T30	8.98 ± 0.32	0.66 ± 0.02	0.68 ± 0.03	3.60 ± 0.43
fir				
UW	12.50 ± 0.56	0.36 ± 0.01	0.39 ± 0.01	7.36 ± 0.13
DW	14.65 ± 0.15	0.35 ± 0.01	0.37 ± 0.01	8.65 ± 0.55
DW-T0	10.49 ± 0.45	0.40 ± 0.01	0.42 ± 0.01	3.84 ± 0.57
DW-T5	10.70 ± 0.26	0.39 ± 0.01	0.41 ± 0.01	4.11 ± 0.69
DW-T30	10.94 ± 0.40	0.42 ± 0.01	0.44 ± 0.02	4.23 ± 0.15

Generally speaking, degraded wood tends to absorb more water than modern intact wood and the consolidation with Paraloid is able to reduce the moisture sorption of the two species of damaged wood [18, 22]. Comparing the physical behavior of the two types of decayed wood with their corresponding intact modern wood, it is possible to notice that both of them manifest a decrease of dry and wet densities, ρ_0 and ρ_{12} because of the decay process. Moreover, damaged walnut wood samples tend to absorb less moisture, M%, than intact wood and are characterized by a lower value of volumetric swelling, S. Ancient fir wood samples register higher values of M% and S in comparison to modern fir samples. This could be related to their different conservation conditions. In fact, degraded walnut wood shows holes and larval tunnels that are not so numerous in degraded fir samples. Maybe, the critical biological decay of walnut reduced the wooden matter able to interact with the environment, producing a decrease of the moisture content. For as the effects of consolidation treatments is concerned, the application of all formulations leads to a decrease of about 25% of the moisture sorption for both wood species. In particular, a slight increase of the absorbed water for walnut and fir degraded wood samples treated with CMC filled PB72, proportional to the filler loading is detected (Figure IV-61(a-b)). This may be due to the lower amount of Paraloid in composite solutions, but this variation is less than 0.5% even for formulations with the highest amount of filler. For both investigated wood types the increase of the CMC loading produces a systematic reduction of the volumetric swelling and an enhancement of dry and wet densities values. Worm-eaten walnut samples, treated with PB72-CMC-30, almost reach density values of their corresponding intact wood, while values detected for damaged fir samples exceed the reference ones.

4.3.2.2   Mercury intrusion porosimetry

Table IV-22 reports the values of the percentage of total porosity, P_{TOT}, and the pore radius for the different groups of wood. Also in this case there is a different degradation level noticeable for the two wood species. Before treatments, walnut samples display a stronger decrease of the total porosity in comparison to the modern wood, while degraded fir samples present a value of P_{TOT} similar to that of their corresponding intact wood. Ancient walnut samples show a much more significant increase of the pore radius with respect to fir samples. This can be explained, considering the metabolism action of woodworm larvae that, making galleries and holes, enlarges the pore size of wood and thus reduces the percentage of its closed porosity. For both damaged wood types, CMC composites induce a progressive reduction of the pore radius that becomes much closer to that one of their corresponding intact wood. For walnut, the neat PB72 application increases the P_{TOT}, filling the worm tunnels. For all wood samples, there is a slight decrease of this property as the CMC content increases in comparison to samples treated with the neat resin, probably related to the lower amount of PB72 in composites solutions.

Table IV- 22. Results from mercury intrusion porosimetry analysis of undamaged and damaged walnut and fir wood before and after consolidation with neat PB72 and corresponding CMC composites.

Sample	P_{TOT} (%)	Pore radius (nm)
walnut		
UW	40.89	350.3
DW	26.98	1614.3
DW-T0	37.24	711.8
DW-T5	35.99	356.9
DW-T30	33.76	318.5
fir		
UW	62.22	136.4
DW	60.84	292.4
DW-T0	55.77	191.2
DW-T5	47.30	144.9
DW-T30	40.56	141.1

4.3.2.3 Assessment of the penetration degree of consolidant solutions

4.3.2.3.1 Optical microscope observations

In Figure IV-62(a-d) and IV-63(a-d) optical microscope images of surfaces of damaged wood samples of walnut and fir before and after consolidant treatments are respectively reported.

(a)

(b)

(c)

(d)

Figure IV- 62. Optical microscope images of surfaces of damaged walnut samples untreated (a) and treated with neat Paraloid (b) and microcomposites with 5 wt% and 30 wt% of CMC (c-d).

(a)
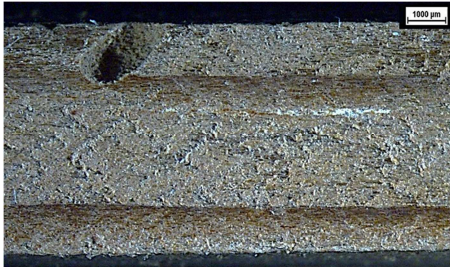
(b)
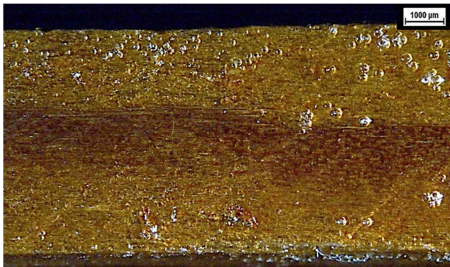
(c)
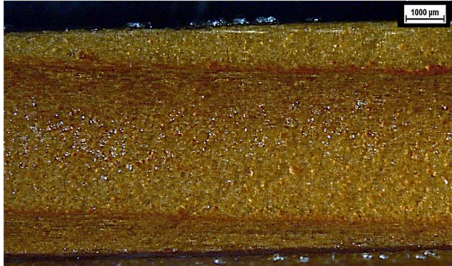
(d)
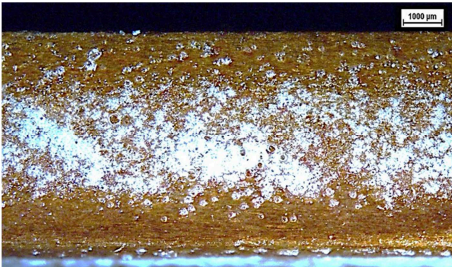
Figure IV- 63. Optical microscope images of surfaces of damaged fir samples untreated (a) and treated with neat Paraloid (b) and microcomposites with 5 wt% and 30 wt% of CMC (c-d).

All formulations create a surface transparent coating on each type of wood. Only samples treated with the composition at the highest amount of CMC present a visible exterior deposit of this microfiller.

In Figure IV-64(a-d) and IV-65(a-d) optical microscope images of long cross-sections of damaged wood samples of walnut and fir before and after consolidant treatments are respectively presented.

(a)
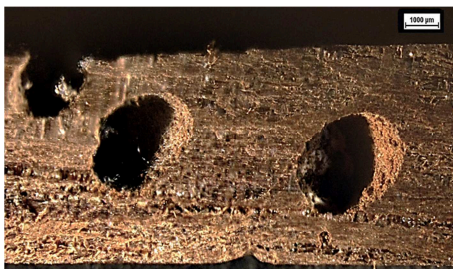
(b)

(c)

(d)

Figure IV- 64. Optical microscope images of long cross-sections of damaged walnut samples untreated (a) and treated with neat Paraloid (b) and microcomposites with 5 wt% and 30 wt% of CMC (c-d).

(a)
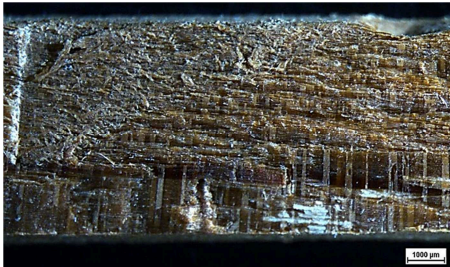
(b)
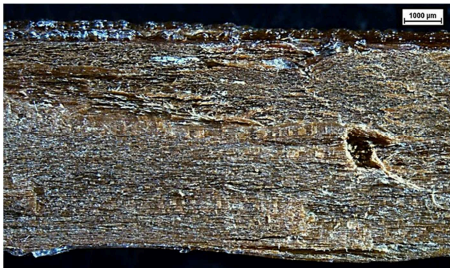
(c)
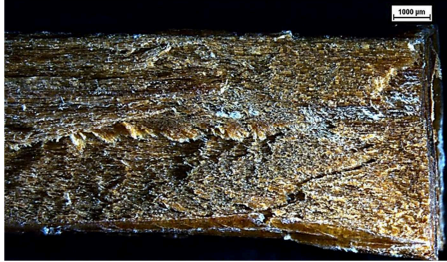
(d)
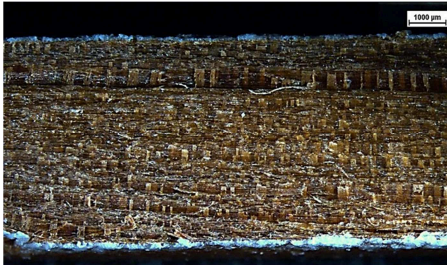
Figure IV- 65. Optical microscope images of long cross-sections of damaged fir samples untreated (a) and treated with neat Paraloid (b) and microcomposites with 5 wt% and 30 wt% of CMC (c-d).

Only for walnut samples it is possible to assess the presence of consolidants in the long cross-sections, and how PB72 and, especially, CMC are able to partially fill the defects made by larvae worms. These defects into the wood become ways of penetration for consolidant solutions. While, in the inner sections of fir samples the consolidants penetration is not perceivable.

Moreover, the comparison between surfaces and long cross-sections images of decayed walnut and fir samples proves the different degradation state of these two wood types, with evident larval holes and galleries on the surfaces and in the inner of just walnut samples.

4.3.2.3.2   Fourier transform infrared spectroscopy (FTIR)

FTIR spectra of surfaces of untreated and treated degraded wood samples of walnut and fir (Figure IV-66(a-b)) confirm the formation of a surface transparent protective layer, through the presence in all FTIR curves of the main stretching peak of carbonyl groups at about 1750 cm^{-1} typical of PB72.

(a)   (b)
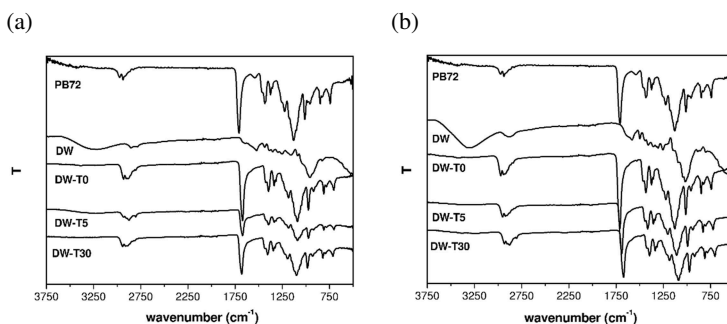
Figure IV- 66. FTIR spectra of surfaces of damaged wood samples untreated and treated with neat Paraloid and CMC composites. (a) Walnut, (b) fir.

Additionally, Figure IV-67(a-b) shows the FTIR spectra of long cross-sections of untreated and treated decayed walnut and fir samples, respectively.

(a)   (b)
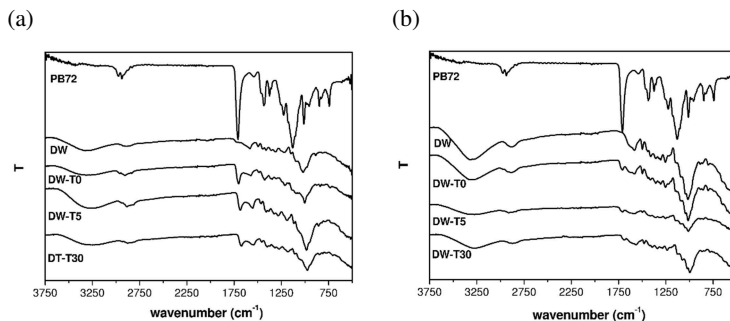
Figure IV- 67. FTIR spectra of long cross-sections of damaged wood samples untreated and treated with neat Paraloid and CMC composites. (a) Walnut, (b) fir.

According to optical observations, the presence of the PB72 carbonyl group peak in the walnut wood long cross-sections spectra underlines the higher penetration degree of unfilled and filled Paraloid consolidants within this wood, through worm holes and galleries that are preferential ways of penetration. For fir samples a very low carbonyl signal was detected, verifying the essentially surface nature of PB72/CMC consolidation treatments for this degraded wood.

4.3.3   Mechanical characterization

Before testing, samples were conditioned at 23°C and 55% of relative humidity in a chamber with a super-saturated solution of $Mg(NO_3)_2 \cdot 6H_2O$ until a constant weight was achieved.

4.3.3.1   *Three points flexure tests*

In Figure IV-68(a-b) the representative force/displacement (F/u) curves of
each group of tested walnut and fir samples are presented, while, in Table
IV-23 the main flexural properties in quasi-static condition are listed.

(a)   (b)
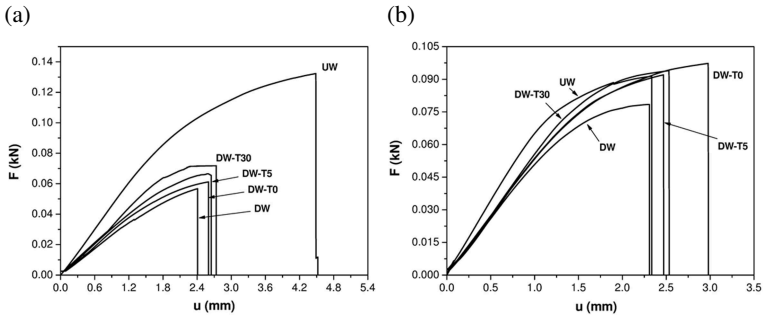
**Figure IV- 68. Representative force/displacement curves of the quasi-static flexural
tests on undamaged and damaged wood samples before and after consolidation with
neat Paraloid and CMC composites. (a) Walnut, (b) fir.**

**Table IV- 23. Results of quasi-static flexural tests on undamaged and damaged walnut
and fir wood samples before and after consolidation with neat PB72 and corresponding
composites.**

Sample	E_f (GPa)	$\sigma_{MAX,f}$ (MPa)	$\varepsilon_{MAX,f}$
walnut			
UW	6.97 ± 0.46	115.41 ± 6.12	0.115 ± 0.011
DW	4.92 ± 0.37	49.72 ± 1.32	0.060 ± 0.011
DW-T0	4.57 ± 0.66	53.88 ± 0.25	0.068 ± 0.009
DW-T5	5.37 ± 0.29	62.65 ± 4.47	0.068 ± 0.008
DW-T30	5.45 ± 0.44	63.94 ± 3.92	0.066 ± 0.006

Sample	E_f (GPa)	$\sigma_{MAX,f}$ (MPa)	$\varepsilon_{MAX,f}$
fir			
UW	7.87 ± 0.59	71.62 ± 4.00	0.058 ± 0.004
DW	5.99 ± 0.40	56.36 ± 4.03	0.061 ± 0.005
DW-T0	5.99 ± 0.17	68.57 ± 1.56	0.074 ± 0.005
DW-T5	6.34 ± 0.20	65.24 ± 3.42	0.071 ± 0.007
DW-T30	6.43 ± 0.24	66.26 ± 1.10	0.071 ± 0.006

First of all one can notice the drastic drop in mechanical properties for decayed walnut and fir due to the decay process. The neat PB72 based treatment is able to raise both maximum flexural stress and strain of the two types of wood, but has not effect on the elastic modulus, E_f. Remarkably, all wood samples treated with microcomposites show a systematic increase of E_f as the CMC content increases. For walnut a progressive enhancement of $\sigma_{MAX,f}$ with increasing of CMC loading is registered. On the other hand, there is no relevant effect of CMC on the maximum flexural strain of walnut wood. For fir wood, considering standard deviation values, it is possible to affirm that the presence of CMC does not significantly affect the flexural strength of consolidated samples. After the consolidation with microcomposites, decayed fir samples exhibit a slight decrease of $\varepsilon_{MAX,f}$. The flexural behavior of treated damaged fir samples could be related to the almost null penetration of Paraloid based consolidants into this wood and the lower concentration of this resin in composites solutions.

In Figure IV-69(a-b) and IV-70(a-b) the values of E_f and $\sigma_{MAX,f}$ for each group of tested walnut and fir samples are respectively plotted.

(a)

(b)
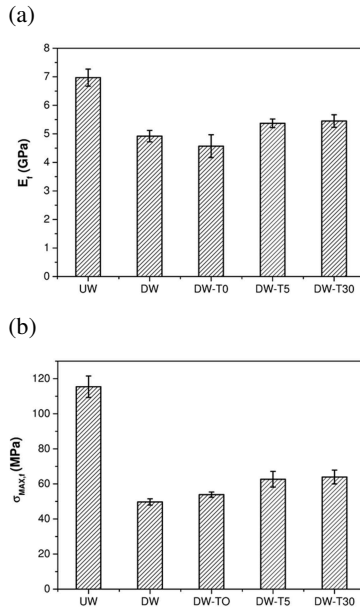
Figure IV- 69. Main quasi-static flexural properties of undamaged and damaged walnut wood samples untreated and treated with neat Paraloid and CMC composites. (a) flexural modulus, E_f, (b) maximum flexural stress, $\sigma_{MAX,f}$.

(a)

(b)
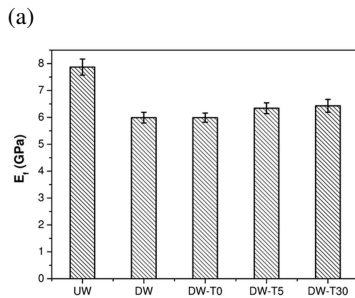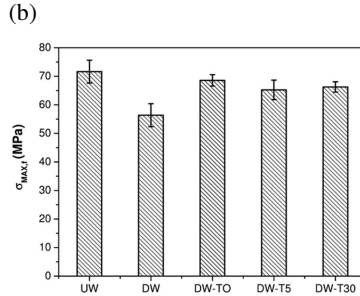
Figure IV- 70. Main quasi-static flexural properties of undamaged and damaged fir wood samples untreated and treated with neat Paraloid and CMC composites. (a) flexural modulus, E_f, (b) maximum flexural stress, $\sigma_{MAX,f}$.

From Figure IV-69(a-b) and IV-70(a-b) it is clear that both of the two species of damaged wood present an important decrease of their flexural properties because of the degradative process. In particular, worm-eaten walnut samples register the highest fall in flexure strength, with a reduction of about 50% of $\sigma_{MAX,f}$ with respect to damaged fir samples that register a $\sigma_{MAX,f}$ decrease of about 20%. The effect of CMC on the consolidating properties of PB72 is evident since the lowest amount of this microfiller and no relevant differences are noticeable between samples treated with composites at 5 wt% and 30 wt% of CMC. The enhancement of E_f is visible only for samples treated with PB72 filled composites and it is significant just for walnut. In fact, if fir samples consolidated with microcomposites register an E_f increase of about 7%, decayed walnut samples treated with PB72 filled formulations present E_f values around 20% higher than that of samples treated with the neat resin. The maximum stress values of walnut samples consolidated with PB72/CMC composites solutions are about 20% higher than the experimental $\sigma_{MAX,f}$ values of samples treated with the unfilled PB72. While for fir samples no significant effect of CMC on this property can be detected.

4.3.3.2   *Charpy impact tests*

In Table IV-24 the values of total specific fracture energy U_{TOT}, specific energy for crack initiation U_i, specific energy for crack propagation U_p, and the ductility index DI, are summarized for each group of walnut and fir samples. The most important results from Charpy impact tests are showed in Figure IV-71(a-b) for walnut and IV-72(a-b) for fir.

Table IV- 24. Charpy tests results of undamaged and damaged walnut and fir wood samples before and after consolidation with neat PB72 and corresponding composites.

Sample	U_{TOT} $(kJ \cdot m^{-2})$	U_i $(kJ \cdot m^{-2})$	U_p $(kJ \cdot m^{-2})$	DI
walnut				
UW	20.86 ± 0.82	15.94 ± 0.66	4.92 ± 1.20	0.31 ± 0.05
DW	6.83 ± 0.60	3.50 ± 0.89	3.33 ± 0.70	0.95 ± 0.17
DW-T0	8.26 ± 0.89	4.33 ± 0.57	3.93 ± 0.45	0.91 ± 0.20
DW-T5	9.91 ± 0.80	6.11 ± 0.912	3.79 ± 0.52	0.62 ± 0.13
DW-T30	9.45 ± 0.57	6.13 ± 0.45	3.32 ± 0.33	0.54 ± 0.15
fir				
UW	12.95 ± 0.58	7.55 ± 0.94	5.40 ± 1.40	0.72 ± 0.22
DW	5.79 ± 0.80	4.09 ± 0.39	1.71 ± 0.54	0.42 ± 0.11
DW-T0	7.97 ± 0.83	5.32 ± 0.73	2.65 ± 0.88	0.50 ± 0.17
DW-T5	10.21 ± 0.54	6.24 ± 0.53	3.97 ± 0.52	0.64 ± 0.15
DW-T30	9.84 ± 0.87	6.03 ± 0.42	3.23 ± 0.57	0.54 ± 0.18

(a)

(b)
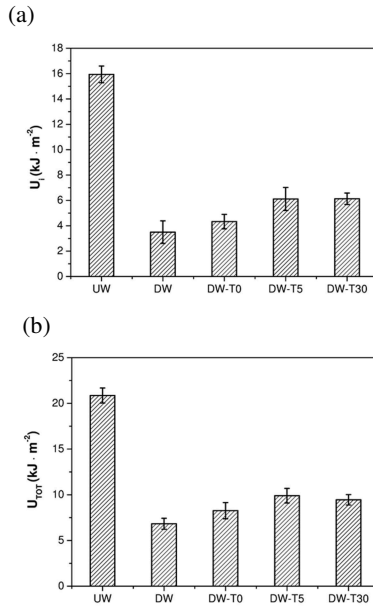
Figure IV- 71. Main impact flexural properties of undamaged and damaged walnut wood samples untreated and treated with neat Paraloid and CMC composites. (a) Specific energy adsorbed at the crack initiation, U_i, (b) total specific absorbed energy, U_{TOT}.

(a)

(b)
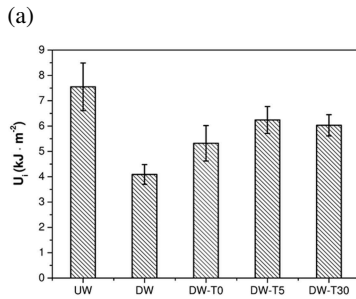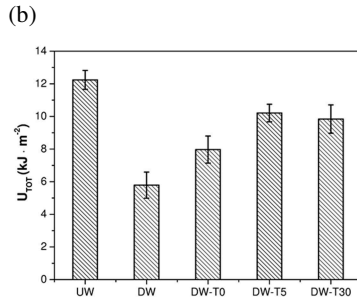
Figure IV- 72. Main impact flexural properties of undamaged and damaged fir wood samples untreated and treated with neat Paraloid and CMC composites. (a) Specific energy adsorbed at the crack initiation, U_i, (b) total specific absorbed energy, U_{TOT}.

These results highlight how impact strength values of historical damaged wood samples are much lower than their corresponding modern intact wood ones, with a drop in the main impact properties of about 70% for walnut and about 50% for fir. Moreover, if degraded fir registers a decrease of the ductility index, the DI value of worm-eaten walnut is much higher than that one of intact walnut, probably because of larval holes and galleries which modify the crack propagation path. Even under impact conditions, the consolidation with the neat matrix improves the flexural strength of the two wood species, with the increase of both U_i and U_{TOT}. Interestingly, all degraded wood samples treated with CMC composites exhibit higher values of U_i and U_{TOT} in comparison to wood consolidated with neat PB72. The best results are obtained by samples consolidated through the formulation with 5wt% of CMC. Walnut and fir samples treated with the neat PB72 register a higher value of the energy absorbed during the damage propagation and a similar value of the ductility index in comparison to the corresponding untreated samples. This could be explained with the presence of a transparent and ductile film on the surface of treated woods made by

PB72. Walnut samples consolidated with microcomposites report a progressive reduction of the U_p and, therefore, a decrease of DI as the CMC amount increases, evidencing how microcellulose can better fill the decay defects in these materials reducing the path of crack. While for fir samples consolidated with filled formulations an increase of both U_p and DI is detected, probably due to the surface nature of all treatments that being not able to penetrate, make only a ductile film on wood.

4.3.3.3 ShoreD hardness tests

In the following table the results from ShoreD hardness tests on each group of examined wood are collected.

Table IV- 25. Radial and tangential hardness values of undamaged and damaged walnut and fir wood samples before and after consolidation with neat PB72 and corresponding composites.

Sample	H_r	H_t
walnut		
UW	69.25 ± 0.63	63.51 ± 0.17
DW	65.56 ± 0.81	62.78 ± 0.64
DW-T0	65.70 ± 0.70	62.88 ± 0.80
DW-T5	67.44 ± 0.59	64.33 ± 0.79
DW-T30	69.03 ± 0.46	67.70 ± 0.42
fir		
UW	42.02 ± 0.59	45.65 ± 0.76
DW	35.54 ± 0.80	37.69 ± 0.86
DW-T0	39.28 ± 0.45	41.83 ± 0.76
DW-T5	39.13 ± 0.65	42.25 ± 0.75
DW-T30	39.09 ± 0.43	41.82 ± 0.60

Even the surface hardness of damaged walnut and fir woods is affected by the decay process. Both radial and tangential hardness values of the two historical wood types are lower than H_r and H_t of their corresponding modern intact wood. As one can see in Table IV-25, a positive effect of the CMC presence within Paraloid and, especially, its surface deposit on wood, is the improvement of H_r and H_t hardness values of treated decayed walnut wood which are progressively higher than those registered by wood samples treated with neat PB72. For fir it is not possible to notice any relevant difference between samples consolidated by the neat matrix and those treated with CMC composites.

4.3.3.4 Microstructural analysis

In order to assess if CMC flakes modify the fracture mode of treated wood, microstructural analysis of failure surfaces of impact tested walnut and fir samples were carried out. In Figure IV-73(a-e) and IV-74(a-e) it is possible to observe the 3D profiles of cross-sections of each group of walnut and fir, respectively, after impact failure.

(a)   (b)

(c)   (d)

(e)
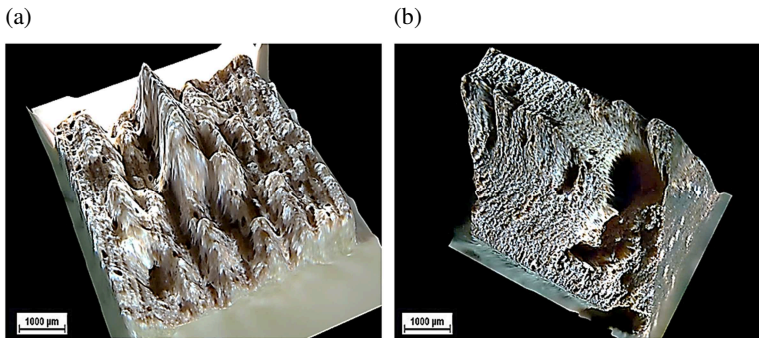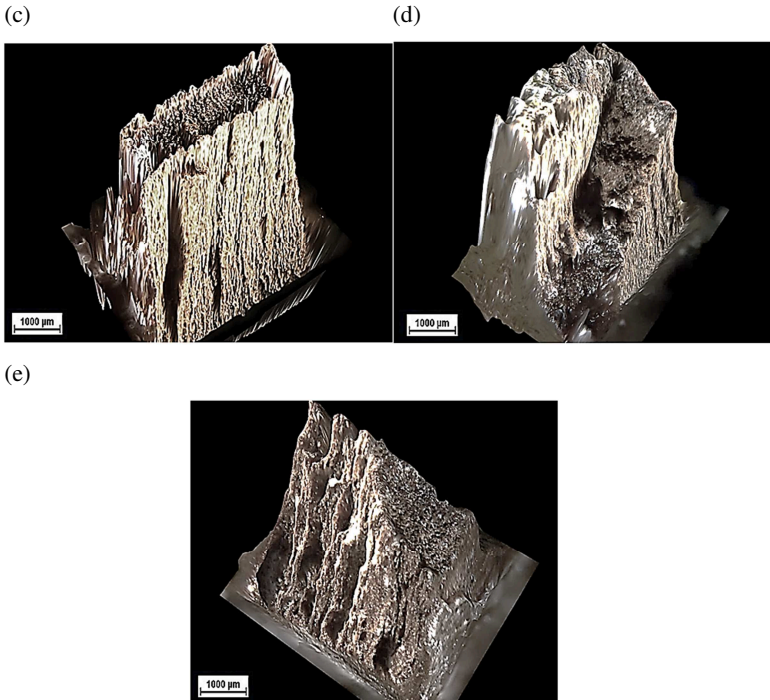
Figure IV- 73. 3D profiles of impact fracture cross-sections of undamaged (a) and damaged walnut wood samples untreated (b) and treated with neat Paraloid (c) and microcomposites with 5 wt% and 30 wt% of CMC (d-e).

(a)

(b)

(c)

(d)

(e)
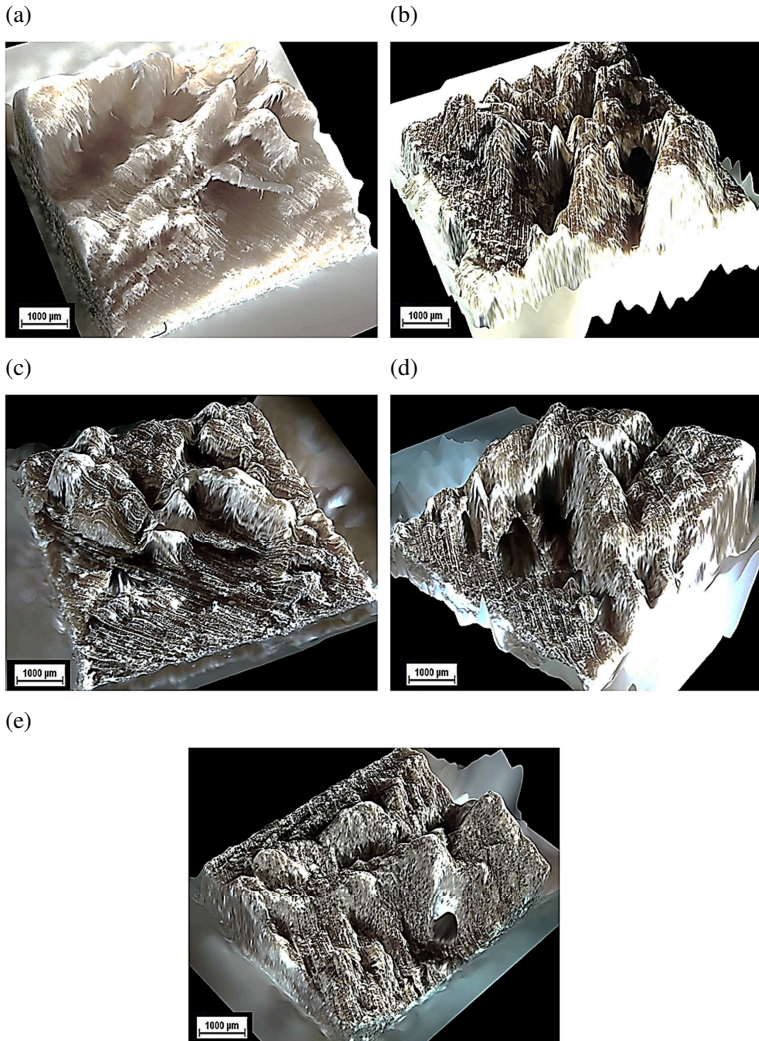
Figure IV- 74. 3D profiles of impact fracture cross-sections of undamaged (a) and damaged fir wood samples untreated (b) and treated with neat Paraloid (c) and microcomposites with 5 wt% and 30 wt% of CMC (d-e).

It is evident that all consolidants do not change the fracture behavior of the two decayed wood species. However, the images of walnut samples (Figure IV-73(a-b) show how defects made by larvae worms in the samples completely change the fracture mode of walnut passing from a brittle clean break to a cross-grain one [136]. It is also interesting to notice the inner walls of worm tunnels with the wooden matter totally degraded and, in case of treated samples, the deposit of the neat matrix or of polymer and microfiller together.

4.4   Lining of oil paintings on canvas

A degraded canvas has to recover its initial tension and mechanical properties and to do this conservators have to consolidate the original support by a lining work. The lining of canvas requires to the adhesive to be applied good viscoelastic and creep strength and relaxation resistance. Therefore, for this specific application an improvement of the adhesive joint dimensional stability is highly desirable, especially in cases of hygroscopic polymers as Aquazol resins. In the light of promising results obtained by Aquazol polymers after the introduction of CMC, melt-compounded thin films of neat Aquazol 200 and 500 and their resulting microcomposites with 5 wt% and 30 wt% of CMC and an average thickness of 100 μm were applied as lining adhesives keeping connected two canvases: an English linen representing the original oil painting substrate and a woven polyester usually utilized as lining textile.

4.4.1   Rheological tests

An important parameter to be considered for a successful lining work of oil paintings is the product penetration into the canvas. This property is strictly

related to the viscosity of the resin. Rheological tests were conducted on conditioned samples (T= 23°C and RH= 55%) at a temperature of 60 °C, the same environmental conditions and temperature used for the lining cycle, in order to assess the possible effect of CMC introduction on the viscosity of neat matrices. Figure IV-75(a-b) reports apparent viscosity curves of CMC composites tested at 60°C (i.e. the temperature of adhesive joints production).

(a)   (b)
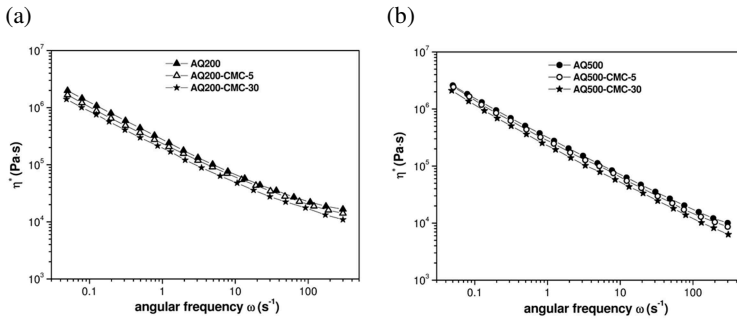
Figure IV- 75. Apparent viscosity curves of neat matrices and corresponding CMC composites. a) Aquazol 200 b) Aquazol 500.

A similar solid-like behavior is detected for all examined formulations. Rheological curves of Aquazol/CMC composites even at the highest CMC amount maintain the same viscosity value of neat matrices. The addition of CMC does not change the viscosity of AQ200 and 500 and therefore does not impair the good penetration degree of these products.

4.4.2   Single-lap shear tests

Single-lap shear tests in quasi-static and creep configuration were performed on canvas samples lined by thin Aquazol/CMC films. In Table IV-26 the

shear strength (τ_B) and joint displacement (u) values from single lap shear tests are collected. In Figure IV-76(a-b) adhesive displacement curves of filled and unfilled Aquazol 200 and 500 are presented.

Table IV- 26. Results of single-lap shear tests under quasi-static and creep condition on neat matrices and resulting CMC composites.

Sample	τ_B (MPa)	u at t= 3600s (mm)
AQ200	1.04 ± 0.02	22.90 ± 0.03
AQ200-CMC-5	1.26 ± 0.02	14.33 ± 0.03
AQ200-CMC-30	1.17 ± 0.01	11.90 ± 0.02
AQ500	1.76 ± 0.01	24.29 ± 0.05
AQ500-CMC-5	1.87 ± 0.01	15.25 ± 0.02
AQ500-CMC-30	1.70 ± 0.02	13.35 ± 0.03

(a) (b)
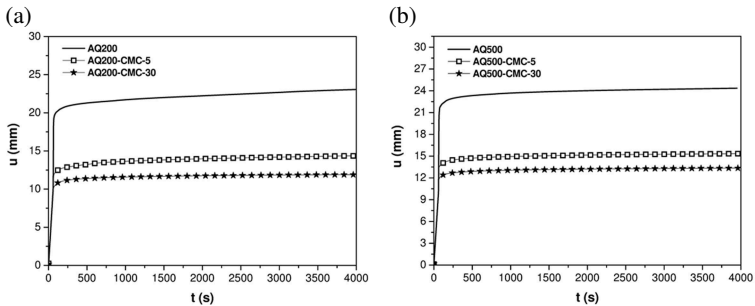
Figure IV- 76. Displacement curves from single-lap shear tests under creep condition on adhesive joints based on CMC polymer composites. a) neat AQ200 and resulting composites, b) neat AQ500 and resulting composites.

The results show that the introduction of CMC particles into AQ200 and AQ500 leads to an increase of τ_B for formulations with 5 wt% of this microfiller and also with 30 wt% for AQ200. Adhesive joints of AQ500 with the highest CMC content manifest a value of τ_B close to that of the neat matrix. As previously seen (section 4.1.3) also during the application it is possible to appreciate the synergistic effect of moisture content and CMC on these materials. The higher percentage of water in samples with 5 wt% of CMC in comparison to pure polymers could be the cause of the τ_B increment, while, in composites with 30 wt% of CMC, the filler action is predominant, but the presence of moisture limits the τ_B loss. The values of joint displacement u, prove the higher creep stability upon a constant stress of filled adhesive joints in comparison to the corresponding neat matrices. In fact, the u values of filled AQ200 and AQ500 are progressive lower than those of unfilled polymers, especially for long time of testing. In Figure IV-77(a-b) relative τ_B and u trends (i.e. normalized over the value corresponding to neat polymer matrices) as a function of the CMC loading are shown.

(a)   (b)
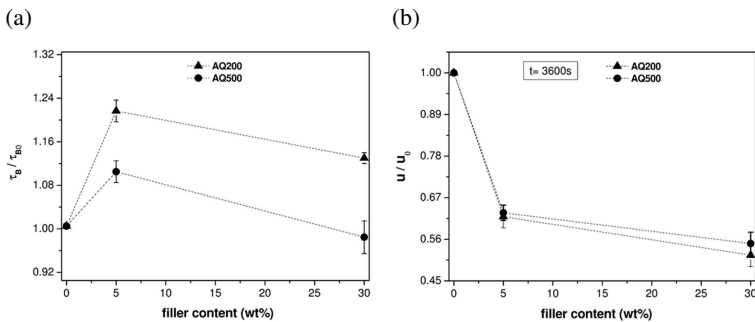
Figure IV- 77. Relative single-lap shear properties trends of neat matrices and resulting CMC composites. (a) Shear strength τ_B, (b) displacement u, at 3600 s.

From the relative τ_B trends of the two Aquazol it is possible to observe the slight increase of the adhesive strength more visible for AQ200 samples. The progressive reduction of u is similar for the two polyamides. In particular, a CMC addition of 30 wt% is able to promote a decrease of joint displacement of about 50% in comparison to neat matrices.

4.4.3   Microstructural analysis

Since the introduction of a reinforcing agent in adhesive systems could impair their fracture behavior, optical microscope observations of the fracture surfaces of Aquazol based microcomposites were performed. Figure IV-78(a-b) presents the two cross-sections of each joint (the neat polymers and their corresponding composites) after fracture, with the English linen canvas in the upper part of the samples and the woven polyester in the bottom parts.

(a)
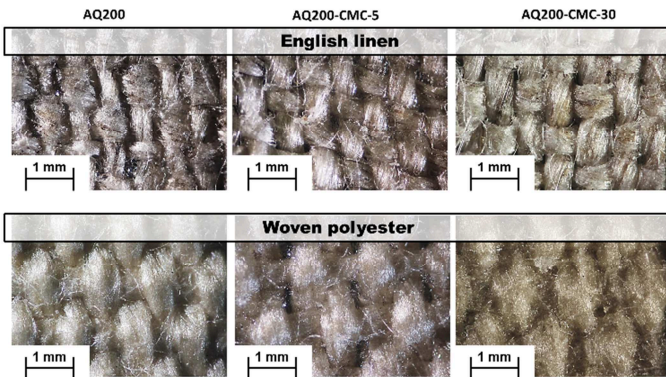
(b)
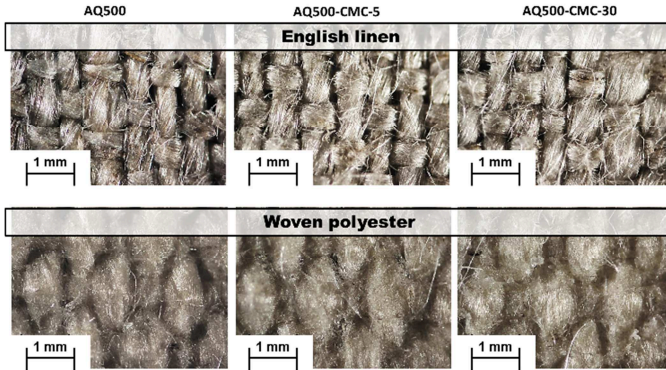
Figure IV- 78. Optical microscope images of overlap adhesive area of CMC composites. a) neat AQ200 and resulting composites, b) neat AQ500 and resulting composites.

The images show that all formulations, even with the highest amount of CMC, manifest the same fracture mode of neat matrices, i.e. an adhesive fracture. In fact, the adhesive joints fail at the linen/glue interface and the main part of the adhesive layers remain on the woven polyester. This could be explained through a different penetration degree of adhesive films into the two kinds of canvas due to a difference in the inter-yarn porosity of the two selected textiles. The woven polyester has a lower inter-yarn porosity in comparison to the linen canvas and maybe this affects the penetration of adhesive films, allowing a higher penetration of these materials into the lining textile.

4.4.4 Comparison between micro- and nano adhesives composites performances

Considering the relevant increase of the dimensional stability imparted by CNC particles to Aquazol 500, thin films of this polymer filled with 5, 10 and 30 wt% of CNC having an average thickness of 250 μm were applied as lining adhesives of canvas. The same types of substrates and the same tests already seen for melt-compounded CMC films were utilized. In order to investigate the action of a micro- and a nanoscale cellulose on the mechanical performance of AQ500 adhesive, the same tests were carried out on adhesive joints made by CMC thin films produced through the solution mixing method. In this way it was possible to verify if the positive stabilization of the matrix promoted by CMCs and CNCs is also active during the application of this polymer as canvas consolidant/adhesive.

4.4.4.1 Single-lap shear tests

Single-lap shear tests in quasi-static and creep configuration were performed on canvas samples lined by thin CMC and CNC films obtained by solvent casting process. The adhesive strength (τ_B) and the joint displacement (u) values of the neat matrix and the relative micro- and nanocomposites are listed in Table IV-27. In Figure IV-79(a-b) adhesive displacement curves of Aquazol 500 filled with CMC and CNC are represented.

Table IV- 27. Results of single-lap shear tests under quasi-static and creep condition on neat Aquazol 500 and resulting CMC and CNC composites.

Sample	τ_B (MPa)	u at t= 3600s (mm)
AQ500	2.87 ± 0.02	19.71 ± 0.03
AQ500-CMC-5	2.51 ± 0.01	15.68 ± 0.03
AQ500-CMC-10	2.47 ± 0.02	14.15 ± 0.02
AQ500-CMC-30	1.30 ± 0.04	--
AQ500-CNC-5	2.70 ± 0.02	11.13 ± 0.02
AQ500-CNC-10	2.63 ± 0.05	9.11 ± 0.02
AQ500-CNC-30	2.00 ± 0.02	7.29 ± 0.04

(a)   (b)
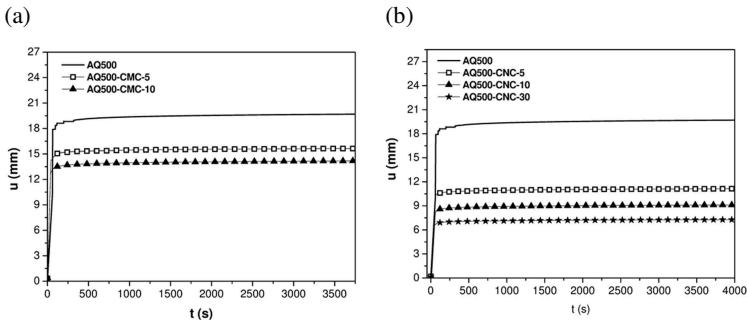
Figure IV- 79. Displacement curves from single-lap shear tests under creep condition on adhesive joints of Aquazol 500 and (a-b) CMC and CNC composites.

Cellulose micro and nanocrystals lead to a decrease of the adhesive strength of AQ500 proportionally to the filler loading. If for CMC filled adhesive joints this fall in τ_B is significant since the lowest amount of this microfiller, the negative effect of CNC on the τ_B of AQ500 becomes relevant in samples with the highest filler content. On the other hand, a relevant increase of the

dimensional stability for all adhesive joints, and, in particular, for those filled with CNC, with a systematic reduction of the adhesive displacement u, is detected since the lowest amount of fillers. It was not possible to perform single-lap shear tests under creep condition on microcomposites at 30 wt% of CMC since they failed during tests, being the shear stress used for these tests (τ_0 = 50% of the AQ500 τ_B value) too high for them. The direct comparison of relative τ_B trends (i.e. normalized over the value corresponding to the neat matrix) as a function of the filler loading (Figure IV-80a) shows that CMC composites register the most important adhesive strength loss, with a decrease of τ_B for the formulations with the highest filler amount of around 60% in comparison to the unfilled matrix. While CNC composites at 30 wt% of filler reach a τ_B value about 30% lower than that of the neat AQ500. From relative u trends (Figure IV-80b) one can notice that microcomposites report an elongation reduction up to about 30% for formulations with 10 wt% of CMC, against joints filled with CNC suspensions that reach u values up to 60% lower than the neat matrix.

(a)   (b)
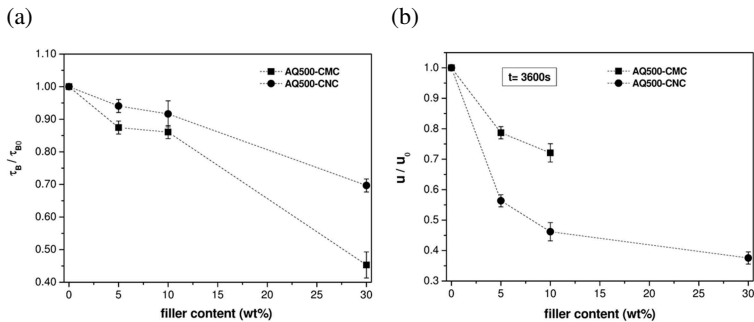
Figure IV- 80. Relative single-lap shear properties trends of neat Aquazol 500 and resulting CMC and CNC composites. (a) Shear strength τ_B, (b) displacement u, at 3600 s.

In conclusion the comparison between micro- and nano-adhesive films performances highlights how the stabilization action of CNC on AQ500 is

much stronger and more powerful than that produces by CMC. CNC particles are responsible of a more limited decrease of the adhesive strength and a higher creep resistance since the lowest amount of filler with respect to CMC.

4.4.4.2 Microstructural analysis

Figure IV-81(a-b) represents the two cross-sections of each joint (the neat polymer and its corresponding CMC and CNC composites) after fracture, with the English linen canvas in the upper part of the samples and the woven polyester in the bottom parts.

(a)
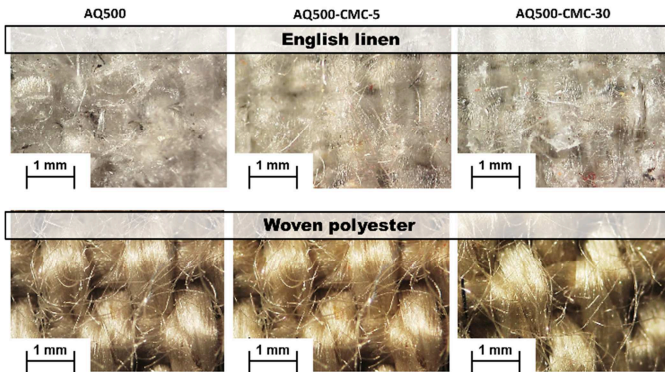
(b)
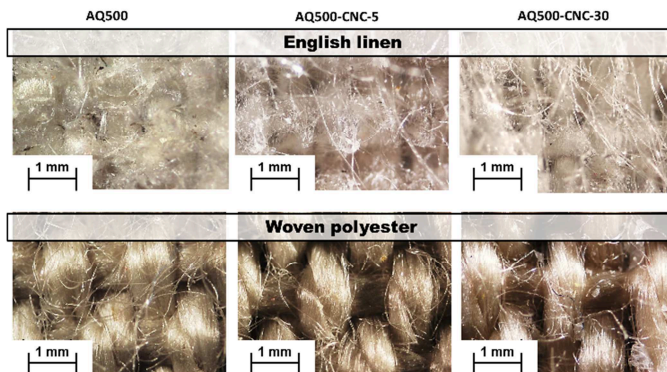
Figure IV- 81. Optical microscope images of overlap adhesive area of (a) CMC composites and (b) CNC composites.

All adhesive joints, even with the highest amounts of micro- and nanocellulose, manifest the same fracture mode of the neat matrix, i.e. an adhesive fracture. In fact, all adhesive films fail at the polyester/glue interface and the main part of the adhesive layers remain on the English canvas. This could be due to the effect of the solvent used in the films production and at the same time a probable higher hygroscopicity of linen textile with respect to the synthetic polyester that allows a better penetration of adhesive films into the English canvas.

Chapter V
Conclusions and Future perspectives

Conclusions of the microcomposites characterization

Various amounts of cellulose microcrystals (CMC, 5÷30 wt%) were melt compounded and compression molded with three commercial artwork preserve resins: a MA/EMA acrylate copolymer (Paraloid B72) and two molecular weights of a poly 2-ethyl-2-oxazoline homopolymer (Aquazol 200 and 500) to prepare innovative thermoplastic composites for cultural heritage restoration. In order to assess the effect of this microfiller on the physical and thermo-mechanical behavior of the resulting materials an extended characterization was performed. A comparison between dried and conditioned samples was carried out in order to evaluate also the combined action of CMC and water uptake under recommended hydrothermal conditions for artworks conservation (T= 23°C, RH= 55%).

- ESEM observations showed a uniform dispersion within the three matrices of CMC without any preferential orientation and filler aggregation. Only for PB72 matrix an enhancement of the glass

transition temperature since the lowest amount of CMC was detected. TGA tests revealed that CMC increased the thermal stability of all polymers except AQ200/500 with the highest amount of CMC.

- The water diffusion through the filler/matrix interface led to an increase of the equilibrium moisture content for all composites with respect to neat matrices. A transparency decrease proportional to the filler content and a chromatic change of these materials filled with the highest amount of CMC towards yellow tones were observed.

- Despite the increase of moisture content, CMC addition produced an interesting stabilizing effect on both dried and conditioned matrices with an increase of the dynamic storage and loss moduli, more pronounced for wet samples, and a decrease of the thermal expansion coefficient as the filler loading increases. Moreover, CMC introduction in conditioned formulations determined a remarkable increment of the stiffness associated to an enhancement of the tensile properties at break, in contrast to the mechanical behavior of dried microcomposites that reported a drop in these properties. Both dried and wet formulations highlighted a similar stabilizing effect induced by CMC flakes even under constant long-lasting (creep) stresses, regardless of the moisture content. Therefore, CMC has a predominant role on the mechanical response of these polymers over the action of absorbed water. This is important especially for Aquazol polymers which have a very high tendency to water sorption.

Conclusions of the nanocomposites characterization

The physical and thermo-mechanical behavior of thin films obtained by the solution mixing method and made of a thermoplastic artwork adhesive Aquazol 500 (a poly 2-ethyl-2-oxazoline homopolymer), and different amounts of cellulose nanocrystals (CNC, 5÷30 wt%) were investigated. The comparison with microcomposites obtained from the same matrix filled with cellulose microcrystals, CMC, was performed, in order to assess the different effect of a micro- and nanoscale filler on this polymeric matrix.

- FESEM analysis evidenced a homogenous dispersion of both CMC and CNC particles without any filler aggregation. For microcomposites with the highest amount of CMC a deposit phenomenon of this filler was observed. Only CNC was able to improve the glass transition temperature of the pure polymer but for formulations with the highest amount of this nanofiller a more relevant decrease of the thermal stability with respect to microcomposites was detected.

- All nanocomposites preserved their high transparency even at highest amounts of CNC, while CMC flakes impaired the optical features of the neat matrix with increasing of the filler content.

- Interestingly, CNC is more powerful than CMC in the increase of the dynamic moduli and the decrease of the thermal expansion coefficient as the filler loading increases. This stabilizing action of CNC was observed also during creep tests with a progressive and much higher reduction of the AQ500 creep elongation with respect to microcomposites.

Conclusions of the application of Paraloid based microcomposites as consolidant of wood

A physic-mechanical investigation of the effect of 5 and 30 wt% of CMC on the consolidating properties of Paraloid B72 was conducted. Historical walnut (Juglans regia) and fir (Abies alba) wood samples were treated with neat and filled Paraloid solutions in acetone. These two types of wood exhibited a critical biological degradation more pronounced for walnut samples, with an increase of the pore radius and a dramatic drop of their mechanical properties due to the holes and tunnels made by larval worms.

- CMC introduction did not change the good viscosity of the neat matrix and especially its good water repellency. In fact, for all treated wood samples a similar reduction of the moisture content and the volumetric swelling was observed. Wood samples treated with PB72/CMC composites showed a progressive decrease of the pore radius.

- From optical microscope images and FTIR analysis it was possible to observe how PB72 and CMC flakes were able to create a surface transparent film on all consolidated samples and penetrate in the inner of treated damaged woods filling worm-larvae holes and galleries. Only for wood samples treated with the highest amount of CMC was possible to notice a white exterior deposit of this filler on the surface.

- The presence of CMC within PB72 allowed the improvement of the stiffness and the flexure strength of consolidated woods under quasi-static and impact conditions, with the flexural modulus, the maximum flexural stress and both initial and total impact absorbed energies increased with filler loading. Moreover, a systematic

increment of the radial and tangential surface hardness almost up to the intact wood values was observed on treated walnut wood samples.

Conclusions of the application of Aquazol based micro- and nanocomposites as lining adhesives of canvas

Melt-compounded thin films of AQ200 and 500 filled with 5 wt% and 30 wt% of CMC and solution mixed AQ500 micro- and nanocomposites with 5, 10 and 30 wt% of CMC and CNC, respectively, were applied as adhesives connecting two kinds of canvas in order to simulate the restoration of oil paintings by a lining work. Thanks to single-lap shear tests it was possible to verify the increase of the dimensional stability of Aquazol resins due to the CMC and CNC introduction already seen in the preliminary characterization of these experimental formulations.

- Mechanical tests confirmed the stabilization provided by the addition of CMC on the melt-compounded Aquazol matrices, with an important reduction up to 50% of the adhesive joint elongation. It is assumed that the higher amount of moisture within filled samples led to an increase of the adhesive strength.
- CMC solution mixed composites reported a dramatic drop in the adhesive strength since the lowest amount of filler. CNC films showed a relevant decrease of this property just at the highest filler content, but a more pronounced reduction of the adhesive displacement (around 60%) was detected since the lowest loading of this filler.

Considering the promising results obtained from micro- and nanocomposites could be interesting to extend the application of CMC and, especially, CNC composites in other restoration operations, testing also different polymeric matrices. For this purpose, cellulose nanocrystals were produced starting from CMC flakes by means of the sulfuric acid hydrolysis (see section 6.1).

Chapter VI
Collateral research activities

6.1   Cellulose nanocrystals production

The objective of this work was to find a rapid and high-yield process to obtain an aqueous stable colloid suspension of cellulose nanocrystals (CNC). In this section the experimental procedure for the production of CNC starting from cellulose microcrystals (CMC) powder is described. The preliminary results of the morphology characterization of these obtained CNC particles are presented. The final goal is the production of cellulose nanocrystals with a milder process with respect to standard methods present in literature and an aspect ratio close to that of CNCs already used in this research kindly supplied by the Wallenberg Wood Science Center (Sweden).

6.1.1   Samples preparation

CNCs were separated from CMC powder (specific gravity=1.56 g·cm^{-3}, mean molecular weight= 90000 g/mol), supplied by Sigma Aldrich (USA).

CMC particles consist of elongated flakes with an average length of about 24 μm and a diameter of about 10 μm (average L/D ratio of 2.4) (Figure III-3). The cellulose nanoparticles were isolated from CMC by sulfuric acid hydrolysis, following the procedure described by Bondeson et al. [94, 137] with some modifications.

CMC was mixed with deionized water. The water/CMC suspension was then put in an ice bath and stirred while concentrated sulfuric acid (Sigma Aldrich) was added by drop until the desired acid concentration was reached. A concentration of CMC of 10 g/100mL of acid and an acid concentration of 64% (w/w) were utilized. The suspension was heated while stirred till a temperature of 44 °C was achieved. The suggested treatment time was of 2h. In this work two acid treatment times were selected: 1h and 2h, in order to check the difference in the size of CNC particles after the two different treatments and try to get a milder cycle of production with good particles size results. The suspension was then washed with deionized water using repeated centrifuge cycles of 30 min at 3500 rpm. The supernatant was removed from the sediment and replaced by new deionized water and mixed. Centrifuge cycles were stopped until the supernatant became turbid. The final step was the dialysis with deionized water until the reaching of a neutral constant pH (around 6-7). The total preparation procedure is illustrated in Figure VI-1.
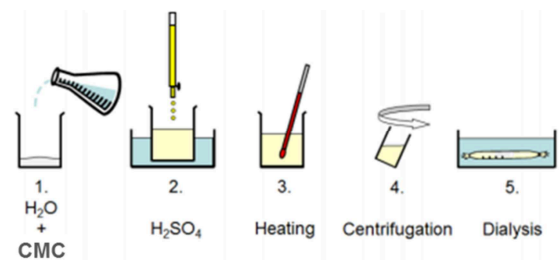
Figure VI- 1. Preparation procedure for cellulose nanocrystals [137].

In Figure VI-2 a picture of the two aqueous suspensions of CNC obtained through an acid hydrolysis time of 1h and 2h is reported.

Figure VI- 2. Image of aqueous suspensions of CNC after a sulfuric acid hydrolysis time of 1h and 2h.

6.1.2 TEM analysis

The morphological characteristics of CNC particles made by 1h and 2h of acid treatment were obtained from a Philips® EM 400 T (Amsterdam, Netherlands) transmission electronic microscope at an acceleration voltage of 120 kV. A drop of diluted suspensions (0.0016% w/v in water) was placed on a copper grid and allowed the air-drying for 24h. TEM micrographs of CNCs after 1h and 2h of sulfuric acid hydrolysis are depicted in Figure VI-3(a-d) and Figure VI-4(a-d), respectively.

(a) (b)

(c) (d)
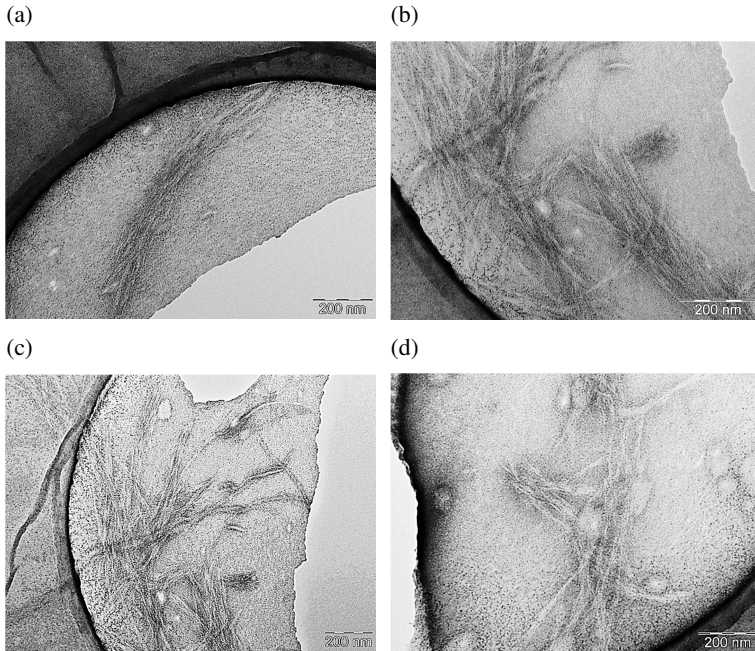
Figure VI- 3. TEM images of CNCs after 1h of acid treatment (a-d).

(a)

(b)

(c)

(d)
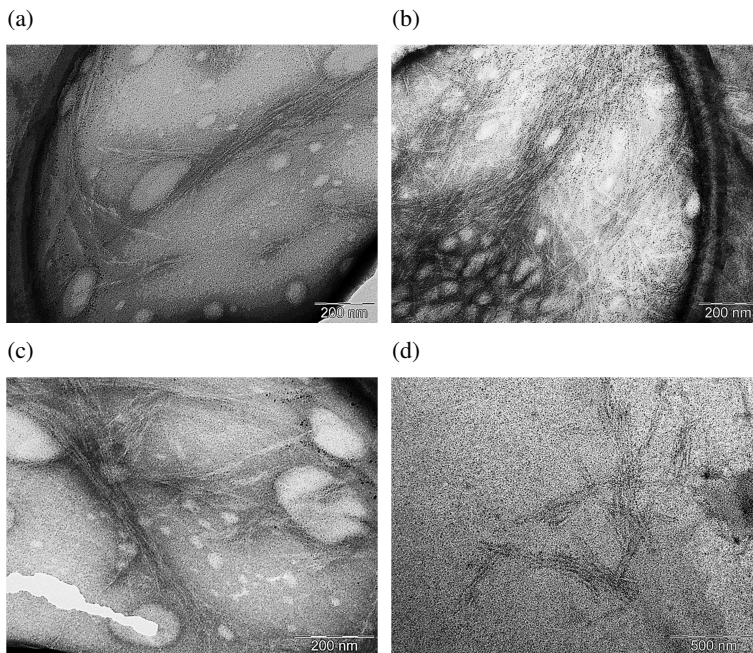
Figure VI- 4. TEM images of CNCs after 2h of acid treatment (a-d).

Comparing the two set of TEM micrographs it is possible to see that CNCs obtained with half of the suggested time of CMC acid hydrolysis result visible thicker than those treated for 2h with sulfuric acid. Since it is hard to quantify the size of these particles by an image analysis software because of their low resolution, it could be convenient to negatively stain the samples before observation in order to increase the contrast of images, as reported in literature [138-140].

6.2 Determination of the polymerization degree of cellulose-based textiles

The textiles utilized as substrates of ancient oil paintings are obtained from the processing and the weaving of natural fibers, such as linen and cotton. These fibers are made up cellulose. The cellulose polymer consists of linear chains of β-D-glucose monomers. These units can reach a number of 2500-3000 in the most common raw fibers. This number is defined degree of polymerization (DP). Degradative reactions due to various factors as light, heat, chemical agents, pollutions and biological organisms can decrease the DP of cellulose fibers. In presence of decay processes the length of polymer chains is downsized because of the splitting of β-D-glucose bonds and this leads to a consequent mechanical properties loss [141]. In particular, the DP is direct correlated to the tenacity of canvas yarns. The polymerization degree of cellulose can be determined through its intrinsic viscosity in solution using a capillary viscometer. The assessment of the DP of ancient damaged canvas samples taken from an oil painting (18th century) under restoration was performed in order to determine a representative conservation state of oil paintings substrates. This is a very important information for conservators, because it gives them an idea about the optimal restoration approach to select, especially when it is necessary to make a choice of lining.

6.2.1   Samples preparation

In Figure VI-5(a-b) the two kinds of canvas examined in this work are shown.
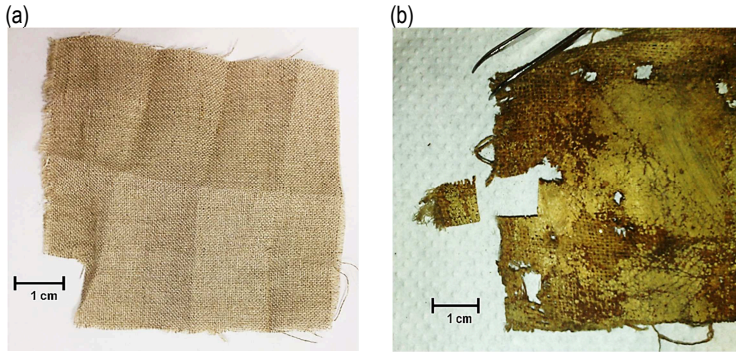
Figure VI- 5. Samples of linen canvas for viscosimetry measurements. (a) Modern intact canvas, (b) ancient damaged canvas.

On the surface of the ancient canvas sample a layer of imprimitura is present. An oil painting is made up several layers. As one can see in Figure VI-6, the schematic of an oil painting section shows the canvas that is the substrate (named ground) at the bottom of the artwork, the imprimitura coming after, the following paint film and at the end the varnish layer.

Figure VI- 6. Schematic of an oil painting section.

The imprimitura is an intermediate layer between the ground and the paint layers also called priming layer which was made of oils and/or resins or proteinaceous binders and fillers [142]. It acts as a compact base for fixing pigments, colors and media and reducing the absorbency of the ground layer. Since this coating could make harder the dissolution of canvas for viscosity tests, it was necessary to identify its chemical composition to remove it. The traditional priming layer of oil paintings was made up basic lead carbonate called "biacca" and linseed oils. The ESEM-EDS analysis of this priming coating was conducted using a Philips XL30 environmental scanning electron microscope equipped with an EDAX light-element energy-dispersive spectroscopy detector. In Figure VI-7(a-b) the ESEM image of analyzed coating area and the collected EDS spectrum and quantitative results are reported.

(a)

(b)

Element	Wt %	At %	K-Ratio	Z	A	F
NaK	0.82	4.39	0.0025	1.2401	0.2433	1.0003
MgK	1.08	5.47	0.0044	1.2696	0.3249	1.0004
AlK	0.86	3.94	0.0045	1.2306	0.4212	1.0006
SiK	1.59	7.00	0.0106	1.2647	0.5242	1.0004
K K	0.81	2.55	0.0054	1.2426	0.5322	1.0032
CaK	6.59	20.31	0.0490	1.2628	0.5881	1.0003
FeK	2.30	5.09	0.0242	1.1876	0.8722	1.0122
PbL	85.95	51.24	0.7955	0.9228	1.0030	1.0000
Total	100.00	100.00				
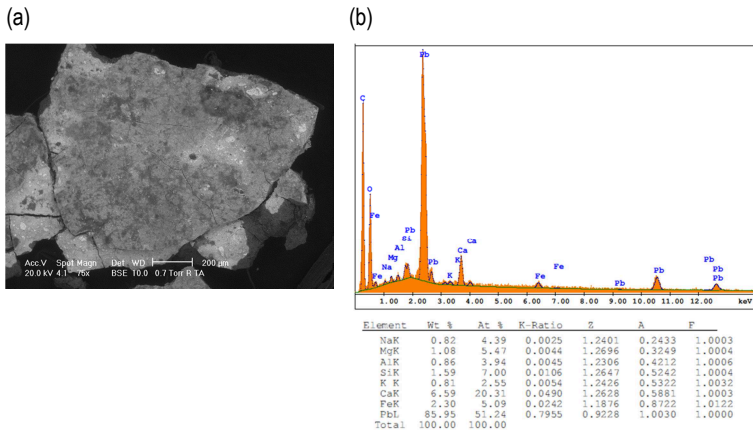
Figure VI- 7. (a) ESEM image of the examined priming layer area and (b) collected EDS results.

The ESEM-EDS analysis confirm that the main constituent of the examined layer is lead. Additionally, FTIR analysis of the coating was carried out by a FTIR spectrometer Varian 4100 (Excalibur Series) equipped with a Golden Gate diamond (Graseby Specac) for ATR analysis. In Figure VI-8 the FTIR spectra of uncoated and coated canvas are represented.
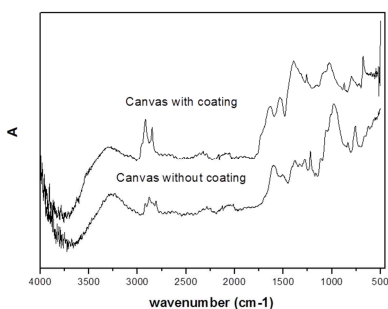
Figure VI- 8. FTIR spectra of canvas with and without the priming layer.

From these spectra one can identify the typical peaks of linseed oils: the stretching signal of C-H at around 3000 - 2800 cm^{-1} and the stretching peak of C=O visible at about 1700 cm^{-1} in the shoulder of the cellulose peak centered at around 1500 cm^{-1}. The typical peaks of biacca are also present at around 1450 cm^{-1} due to the bending of CH_2, at around 1150-1050 cm^{-1} and at 690 cm^{-1}. A buffer solution of acetic acid/sodium acetate at pH 5 in order to avoid an additional damage of the ancient canvas was utilized for the cleaning of the coating. ESEM-EDS analysis (Figure VI-9(a-b)) and optical microscope image (Figure VI-10(a-b)) of the ancient canvas samples after treatment evidence the almost complete removal of this layer.

(a)   (b)
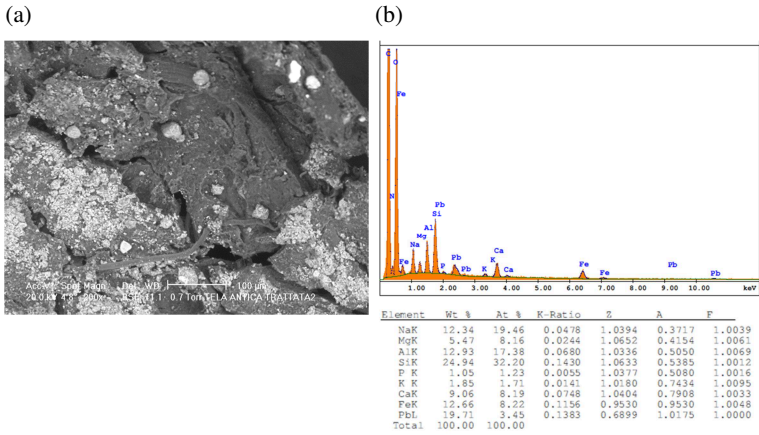
Figure VI- 9. (a) ESEM image of treated priming layer area and (b) collected EDS results.

(a)   (b)
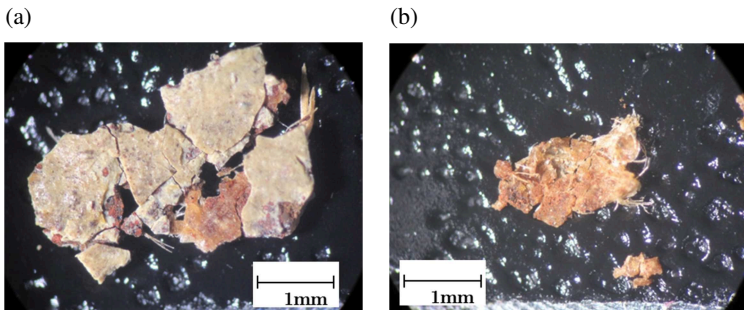
Figure VI- 10. Optical microscope images of ancient canvas (a) before and (b) after treatment of imprimitura removal.

6.2.2 Viscosity measurements

Viscosity measurements of ancient damaged linen canvas samples were conducted. The same tests were performed on corresponding modern intact canvas samples as terms of comparison. All samples were dissolved in cupriethylenediamine hydroxide 0.5 M with a final solution concentration of 0.1 g/dL. A magnetic stirring at 35 °C was used to allow the complete dissolution of textiles. The viscosity tests were performed through an Ubbelohde capillary viscometer type sI 22 at 25 °C. The intrinsic viscosity [η] values were calculated according to UNI 8282, ASTM D1795-96 and DIN EN ISO 1628-1 standards. The weight average polymerization degree of cellulose DP_W, was determined multiplying [η] for a factor of 1.5 according to the Mark–Houwink–Sakurada equation [143, 144]:

$$DP_W = K[\eta]^a$$

where K and a are experimental constants equal to 1.5 and 1, respectively.

At least five specimens for each kind of canvas were tested.

In Table VI-1 the [η] and DP_W values of ancient and modern canvases are listed.

Table VI- 1. Intrinsic viscosity [η] and weight average polymerization degree of cellulose DP_W values of ancient and modern linen canvases.

Sample	[η] (mL/g)	DP_W
Canvas		
Modern	1300	1950
Ancient	320	480

A dramatic drop in [η] and DP_W is evident for damaged canvas. In particular, [η] and DP_W values are 75% lower than those reported by modern intact linen, highlighting a critical conservation state of this textile. Moreover, these results are in accordance with literature studies, where oil paintings substrates from XVII-XVIII centuries registered DP_W values between 750 and 500 [145]. A so poor polymerization degree of canvas requires an incisive restoration operation as the lining work and/or the consolidation of the oil painting substrate.

References

1   C. F. Bria, *The History of the Use of Synthetic Consolidants and Lining Adhesives. WAAC Newsletter,* 1986. **8**.

2   J. S. Mills and R. White, *The Organic Chemistry of Museum Objects*, Butterworth, Oxford U.K. 1994.

3   C. V. Horie, *Materials for Conservation: Organic consolidants, Adhesives and Coatings* Butterworth-Heinemann, Oxford, U. K. 1987.

4   T. Van Oosten, Y. Shashoua and F. Waentig, *Plastics in ArtsHistory, Technology, Preservation*, Kölner Beiträge zur Restaurierung und Konservierung von Kunst- und Kulturgut Band 15, München, Germany 2002.

5   S. Spoljaric, A. Genovese and R. A. Shanks, *Polypropylene–microcrystalline cellulose composites with enhanced compatibility and properties. Composites Part A Applied Science and Manufacturing,* 2009. **40:**791-799.

6   J. P. F. Lagerwall, C. Schutz, M. Salajkova, J. Noh, J. Hyun Park, G. Scalia and L. Bergstrom, *Cellulose nanocrystal-based materials: from liquid crystal self-assembly and glass formation to multifunctional thin films. NPG Asia Mater,* 2014. **6:**e80.

7   M. Koller, Learning from the history of preventive conservation, in *IIC 1994 Ottawa Congress: Preventive Conservation - Practice, Theory and Research*, ed by A. Roy and P. Smith. Archetype Publications, London, 1994. pp. 1-7.

8   A. Conti, *A History of the Restoration and Conservation of Works of Art*, Butterworth-Heinemann 2007.

9   M. Abey-Koch, *History of housekeeping. In The National Trust manual of housekeeping. The care of collections in historic houses open to the public*, Elsevier Butterworth-Heinemann, Oxford, U.K. 2006.

10   L. Masschelen-Kleiner and F. Bergiers, Influence of adhesives on the conservation of textiles, in *Adhesives and consolidants: Contributions to the 1984 IIC Congress*, ed by B. e. al., Paris, pp. 70-73 (1984).

11   R. L. Feller, N. Stolow and E. H. Jones, *On picture varnishes and their solvents*, National Gallery of Art 1985.

12   E. May and M. Jones, *Conservation Science: Heritage Materials*, Royal Society of Chemistry 2006.

13 B. Appelbaum, *Conservation Treatment Methodology*, Butterworth-Heinemann 2007.

14 H. M. Szczepanowska, *Conservation of Cultural Heritage: Key Principles and Approaches*, Routledge 2013.

15 M. Matteini and A. Moles, *La chimica nel restauro: i materiali dell'arte pittorica*, Nardini 1989.

16 C. H. Thuer, *Scottish Renaissance Interiors: Facings and adhesives for size-tempera painted wood*. *Historic Scotland Technical Paper,* 2011.

17 M. a. G. Commision, *Science for Conservators: Adhesives and coatings*, Conservation Unit of the Museum and Gallery Commision 1987.

18 A. Unger, A. P. Schniewind and W. Unger, *Conservation of Wood Artifacts: A Handbook*, Springer 2001.

19 L. Toniolo, A. Paradisi, S. Goidanich and G. Pennati, *Mechanical behaviour of lime based mortars after surface consolidation*. *Construction and Building Materials,* 2011. **25:**1553-1559.

20 G. Borsoi, M. Tavares and R. V. António Santos Silva, Studies of the Performance of Nanostructured and other Compatible Consolidation Products for Historical Renders, in *Materials Science Forum*. Ana Maria Pires Pinto and António Sérgio Pouzada, pp. 942-947 (2012).

21 F. P. Laboratory, *Wood handbook: Wood as an engineering material*, Department of Agriculture, Washington, D.C, U.S. 1987.

22 R. Eaton and M. Hale, *Wood: Decay, Pests and Protection*, Chapman and Hall 1993.

23 Y. Wang and A. P. Schniewind, *Consolidation of deteriorated wood with soluble resins*. *Journal of the American Institute for Conservation,* 1985. **24:**77-91.

24 D. W. Grattan, Consolidants for degraded and damaged wood, in *Proceedings of the furniture and wooden objects symposium*. Canadian Conservation Institute, Ottawa, pp. 27–42 (1980).

25 R. Barclay, *Wood consolidation of an eighteenth century English fire engine*. *Studies in Conservation,* 1981. **26:**133-139.

26 M. Robson, Early advances in the use of acrylic resins for the conservation of antiquities, in *Polymers in conservation*, ed by N. S. Allen, M. Edge and C. V. Horie. Royal Society of Chemistry, Cambridge U. K., 1992. pp. 184.

27 T. H. Taylor, *In situ repair of architectural glass, Adhesives and consolidants*, International Institute for Conservation, London U.K. 1984.

28 G. G. Amoroso and V. Fassina, *Stone decay and conservation*, Elsevier, Amsterdam 1973.

29 M. Lazzari and O. Chiantore, *Thermal-ageing of paraloid acrylic protective polymers*. *Polymer,* 2000. **41:**6447-6455.

30   O. Chiantore and M. Lazzari, *Photo-oxidative stability of paraloid acrylic protective polymers. Polymer,* 2001. **42:**17-27.

31   D. Sale, Yellowing and Appearance of Conservation Adhesives for Poly(methyl methacrylate): A Reappraisal of 20-Year-Old Samples and Test Methods, in *Adhesives and Consolidants for Conservation* Ottawa, Canada (2011).

32   E. F. Hansen, M. R. Derrick, M. R. Schilling and R. Garcia, *The Effects of Solution Application on some Mechanical and Physical Properties of Thermoplastic Amorphous Polymers Used In Conservation: Poly(vinyl acetate)s. Journal of the American Institute for Conservation,* 1991. **30:**203-213.

33   S. Chapman and D. Mason, *Literature Review: The Use of Paraloid B-72 as a Surface Consolidant for Stained Glass. Journal of the American Institute for Conservation,* 2003. **42:**381-392.

34   J. L. Down, M. A. MacDonald, J. Tétreault and R. S. Williams, *Adhesive testing at the Canadian Conservation Institute: An evaluation of selected poly(vinyl acetate) and acrylic adhesives. Studies in Conservation,* 1996. **41:**19-44.

35   H. Keskkula and D. R. Paul, *Miscibility of polyethyloxazoline with thermoplastic polymers. Journal of Applied Polymer Science,* 1986. **31:**1189-1197.

36   G. M. Crisci, M. F. La Russa, M. Malagodi and S. A. Ruffolo, *Consolidating properties of Regalrez 1126 and Paraloid B72 applied to wood. Journal of Cultural Heritage,* 2010. **11:**304-308.

37   C. Villers, Lining Paintings: Papers from the Greenwich Conference on Comparative Lining Techniques. Archetype Publications, London, pp. 191 (2004).

38   G. A. Berger and W. H. Russell, *Conservation of paintings: research and innovations*, Archetype Publications, London 2007.

39   M. F. Mecklenburg, Some Aspects of the Mechanical Behaviour of Fabric Supported Paintings. National Museum, Washington D. C., pp. 28 (1982).

40   S. Hackney, *Framing for conservation at the Tate gallery. The Conservator,* 1990. **14:**44-52.

41   P. Ackroyd, *The structural conservation of canvas paintings: changes in attitude and practice since the early 1970s. Reviews in conservation,* 2002. 3-14.

42   C. F. J. Bria, *The history of the use of synthetic consolidants and lining adhesives. WAAC Newsletter,* 1986. **8:**7-11

43   G. A. Berger, *On hot-melt, heat-seal and hot-set adhesives. Journal of the American Institute of Conservation,* 1978. **18:**44-45

44   J. Hill Stoner and R. Rushfield, *Conservation of Easel Paintings*, Routledge 2012.

45 T. T. Chiu and W. J. Fairchock, Poly (2-ethyl-2oxazoline): A new water- and organic-soluble adhesive, in *Water-soluble polymers: Beauty with performance*, ed by J. E. Glass. American Chemical Society, Washington, D.C., 1986. pp. 425–433.

46 R. C. Wolbers, M. McGinn and D. Duerbeck, Poly(2-Ethyl-2-Oxazoline): a new conservation consolidant, in *AIC-WAG proceedings: Painted Wood: history and conservation*, pp. 514-527 (1994).

47 J. Arslanoglu and C. Gallent, *Evaluation of the Use of Aquazol as an Adhesive in Paintings Conservation. WAAC Newsletter,* 2003. **25:**12-18.

48 E. Meaurio, L. C. Cesteros and I. Katime, *Study of the solvent role on complexation in systems poly(mono malkyl itaconate)/tertiary polyamide. Polymer,* 1998. **39:**379-385(377).

49 C. Shelton, The Use of Aquazol-Based Gilding Preparations, in *WAG sessions of the AIC Annual Meetings*, Norfolk, Virginia (1996).

50 C. D. Walton and J. F. Warchol, Creping adhesives containing oxazoline polymers and methods of use thereof. US (1998).

51 R. Brinkhuis, Hyperbranched esteroxazoline polymers. Google Patents (2003).

52 J. Arslanoglu, *Aquazol as used in conservation practise. WAAC Newsletter,* 2004. **26:**10-15.

53 C. H. Chen, J. E. Wilson, R. M. Davis, W. Chen and J. S. Riffle, *Measurement of the segmental adsorption energy of poly(2-ethyl-2-oxazoline) on silica in water and ethanol. Macromolecules,* 1994. **27:**6376-6382.

54 G. Mirderikvand, M. Doutre, A. Murray, L. Fuster-López, D. J. Yusà-Marco and M. F. Mecklenburg, Adhesives in the Formulation of Filling Materials for Easel Paintings: Requirements, Suitability, and Stability, in *Adhesives and Consolidants for Conservation* Ottawa, Canada (2011).

55 S. Friend, *Aquazol: One Conservator's Empirical Evaluations. Technical exchange in WAAC,* 1996. **18**.

56 S. Thomas, K. Joseph, S. K. Malhotra, K. Goda and S. Sreekala, *Polymer Composites, Macro- and Microcomposites*, Wiley 2012.

57 M. F. Ashby, *Materials Selection in Mechanical Design*, Elsevier Science 2004.

58 J. Móczó and B. Pukánszky, *Polymer micro and nanocomposites: Structure, interactions, properties. Journal of Industrial and Engineering Chemistry,* 2008. **14:**535-563.

59 B. A. Bednarcyk, *An inelastic micro/macro theory for hybrid smart/metal composites. Composites Part B: Engineering,* 2003. **34:**175-197.

60   R. F. Landel and L. E. Nielsen, *Mechanical Properties of Polymers and Composites, Second Edition*, Taylor & Francis 1993.

61   J. Karger-Kocsis, *Polypropylene Structure, blends and Composites*, Springer Netherlands 1995.

62   P. M. Ajayan, L. S. Schadler and P. V. Braun, *Nanocomposite Science and Technology*, Wiley 2003.

63   B. Pukánszky and J. Móczó, *Morphology and Properties of Particulate Filled Polymers. Macromolecular Symposia,* 2004. **214:**115-134.

64   T. Xu, H. Lei and C. S. Xie, *Investigation of impact fracture process with particle-filled polymer materials by acoustic emission. Polymer Testing,* 2002. **21:**319-324.

65   M. J. John, B. Francis, K. T. Varughese and S. Thomas, *Effect of chemical modification on properties of hybrid fiber biocomposites. Composites Part A: Applied Science and Manufacturing,* 2008. **39:**352-363.

66   J. G. Cook, *Handbook of Textile Fibres: Natural Fibres*, Elsevier Science 1984.

67   K. Leppänen, S. Andersson, M. Torkkeli, M. Knaapila, N. Kotelnikova and R. Serimaa, *Structure of cellulose and microcrystalline cellulose from various wood species, cotton and flax studied by X-ray scattering. Cellulose,* 2009. **16:**999-1015.

68   U. S. Department of Energy and Office of Science, Genomics: GTL Roadmap in *Available online: http://genomicsgtlenergygov/roadmap/ (accessed on 8 December 2010).*

69   K. Fleming, D. G. Gray and S. Matthews, *Cellulose crystallites. Chemistry,* 2001. **7:**1831-1835.

70   S. M. Gaonkar and P. R. Kulkarni, *Microcrystalline cellulose from coconut shells. Acta Polymerica,* 1989. **40:**292-294.

71   Y. Padmadisastra and I. Gonda, *Preliminary studies of the development of a direct compression cellulose excipient from bagasse. Journal of Pharmaceutical Sciences,* 1989. **78:**508-514.

72   P. Thummanukitcharoen, S. Limpanart and K. Srikulkit, Preparation Of Organosilane Treated Microcrystalline Cellulose (Simcc) And The Polypropylene/ Simcc Composite, in *18th International Conference On Composite Materials*, Jeju Island, Korea (2011).

73   J. K. Pandey, H. Takagi, A. N. Nakagaito and H. J. Kim, *Handbook of Polymer Nanocomposites. Processing, Performance and Application: Volume C: Polymer Nanocomposites of Cellulose Nanoparticles*, Springer Berlin Heidelberg 2014.

74   K. Das, D. Ray, N. R. Bandyopadhyay and S. Sengupta, *Study of the Properties of Microcrystalline Cellulose Particles from Different*

Renewable Resources by XRD, FTIR, Nanoindentation, TGA and SEM. Journal of Polymers and the Environment, 2010. **18:**355-363.

75   Y. P. Chauhan, R. S. Sapkal, V. S. Sapkal and G. S. Zamre, *Microcrystalline Cellulose from Cotton Rags (Waste from Garment and Hosiery Industries). International Journal of Chemical Sciences,* 2009. **7:**681-688.

76   W. Qui, T. Endo and T. Hirotsu, *Interfacial interaction, morphology and tensile properties of a composite of highly crystalline cellulose and maleated polypropylene. Journal of Applied Polymer Science,* 2006. **102:**30-41.

77   S. Kalia, A. Dufresne, B. M. Cherian, B. S. Kaith, L. Avrous, J. Njuguna and E. Nassiopoulos, *Cellulose-Based Bio- and Nanocomposites: A Review. International Journal of Polymer Science,* 2011. **2011:**35 pages.

78   V. Favier, H. Chanzy and J. Y. Cavaille, *Polymer Nanocomposites Reinforced by Cellulose Whiskers. Macromolecules,* 1995. **28:**6365-6367.

79   D. Klemm, F. Kramer, S. Moritz, T. Lindström, M. Ankerfors, D. Gray and A. Dorris, *Nanocelluloses: A New Family of Nature-Based Materials. Angewandte Chemie International Edition,* 2011. **50:**5438-5466.

80   S. J. Eichhorn, A. Dufresne, M. Aranguren, N. E. Marcovich, J. R. Capadona, S. J. Rowan, C. Weder, W. Thielemans, M. Roman, S. Renneckar, W. Gindl, S. Veigel, J. Keckes, H. Yano, K. Abe, M. Nogi, A. N. Nakagaito, A. Mangalam, J. Simonsen, A. S. Benight, A. Bismarck, L. A. Berglund and T. Peijs, *Review: current international research into cellulose nanofibres and nanocomposites. Journal of Materials Science,* 2010. **45:**1-33.

81   M. Ankerfors, Microfibrillated cellulose: Energy-efficient preparation techniques and key properties, in *Department of Fibre and Polymer Technology Division of Fibre Technology*. KTH Royal Institute of Technology, Stockholm, Sweden (2012).

82   G. Siqueira, J. Bras and A. Dufresne, *Cellulosic Bionanocomposites: A Review of Preparation, Properties and Applications. Polymers,* 2010. **2:**728-765.

83   I. Siró and D. Plackett, *Microfibrillated cellulose and new nanocomposite materials: a review. Cellulose,* 2010. **17:**459-494.

84   M. Andresen, L.-S. Johansson, B. S. Tanem and P. Stenius, *Properties and characterization of hydrophobized microfibrillated cellulose. Cellulose,* 2006. **13:**665-677.

85   A. N. Nakagaito and H. Yano, *Novel high-strength biocomposites based on microfibrillated cellulose having nano-order-unit web-like network structure. Applied Physics A,* 2005. **80:**155-159.

86   F. W. Herrick, R. L. Casebier, J. K. Hamilton and K. R. Sandberg, *Microfibrillated cellulose: morphology and accessibility* 1983.

87   S. Montanari, M. Roumani, L. Heux and M. R. Vignon, *Topochemistry of Carboxylated Cellulose Nanocrystals Resulting from TEMPO-Mediated Oxidation. Macromolecules,* 2005. **38:**1665-1671.

88   A. Hirai, O. Inui, F. Horii and M. Tsuji, *Phase Separation Behavior in Aqueous Suspensions of Bacterial Cellulose Nanocrystals Prepared by Sulfuric Acid Treatment. Langmuir,* 2008. **25:**497-502.

89   J. Sugiyama, H. Chanzy and J. Revol, *On the polarity of cellulose in the cell wall of Valonia. Planta,* 1994. **193:**260-265.

90   X. Cao, Y. Chen, P. R. Chang, M. Stumborg and M. A. Huneault, *Green composites reinforced with hemp nanocrystals in plasticized starch. Journal of Applied Polymer Science,* 2008. **109:**3804-3810.

91   C. Bonini, L. Heux, J.-Y. Cavaillé, P. Lindner, C. Dewhurst and P. Terech, *Rodlike Cellulose Whiskers Coated with Surfactant: A Small-Angle Neutron Scattering Characterization. Langmuir,* 2002. **18:**3311-3314.

92   W. Thielemans, C. R. Warbey and D. A. Walsh, *Permselective nanostructured membranes based on cellulose nanowhiskers. Green Chemistry,* 2009. **11:**531-537.

93   S. Beck-Candanedo, M. Roman and D. G. Gray, *Effect of Reaction Conditions on the Properties and Behavior of Wood Cellulose Nanocrystal Suspensions. Biomacromolecules,* 2005. **6:**1048-1054.

94   D. Bondeson, A. Mathew and K. Oksman, *Optimization of the isolation of nanocrystals from microcrystalline cellulose by acid hydrolysis. Cellulose,* 2006. **13:**171-180.

95   M. Tanahashi, *Development of Fabrication Methods of Filler/Polymer Nanocomposites: With Focus on Simple Melt-Compounding-Based Approach without Surface Modification of Nanofillers. Materials,* 2010. **3:**1593-1619.

96   K. Kalaitzidou, H. Fukushima and L. T. Drzal, *A new compounding method for exfoliated graphite–polypropylene nanocomposites with enhanced flexural properties and lower percolation threshold. Composites Science and Technology,* 2007. **67:**2045-2051.

97   D. W. Chae and B. C. Kim, *Characterization on polystyrene/zinc oxide nanocomposites prepared from solution mixing. Polymers for Advanced Technologies,* 2005. **16:**846-850.

98   CIE, *Colorimetry. CIE Publication No 15.2*, CIE Central Bureau, Vienna 1986.

99   S. V. Glass and S. L. Zelinka, *Wood Handbook, Chapter 04: Moisture Relations and Physical Properties of Wood*, U.S. Department of Agriculture, Forest Service, Forest Products Laboratory, Madison, WI 2010.

100   J. F. Siau, *Wood: influence of moisture on physical properties*, Virginia Polytechnic institute and State University. Dept. of Wood Science & Forest Products, Virginia 1995.

101   C. Skaar, *Wood-Water Relationships*, Springer 1988.

102   F. Lionetto, G. Quarta, A. Cataldi, A. Cossa, R. Auriemma, L. Calcagnile and M. Frigione, *Characterization and dating of waterlogged woods from an ancient harbor in Italy*. Journal of Cultural Heritage, 2014. **15:**213-217.

103   F. Lionetto and M. Frigione, *Effect of novel consolidants on mechanical and absorption properties of deteriorated wood by insect attack*. Journal of Cultural Heritage, 2012. **13:**195-203.

104   M. Plötze and P. Niemz, *Porosity and pore size distribution of different wood types as determined by mercury intrusion porosimetry*. European Journal of Wood and Wood Products, 2011. **69:**649-657.

105   A. Dorigato and A. Pegoretti, *Flexural and impact behaviour of carbon/basalt fibers hybrid laminates*. Journal of Composite Materials, 2013.

106   J. Podany, K. M. Garland, W. R. Freeman and J. Rogers, *Paraloid B-72 as a Structural Adhesive and as a Barrier within Structural Adhesive Bonds: Evaluations of Strength and Reversibility*. Journal of the American Institute for Conservation, 2001. **40:**15-33.

107   D. Allard and K. B. Katz, *Quantitative Study: The Effects of Sized Materials and "Drying Time" in the Use of Lascaux 360 HV as a Lining Adhesive*. Journal of the American Institute for Conservation, 1987. **26:**19-25.

108   K. B. Katz, *The Quantitative Testing and Comparisons of Peel and Lap/Shear for Lascaux 360 H.V. and Beva 371*. Journal of the American Institute for Conservation, 1985. **24:**60-68.

109   A. Bledzki and G. J., *Composites reinforced with cellulose based fibres*. Progress in Polymer Science, 1999. **24:**221-274.

110   K. Kalaitzidou, H. Fukushima and L. T. Drzal, *Mechanical properties and morphological characterization of exfoliated graphite–polypropylene nanocomposites*. Composites Part A Applied Science and Manufacturing, 2007. **38:**1675–1682.

111   A. Yasmin, J. J. Luo, J. L. Abot and I. M. Daniel, *Mechanical and thermal behavior of clay/epoxy nanocomposites*. Composites Science and Technology, 2006. **66:**2415-2422.

112   A. Kiziltas, D. J. Gardner, Y. Han and H. S. Yang, *Dynamic mechanical behavior and thermal properties of microcrystalline cellulose (MCC)-filled nylon 6 composites*. Thermochimica Acta, 2011. **519:**38-43.

113   M. K. M. Haafiz, A. Hassan, Z. Zakaria, I. M. Inuwa, M. S. Islam and M. Jawaid, *Properties of polylactic acid composites reinforced with oil palm*

biomass microcrystalline cellulose. Carbohydrate Polymers, 2013. **98:**139-145.

114   A. Dorigato, S. Morandi and A. Pegoretti, *Effect of nanoclay addition on the fiber/matrix adhesion in epoxy/glass composites*. *Journal of Composite Materials,* 2012. **46:**1439-1451.

115   A. Dorigato, A. Pegoretti and M. Quaresimin, *Thermo-mechanical characterization of epoxy/clay nanocomposites as matrices for carbon/nanoclay/epoxy laminates*. *Materials Science and Engineering A,* 2011. **528:**6324-6333.

116   Y. H. Cui, X. X. Wang, Q. Xu and Z. Z. Xia, *Research on Moisture Absorption Behavior of Recycled Polypropylene Matrix Wood Plastic Composites*. *Journal of Thermoplastic Composite Materials,* 2010. **24:**65-82.

117   B. D. Harper, G. H. Staab and R. S. Chen, *A note on the effects of voids upon the hygral and mechanical properties of AS4/3502 graphite/epoxy*. *Journal of Composite Materials,* 1987. **21:**280-289.

118   O. Ishai, *Environmental effects on deformation, strength, and degradation of unidirectional glass ̄ber reinforced plastics, II experimental study*. *Polymer Engineering and Science,* 1975. **15:**491-499.

119   W. P. Paplham, R. A. Brown, I. M. Salin and J. C. Seferis, *Absorption of water in polyimide resins and composites*. *Journal of Applied Polymer Science,* 1995. **57:**133-137.

120   J. L. Thomason, *The interface region in glass fiber-reinforced epoxy resin composites: 1 sample preparation, void content and interfacial strength*. *Composites,* 1995. **26:**467-475.

121   J. L. Thomason, *The interface region in glass fiber-reinforced epoxy resin composites: 2 water absorption, void content and interface*. *Composites,* 1995. **26:**467-475.

122   B. Yu, H.-N. Lim and Y.-K. Lee, *Influence of nano- and micro-filler proportions on the optical property stability of experimental dental resin composites*. *Materials & Design,* 2010. **31:**4719-4724.

123   J. A. Mbey, S. Hoppe and F. Thomas, *Cassava starch–kaolinite composite film. Effect of clay content and clay modification on film properties*. *Carbohydrate Polymers,* 2012. **88:**213-222.

124   R. W. G. Hunt and M. R. Pointer, *Measuring Colour, 4th Edition*, John Wiley & Sons, UK 2011.

125   G. Sharma and R. Bala, Digital Color Imaging Handbook. CRC Press (2002).

126   M. Mahy, L. Van Eycken and A. Oosterlinck, *Evaluation of Uniform Color Spaces Developed after the Adoption of CIELAB and CIELUV*. *Color Research & Application,* 1994. **19:**105-121.

127   A. P. Mathew, K. Oksman and M. M. Sain, *Mechanical properties of biodegradable composites from poly lactic acid (PLA) and microcrystalline cellulose (MCC). Journal of Applied Polymer Science,* 2005. **97:**2014–2025.

128   R. E. Lavengood and L. A. Goettler, Stiffness of non-aligned fiber reinforced composites, in *US Government R&D Reports*. National Technical Information Service, Springfield, VA, USA (1971).

129   J. C. Halpin, *Stiffness and expansion estimates for oriented short fibre composites. Journal of Composite Materials,* 1969. **3:**732-735.

130   B. C. Hancock, S.-D. Clas and K. Christensen, *Micro-scale measurement of the mechanical properties of compressed pharmaceutical powders. 1: The elasticity and fracture behavior of microcrystalline cellulose. International Journal of Pharmaceutics,* 2000. **209:**27-35.

131   S. J. Eichhorn and R. J. Young, *The Young's modulus of a microcrystalline cellulose. Cellulose,* 2001. **8:**197–207.

132   E. Abraham, B. Deepa, L. A. Pothan, M. Jacob, S. Thomas, U. Cvelbar and R. Anandjiwala, *Extraction of nanocellulose fibrils from lignocellulosic fibres: A novel approach. Carbohydrate Polymers,* 2011. **86:**1468-1475.

133   A. Mandal and D. Chakrabarty, *Isolation of nanocellulose from waste sugarcane bagasse (SCB) and its characterization. Carbohydrate Polymers,* 2011. **86:**1291-1299.

134   E. Abraham, M. S. Thomas, C. John, L. A. Pothen, O. Shoseyov and S. Thomas, *Green nanocomposites of natural rubber/nanocellulose: Membrane transport, rheological and thermal degradation characterisations. Industrial Crops and Products,* 2013. **51:**415-424.

135   M. Roman and W. T. Winter, *Effect of Sulfate Groups from Sulfuric Acid Hydrolysis on the Thermal Degradation Behavior of Bacterial Cellulose. Biomacromolecules,* 2004. **5:**1671-1677.

136   *ASTM Standard D143-94, Standard Test Methods for Small Clear Specimens of Timber*, ASTM International, West Conshohocken, USA 1994.

137   D. Bondeson, Biopolymer-based Nanocomposites: Processing and Properties, in *Department of Engineering Design and Materials, Faculty of Engineering Science and Technology*. Norwegian University of Science and Technology, Trondheim (2007).

138   H. Sadeghifar, I. Filpponen, S. Clarke, D. Brougham and D. Argyropoulos, *Production of cellulose nanocrystals using hydrobromic acid and click reactions on their surface. Journal of Materials Science,* 2011. **46:**7344-7355.

139   P. Lu and Y.-L. Hsieh, *Preparation and characterization of cellulose nanocrystals from rice straw. Carbohydrate Polymers,* 2012. **87:**564-573.

140   J. Lee, S. Park and S. Kim, *Preparation of cellulose nanowhiskers and their reinforcing effect in polylactide. Macromolecular Research,* 2013. **21:**1218-1225.

141   L. N. Howard and S. H. Zeronian, *Historic Textile and Paper Materials*, American Chemical Society 1986.

142   M. L. Franquelo, A. Duran, L. K. Herrera, M. C. Jimenez de Haro and J. L. Perez-Rodriguez, *Comparison between micro-Raman and micro-FTIR spectroscopy techniques for the characterization of pigments from Southern Spain Cultural Heritage. Journal of Molecular Structure,* 2009. **924–926:**404-412.

143   A. M. Seves, S. Sora, G. Scicolone, G. Testa, A. M. Bonfatti, E. Rossi and A. Seves, *Effect of thermal accelerated ageing on the properties of model canvas paintings. Journal of Cultural Heritage,* 2000. **1:**315-322.

144   K. Castro, E. Princi, N. Proietti, M. Manso, D. Capitani, S. Vicini, J. M. Madariaga and M. L. De Carvalho, *Assessment of the weathering effects on cellulose based materials through a multianalytical approach. Nuclear Instruments and Methods in Physics Research Section B: Beam Interactions with Materials and Atoms,* 2011. **269:**1401-1410.

145   G. C. Scicolone, *Dipinti su tela: metodologie d'indagine per i supporti cellulosici*, Nardini 1993.

Publications on peer reviewed journals

- C. Esposito Corcione, A. Cataldi, M. Frigione: "Measurements of Size Distribution Nanoparticles in Ultraviolet-Curable Methacrylate-Based Boehmite Nanocomposites" in Journal of Applied Polymer Science, Vol. 128, pp. 4102-4109 (2013)
- F. Lionetto, G. Quarta, A. Cataldi, A. Cossa, R. Auriemma, L. Calcagnile, M. Frigione: "Characterization and dating of waterlogged woods from an ancient harbor in Italy" in Journal of Cultural Heritage, Vol. 15 (2), pp. 213-217 (2013)
- A. Cataldi, A. Dorigato, F. Deflorian, A. Pegoretti: "Thermo-mechanical properties of innovative microcrystalline cellulose filled composites for art protection and restoration" in Journal of Materials Science, Vol.49 (5), pp. 2035-2044 (2014)
- A. Cataldi, A. Dorigato, F. Deflorian, A. Pegoretti: "Effect of the water absorption on the mechanical behaviour of microcrystalline cellulose filled composites for art protection and restoration" in Journal of Applied Polymer Science, Vol. 131 (18), pp. 40741 (2014)
- A. Cataldi, A. Dorigato, F. Deflorian, A. Pegoretti: "Innovative microcrystalline cellulose composites as lining adhesives for canvas" in Polymer Engineering and Science. In press
- A. Cataldi, F. Deflorian, A. Pegoretti: "Poly 2-ethyl-2-oxazoline/microcrystalline cellulose composites for cultural heritage conservation: mechanical characterization in dry and wet state and application as lining adhesives of canvas" in International Journal of Adhesion and Adhesives. Submitted
- A. Cataldi, F. Deflorian, A. Pegoretti: "Microcrystalline cellulose filled composites for wooden artwork consolidation: application and physic-mechanical characterization" in Materials and Design. Submitted
- A. Cataldi, L. Berglund, F. Deflorian, A. Pegoretti: "Effect of cellulose on the thermo-mechanical behaviour of an adhesive for oil paintings restoration: a comparison between micro and nanocomposites" in Nanocomposites. Submitted

Participation to congresses, schools and workshops

- A. Cataldi, A. Dorigato, F. Deflorian, A. Pegoretti: "Compositi polimerici per la protezione e il restauro di opere d'arte" 6th Biennial International Congress "Colour and Conservation", 16th-18th November 2012, Parma, Italy
- A. Cataldi, A. Dorigato, F. Deflorian, A. Pegoretti: "Polymer composites for artwork protection and restoration" Congress of the European Polymer Federation (EPF-2013), June 16th-21th 2013, Pisa, Italy
- A. Cataldi, L. Berglund, F. Deflorian, A. Pegoretti: "Polymer composite with micro- and nanocellulose for artwork protection and restoration" 16th European Conference on Composite Materials (ECCM16), June 22nd-26th 2014, Seville, Spain
- A. Cataldi, F. Deflorian, A. Pegoretti: "Compositi polimerici con micro e nanocellulosa per la conservazione e il restauro di opere d'arte" XII Convegno nazionale Associazione Italiana d'Ingegneria dei Materiali (AIMAT-2014), September 21st-24th 2014, Lecce, Italy

- Doctoral Course on "Climate Change, Global Change And Cultural Heritage: Vulnerability, Impact and Adaptation" October 7th-10th 2013, Ravello, Italy

Other activities

Activities abroad

- 6th-10th May 2013 at the Wallenberg Wood Science Center in Stockholm, Sweden - Department of Fiber and PolymerTechnology, Royal Institute of Technology (KTH). Training on the production of nanocomposites with CNC by solution mixing method under the supervision of Prof. L. Berglund.

Journal reviewing

- Journal of Reinforced Plastics and Composites (IF=1.19)

Student tutoring

- Research advisor of a graduate student in Conservazione e gestione dei Beni culturali (University of Trento, 2012-2013) regarding the "Restauro Di Sculture Lignee. Studio Di Consolidanti Caricati Con Microcellulosa"

Acknowledgements

Trento, 30th April, 2015